

# Multiscale Mechanical Characterization of Subcellular Structures in Living Walled Cells

Thesis by  
Leah Ginsberg

In Partial Fulfillment of the Requirements for the  
Degree of  
Doctor of Philosophy

The logo for the California Institute of Technology (Caltech), featuring the word "Caltech" in a bold, orange, sans-serif font.

CALIFORNIA INSTITUTE OF TECHNOLOGY  
Pasadena, California

2021  
Defended March 15, 2021

© 2021

Leah Ginsberg

ORCID: 0000-0001-9685-7014

All rights reserved except where otherwise noted

## ACKNOWLEDGEMENTS

No one can write your thesis for you, but no one can write a thesis alone. It is an impossible task to thank everyone who helped me on my journey to write this dissertation, but I will do my best in the next few paragraphs.

First, I would like to thank my adviser, Professor Guruswami Ravichandran. Ravi allowed me immense academic freedom, provided insightful comments on my work, and has always demonstrated an inspiring combination of perceptiveness and kindness. I would also like to thank the members of my committee: Professors Kaushik Bhattacharya, Chiara Daraio, and Eleftheria Roumeli. Group meetings with Kaushik and his group have greatly strengthened my appreciation for rigorous mathematics and the interconnected nature of the many subfields of math and engineering. Discussions with Chiara were the starting point for much of the work in this thesis, and her feedback substantially strengthened the final product. Eleftheria has been my primary collaborator, and her drive and passion for uncovering fundamental physics is much of what kept me motivated and excited to complete the work presented here. Eleftheria has also been a fantastic mentor and friend to me, and I thank her deeply for taking me under her wing. I would also like to thank Professors Mikhael Shapiro, Julia Kornfield, David Tirrell, and Melany Hunt. Mikhael, Julia, and Dave provided insightful comments and suggestions on my work when I presented in our DARPA project meetings. I am also grateful for the enormous amount of biology and chemistry I learned from listening to members of their groups present in those project meetings. Melany provided me with excellent advice in my efforts to increase diversity, equity and inclusion (DEI) within the Mechanical Civil Engineering Department at Caltech, and more importantly, has been exceedingly kind and always had her office door open.

The work presented in this thesis would have been impossible without my collaborators: Robin McDonald, Qinchun Lin, Giada Spigolon, Rodinde Hendrickx, and Professors Misato Ohtani and Taku Demura. Due to the COVID-19 pandemic, many of us have not met in person, but I thank them all for their collaboration and helpful Zoom discussions. I would also like to thank all of the members of the Ravichandran research lab for their feedback and support: Drs. Suraj Ravindran and Korhan Sahin, Vatsa Gandhi, Zichen Gu, Akshay Joshi, Kimberley McDonald, Tomoyuki Oniyama, and Jack Weeks. Many Caltech staff members have also supported my research and DEI efforts. I would especially like to thank Holly Golcher, Lynn

Seymour, Jenni Campbell, Donna Mojahedi, and Carolina Oseguera. I have missed seeing each of you at the office during this strange year.

I am thankful to be surrounded by family and friends who can make failures feel like triumphs and give me the motivation to push through even the deepest frustrations. Thank you to my close friends (and current quarantine buddies) Alex, Maegan, and Kyle for Thursday night chats and lazy Saturdays in the front yard. To my sisters, Beth and Abby, you are both family and friends, and I thank you for constantly providing me with the joy and love I need to keep pushing forward. To my parents and grandparents, thank you for your unwavering support and for nurturing my creativity and interest in science. Thank you especially to my grandfather, for sharing your love of science with me at a very young age.

Finally, I acknowledge my funding sources. Specifically, I received support from the Allan Acosta Endowed Graduate Fellowship through the Department of Mechanical and Civil Engineering at the California Institute of Technology. I also received support from the Defense Advanced Research Projects Agency's Engineered Living Materials program under grant number HR0011-17.

## ABSTRACT

The physiology of walled cells is dramatically different from that of human cells, but the biomechanics of walled cells are far less studied. Most bacterial, fungal, and plant cells have a strong cell wall (CW), which allows them to withstand large hydrostatic pressures in the cytoplasm, called turgor. Turgor pressure conflates the mechanics of subcellular components and complicates the characterization of the cell. In this dissertation, new models are introduced and explored for single cells to investigate the multiscale mechanics of plant and bacterial cells using micro- and nano-indentation experiments.

A multi-scale biomechanical assay is used to study the mechanical properties of plant cells. The plant CW is typically around 5% of the width of the entire cell, and is thought to carry most of the mechanical load. Large-scale indentations using a micro-indentation system probe the behavior of the overall cell structure, and atomic-force microscopy (AFM) nano-scale indentations are used to isolate the CW response. To determine the effect of external osmotic pressure, indentations are performed on cells in different osmotic conditions: hypotonic, isotonic, and hypertonic. The cell is idealized as two springs acting in series, one to represent the CW and one to represent the cytoplasm. The model uses the experimentally determined initial stiffnesses as input to the model to determine the relative stiffness contributions of the CW and the cytoplasm.

The first type of walled cells investigated is the xylem vessel element of *Arabidopsis thaliana*. The xylem is responsible for transporting water through the stem of any vascular plant (more commonly known as a land plant), and hence it must maintain structural integrity against high internal pressures while transporting water from the roots to the leaves. For extra structural support, xylem vessel elements develop secondary cell walls (SCWs), which are known to be a key component for mediating mechanical strength and stiffness in vascular plants. The structure and biomechanics of cultured plant cells are investigated during the cellular developmental stages associated with SCW formation using the multi-scale biomechanical assay described above. To determine the effect of morphological changes during differentiation, micro- and nano-indentations are performed on cells in different observed stages of the differentiation process. Prior to triggering differentiation, cells in hypotonic pressure conditions are significantly stiffer than cells in isotonic or hypertonic conditions, highlighting the dominant role of turgor pressure. Plasmolyzed cells with a

SCW reach similar levels of stiffness as cells with maximum turgor pressure. Analysis using the two-spring model shows that the stiffness of the primary CW in all of these conditions is lower than the stiffness of the fully-formed SCW. These results provide the first experimental characterization of the mechanics of SCW formation at the single-cell level in plant cells.

Next, the mechanical response of individual *Nicotiana tabacum* cells from a suspension culture is studied using the same multi-scale biomechanical assay. The role played by the microtubules (MTs) and actin filaments (AFs) is determined through the use of drug treatments which selectively remove MTs and AFs. A generative statistical model is added to the two-spring model to quantify the stiffnesses of the CW, cytoplasm, turgor pressure, MTs, and AFs. Analysis of the initial stiffness and energy dissipation calculated from micro-indentation experiments indicates that the MTs and AFs contribute significantly to the mechanical response of a cell under compression. Micro- and nano-indentation tests confirm that turgor pressure is the most significant contributor to the stiffness response of turgid cells in compression. Finally, the results reveal that turgor pressure exerts stress on the CW, which leads to a measurable stiffening of the CW.

The studies described above focused on developing a discrete model to describe the mechanics of a cell in indentation experiments. However, the most common type of model used to evaluate the mechanics of a cell are continuum models. Continuum models are also necessary to decouple the material properties of subcellular components from their structure. In the final section, AFM indentations are simulated on a gram-negative bacterium, *Escherichia coli*, and a sensitivity study and inverse analysis are performed to solve for the CW elastic modulus and turgor pressure simultaneously. Sensitivity study results reveal that uncertainty in turgor pressure and CW elasticity indeed contribute the most to variability in force spectra from AFM measurements. The parameter space of possible values for CW elastic modulus and turgor pressure is discretized using triangular elements. "Simulated experiments" are tested throughout the parameter space, and correlations between the CW elastic modulus and turgor pressure, which depend on the type of objective function, are investigated. Two unique objective functions are tested in the inverse analysis, and a third objective function, which is a weighted sum of the first two, is found to reduce errors in estimated CW elastic modulus and turgor pressure by 20% and 11%, respectively. The use of this type of inverse analysis has the potential to elucidate the material properties of CWs using a single indentation measurement and reliably

decouple these properties from the high turgor pressures inside walled cells.

## PUBLISHED CONTENT AND CONTRIBUTIONS

- [1] Leah Ginsberg and Guruswami Ravichandran. “Inverse analysis to determine the mechanical properties of single bacterial cells”. In: *TBD* (In preparation).
- [2] Leah Ginsberg et al. “Cell wall and cytoskeletal contributions in single cell biomechanics of *Nicotiana tabacum*”. In: *Plant and Cell Physiology* (In review).  
L.M.G. participated in the data acquisition and analysis, the preparation, review, and editing of the written article, and the visualization of the data.
- [3] Leah Ginsberg et al. “Multiscale inverse analysis to determine optimal elastic properties of *Bacillus subtilis* and N-(hydroxymethyl)acrylamide”. In: *TBD* (In preparation).
- [4] Leah Ginsberg et al. “Plant biomechanics: from single cells to natural fiber reinforced biocomposites”. In: *TBD* (In preparation).
- [5] Leah Ginsberg et al. “Structure and Biomechanics during Xylem Vessel Transdifferentiation in *Arabidopsis thaliana*”. en. In: *Plants* 9.12 (Dec. 2020), p. 1715. ISSN: 2223-7747. DOI: 10.3390/plants9121715. URL: <https://www.mdpi.com/2223-7747/9/12/1715>.  
L.M.G. participated in the data acquisition and analysis, the preparation, review, and editing of the written article, and the visualization of the data.

## TABLE OF CONTENTS

Acknowledgements . . . . .	iii
Abstract . . . . .	v
Published Content and Contributions . . . . .	viii
Table of Contents . . . . .	viii
List of Illustrations . . . . .	x
List of Tables . . . . .	xii
. . . . .	xiii
Chapter I: Introduction . . . . .	1
1.1 Indentation Experiments . . . . .	2
1.2 Modeling Indentations . . . . .	6
1.3 Outline of This Thesis . . . . .	12
Chapter II: Structure and Biomechanics during Xylem Vessel Transdifferentiation in <i>Arabidopsis thaliana</i> . . . . .	19
2.1 Introduction . . . . .	20
2.2 Results and Discussion . . . . .	22
2.3 Materials and Methods . . . . .	37
2.4 Conclusions . . . . .	40
Chapter III: Cell Wall and Cytoskeletal Contributions in Single-Cell Biomechanics of <i>Nicotiana tabacum</i> . . . . .	52
3.1 Introduction . . . . .	53
3.2 Results and Discussion . . . . .	54
3.3 Materials & Methods . . . . .	69
Chapter IV: Inverse Analysis to Determine the Mechanical Properties of Single Bacterial Cells . . . . .	79
4.1 Introduction . . . . .	79
4.2 Model . . . . .	81
4.3 Results and Discussion . . . . .	87
4.4 Conclusions . . . . .	91
Chapter V: Conclusions and Outlook . . . . .	104
5.1 Future Work in Models of Walled Cells . . . . .	106
5.2 Future Work in Parameter Fitting for Walled Cell Models . . . . .	108
5.3 Extensions to Biocomposites and Living Materials . . . . .	109
Appendix A: Parameter Fitting Methods . . . . .	113

## LIST OF ILLUSTRATIONS

<i>Number</i>	<i>Page</i>
1.1 Schematic of the experimental nano-indentation setup. . . . .	4
1.2 Schematic of the experimental micro-indentation setup. . . . .	5
1.3 Distribution of stress in a cell under compression from different sized indenters. . . . .	7
2.1 Confocal images of VND7-inducible cells in the three stages of transdifferentiation. . . . .	23
2.2 Illustration of cell dimensions on elongated VND7-inducible cells. . .	24
2.3 Proposed two-spring model of a plant cell. . . . .	26
2.4 Measured stiffnesses from micro-indentation experiments in each stage of transdifferentiation and osmotic solution. . . . .	28
2.5 Young's moduli from nano-indentation experiments in each stage of transdifferentiation. . . . .	36
2.6 Optical microscopy images to demonstrate classification by stage of transdifferentiation. . . . .	43
2.7 Confocal images of a cell in final stage of transdifferentiation with visible hydrolyzed PCW. . . . .	44
2.8 Spring models for all treatments/stages. . . . .	44
2.9 Images of VND7-inducible cells in plasmolyzing solution. . . . .	45
2.10 Measured stiffnesses from micro-indentation experiments in each osmotic solution and stage of transdifferentiation. . . . .	45
2.11 Stiffness comparison for each component of spring models. . . . .	45
2.12 Example indentation data for micro- and nano-indentation experiments on VND7-inducible cells. . . . .	46
3.1 Confocal images of BY-2 cells and histograms of cell dimensions. . .	55
3.2 Example AFM data and calculated indentation moduli for each osmotic solution and drug treatment. . . . .	57
3.3 Example micro-indentation data and example images of cells in each osmotic solution. . . . .	58
3.4 Calculated cell stiffnesses from micro-indentation experiments. . . .	59
3.5 Proposed two-spring model of a plant cell with cytoskeleton. . . . .	60
3.6 Table illustrating the two-spring model for each test condition. . . . .	62

3.7	Contours of the posterior distribution. . . . .	64
3.8	Comparison of decoupled stiffness values for each subcellular component. . . . .	66
3.9	Calculated energy dissipated by a cell in micro-indentation experiments.	68
3.10	Prior predictive checks. . . . .	74
4.1	Comparison between force-indentation curves from previous literature and proposed model. . . . .	82
4.2	Schematic of simulation and sensitivity study data. . . . .	84
4.3	Convergence plots for inverse analysis to solve for CW elasticity and turgor pressure. . . . .	88
4.4	FEM data from simulation of AFM indentation. . . . .	93
4.5	Element types used in construction of Abaqus FEM. . . . .	94

## LIST OF TABLES

<i>Number</i>		<i>Page</i>
2.1	Measured principal dimensions and feature sizes of elongated VND7-inducible cells. . . . .	25
2.2	Measured principal dimensions of elongated and round-shaped cells.	42
2.3	SCW bundle feature sizes for elongated and round-shaped cells. . . .	42
2.4	Osmotic pressure calculated for each of the three solutions used for mechanical testing. . . . .	43
4.1	Ranges of model parameters. . . . .	86

## List of Abbreviations

<b>AF</b>	actin filament
<b>AFM</b>	atomic force microscopy
<b>AR</b>	aspect ratio
<b>BY-2</b>	Bright Yellow-2
<b>CCW</b>	combined cell walls
<b>CFM</b>	cellular force microscope
<b>CW</b>	cell wall
<b>DEX</b>	dexamethasone
<b>ECDF</b>	empirical cumulative distribution function
<b>FEM</b>	finite-element model
<b>FEM</b>	finite-element model
<b>GM</b>	growth media
<b>LatB</b>	Latrunculin B
<b>MAP</b>	maximum a posteriori
<b>MLE</b>	maximum likelihood estimate
<b>MT</b>	microtubule
<b>OLS</b>	ordinary least squares
<b>PCD</b>	programmed cell death
<b>PCW</b>	primary cell wall
<b>PS</b>	plasmolyzing solution
<b>RSS</b>	residual sum of squares
<b>SCW</b>	secondary cell wall
<b>SE</b>	standard error

**TE** tracheary element

**VND7** VASCULAR-RELATED NAC-DOMAIN7

*Chapter 1*

## INTRODUCTION

The physiology of walled cells is important to human health, agriculture, molecular biology and biotechnology, and environmental sustainability. The presence of a strong cell wall (CW) in most bacterial, fungal, and plant cells allows them to hold enormous hydrostatic pressures in the cytoplasm, called turgor in microbiology literature. While mammalian cells survive in a relatively well-controlled osmotic environment and maintain internal pressures typically under a kilopascal (kPa) [1], walled cells survive in some of the harshest environments on our planet and maintain enormous turgor pressures. Bacterial cells reportedly hold turgor pressures between 30 and 300 kPa [2], plant cells between 300 kPa and 1 MPa [3], and pressures up to 1.5 MPa have been reported in some fungal cells [4]. The fluctuation of internal turgor pressures enables these walled cells to store water for long periods of time and survive harsh and uncertain environments [5]. For example, cacti survive in deserts without rainfall for months at a time, fungi live at the bottom of deep oceans and in the hypersaline Dead Sea, and bacteria have been found thriving inside hot springs and volcanic craters.

In addition to its evolutionary benefit, the mechanical interplay between a strong cell wall and turgor pressure is integral to cell growth. In a healthy and growing walled cell, turgor pressure causes stress to build up in the cell wall. The viscous property of the cell wall causes stress relaxation and expansion of the cell. As the cell expands, turgor pressure declines. Then, the difference in pressure between the expanded cell and its environment causes water uptake, which returns turgor pressure and cell wall stresses to their original state, and the cycle repeats [6]. Another ubiquitous feature of walled cells is a rod-like shape, which is also derived from the mechanical interaction of the cell wall and turgor pressure. While cell sizes and growth mechanisms differ, the morphology of many rod-shaped cells is similar, indicating that there is a common mechanical balance of turgor pressure and cell wall stress across species [7].

The highly interconnected nature of cell wall stress and turgor pressure and experimental limitations at small scales has led to a large range of reported values for these parameters in the literature. A direct measurement of turgor pressure is possible

in larger cells, like plant and fungal cells through the direct insertion of a pressure gauge [8, 9]. Unfortunately, this method ultimately destroys the cell being tested, so repeated measurements are not possible on the same cell. Incipient plasmolysis is a reversible process, so the cell is preserved in this method and repeated measurements are possible [10]. Again, however, this method is currently only possible in larger plant cells where the beginnings of plasmolysis are observable. The first measurement of turgor pressure in bacteria was accomplished through the collapse of gas vesicles in the vacuole [11]. However, not all bacteria can express gas vesicles, and so a characterization of turgor pressure in some bacteria is not possible using gas vesicle collapse, although recent research in molecular biology has expanded the number of bacteria that can express gas vesicles [12]. Many have also explored the possibility of measuring turgor pressure from mechanical indentations [13–15]. The estimated pressure values from these experiments span more than an order of magnitude, even when the same experiment is performed on the same type of cell.

### **1.1 Indentation Experiments**

The development of indentation probes that can measure forces and displacements with resolutions at or below picoNewtons and nanometers, respectively, has enabled experiments that can probe subcellular mechanics. Concurrent technological advancements have led to improvements in computational modeling of mechanics at multiple length scales. In this dissertation, mechanical indentations are performed on isolated walled cells that span from the nanometer to the micrometer scale, and computational modeling of the indentations is performed to extract the mechanical properties of subcellular components.

Experimental indentation techniques have advanced our understanding of single cell mechanics substantially. The application of indentation-based methods is not limited to walled cells, and has been successfully implemented in studies of animal, plant, and bacterial cells. (For a review of the biomechanics uncovered in each of these cell types through indentation experiments, see [16], [17], and [18], respectively.) These experiments have been used to calculate stiffness contributions from components of a cell that range from cytoskeletal fibers that are a few nanometers in diameter to the entire plant cells, which are tens of micrometers in diameter. Indentations at the nanometer scale, which will be referred to henceforth as nano-indentations, are commonly used for imaging, mapping surface topography, and measuring local mechanical properties. Indentations at the micrometer scale, referred to henceforth as micro-indentations, enable the quantification of whole-cell mechanical properties.

The combination of nano- and micro-indentation experiments allows us to probe mechanics of a living cell across widely different size scales.

Despite the growing number of data sources for indentations on isolated cells and cellular components, results are rarely reproducible due to varying protocols and environmental conditions. The curvature of the cell wall can have a significant effect on measured indentation forces through friction [17]. To bypass this complicating factor, many choose to probe a relatively flat portion of the cell or tissue [19]. The dimensions of the tip and sample [17] and the contact angle between the tip and sample [15, 20] can also affect the precise values of extracted mechanical properties. The appropriate indentation depth is another important consideration when analyzing indentation data [21]. At shallow indentation depths, typically targeting less than 10% of the thickness of the cell wall, the mechanics of the cell wall can be isolated [20, 22–25]. At higher indentation depths and/or with the use of larger indentation probes, the mechanical contribution for the underlying turgor pressure and cytoplasm must be considered. Several studies have used this fact to determine both cell wall elasticity and turgor pressure using either a combination of different indentation depths [26] or by combining deep indentations with osmotic treatments [27, 28].

### **Nano-Indentation**

The experimental method used to achieve nano-indentations on living cells is atomic-force microscopy (AFM). The commercial availability of AFM systems and the wide applicability of the method to many materials and structures has made it an important tool in the field of cell biomechanics. The basic mechanism of the AFM is a reflection of a laser beam off the back of the cantilever. The position of the beam is recorded by a photodetector as the cantilever bends from the force of contact with the sample. AFM assemblies can typically measure contact forces on the order of pico-Newtons to nano-Newtons, but this range largely depends on the stiffness of the selected cantilever.

In walled cells, AFM indentation experiments have been used to measure a range of mechanical properties of both the whole cell and some subcellular components. For example, Deng et al. measured whole cell stiffness of bulging *Escherichia coli* (*E. coli*) cells using AFM, and used that measurement along with the observed radius of a bulge to extract the turgor pressure [29]. In plants, Milani et al. used AFM to measure cell stiffness of shoot apex cells in *Arabidopsis thaliana* and were able

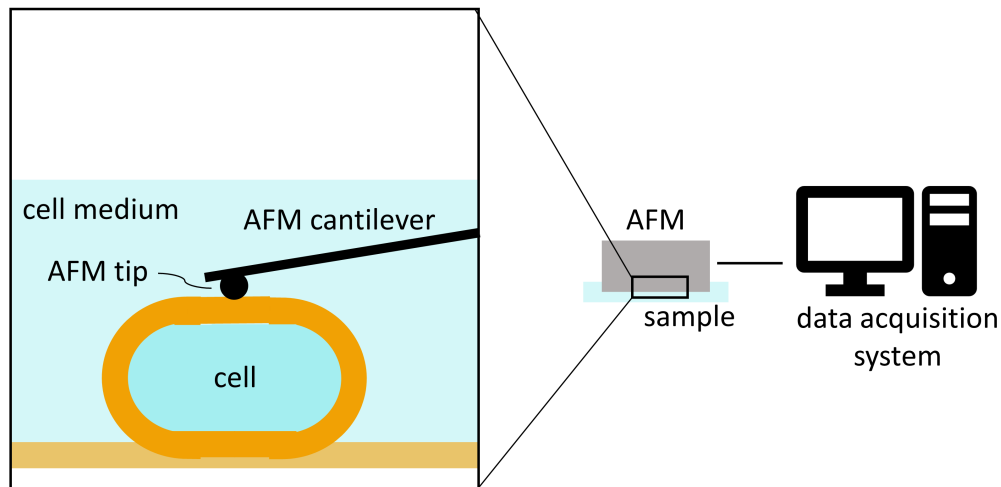


Figure 1.1: Setup of the nano-indentation experiment utilized in subsequent chapters of this thesis. The atomic-force microscopy force indentation data are obtained using the Asylum Research, MFP-3D-Bio system. The AFM tip is immersed in the medium that surrounds the cell. The cell is adhered (adhesive pictured in light gold) to a glass slide (pictured as white) to ensure no slipping occurs between the probe and the slide.

to correlate the measured stiffness with gene expression. At the subcellular level in bacteria, Yao et al. used AFM to measure the elastic modulus of unpressurized *E. coli* sacculi. Their work led to subsequent studies of the cell wall modulus of pressurized, intact *E. coli* cells, and the discovery that bacterial cell walls exhibit stress stiffening behavior [29]. In plants, Peaucelle et al. used AFM to measure both the elastic and viscoelastic properties of the cell walls in living meristems and observed an increase in elasticity in growing organs, which was found to be initiated by pectin demethylation [30].

### Micro-Indentation

Micro-indentation experiments were performed on living plant cells in Chapters 2 and 3. The micro-indentation system is also commercially available and has been used in a variety of applications ranging from cells and biological tissues to electromagnetic devices like micromotors and microfluidics structures [15, 31, 32]. The position of the micro-indentation probe is controlled through piezoelectric actuators, and the contact force is measured through a capacitive force sensor. The micro-indentation assembly can measure contact forces on the order of micro-Newtons.

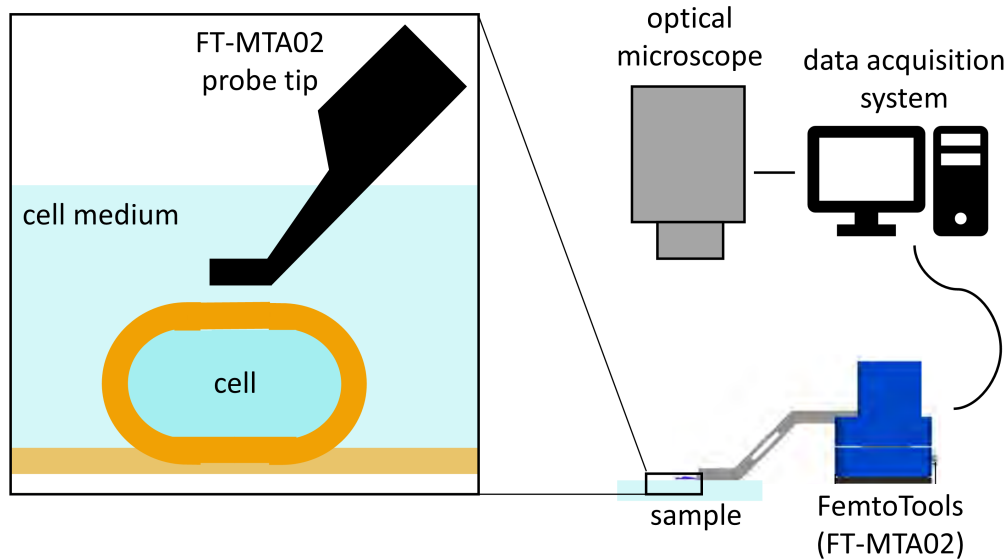


Figure 1.2: Setup of the micro-indentation experiment utilized in subsequent chapters of this thesis. An optical microscope is located on top of the sample and probe to allow user to view and manipulate location of probe to be centered over a cell. The micro-indentation tests are performed using the FT-MTA02 system (FemtoTools AG, Zurich, Switzerland). The probe tip is immersed in the medium that surrounds the cell. The cell is adhered to a glass slide to ensure no slipping occurs between the probe and the slide.

Micro-indentation systems have been used to study the mechanical response of cells to higher forces and stresses than in the nano-indentation systems. In onion epidermal peel cells, the influence of turgor pressure was studied using a micro-indentation system, which the authors termed the cellular force microscope (CFM) [15]. The same CFM system was used to examine growing lily pollen tubes [33]. In both experiments, the CFM was used to measure the apparent stiffness of cells under compression. Local differences of stiffness within the same cell were examined in onion epidermal peels. The cells appeared stiffer over the center of the cell, where turgor pressure played a role in the developing stresses. In growing lily pollen tubes, the stiffness of cells in the tip region, where growth occurs, was compared to the stiffness of cells in the more distal stem region. The initial findings of this study were in agreement with previous findings in the literature; the tip region was apparently softer than the stem region, which allowed for more deformation and growth at the tip. However, the use of a finite-element model in conjunction with previous experimental results revealed that the difference in apparent stiffness between tip and shank was due to differences in geometry, not intrinsic material properties [34].

## 1.2 Modeling Indentations

The interpretation of an indentation measurement with respect to subcellular structures, like the cell wall and turgor pressure, is dependent upon the selection of a mechanical model for the cell deformation. The appropriate selection of a mechanical model is dependent on the cell and indenter geometry [35], and on the stresses in the cell prior to indentation [36]. We can begin to understand the dependence on indenter geometry by considering the stress distribution in an isotropic, homogeneous, elastic half-plane under compression from a point load ( $F$ ). The Flamant solution provides exactly these expressions by applying the traction-free boundary condition at the surface of the elastic half-plane, except at the point directly underneath the point load to the governing equations of linear elasticity [37]. The resulting stresses are

$$\sigma_{xx} = -\frac{2F}{\pi} \frac{x^2 y}{(x^2 + y^2)^2} \quad (1.1)$$

$$\sigma_{yy} = -\frac{2F}{\pi} \frac{y^3 z}{(x^2 + y^2)^2} \quad (1.2)$$

$$\sigma_{xy} = -\frac{2F}{\pi} \frac{xy^2}{(x^2 + y^2)^2} \quad (1.3)$$

at a point  $(x,y)$  in the half-plane. The surface on which the maximum shear stress is constant is a circle. We can use the principle of linear superposition to determine the resulting stress field from a distributed load over a region of the surface. The surface on which the maximum shear stress is constant is elliptical, as pictured in Figure 1.3. The wider the region of indentation, the larger the resulting ellipse of constant maximum shear stress, and the deeper into the specimen the indentation test will probe. If our indenter is small relative to the thickness of the cell wall, then at shallow indentations most of the contact stress distribution will be isolated to the cell wall material. Then, a model which represents only the mechanics of the cell wall would be most appropriate. However, if the indenter is larger than the thickness of the cell wall, then even shallow indentations will cause non-negligible stresses to develop in the cytoplasm. In that case, a mechanical model which includes the effects of the cytoplasm would be necessary. A schematic of a cell under compression from different sized indenters is shown in Figure 1.3, and the exterior of the highlighted ellipse represents an approximate surface of constant maximum shear stress.

Mechanical models of walled cells under compression from a micro- or nano-indentation test in literature can be further classified into discrete and continuum

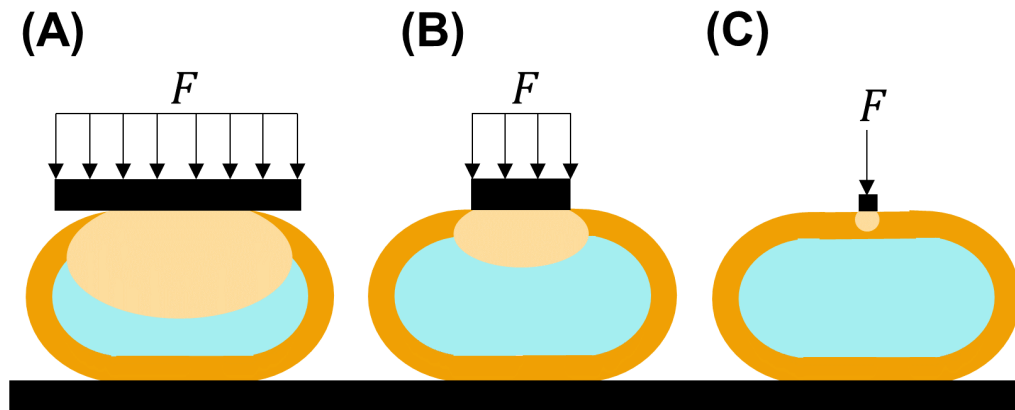


Figure 1.3: (A) Parallel plate geometry with exterior of highlighted region representing an approximate surface of constant maximum shear stress for the region of the cell in contact with the indenter. (B) Micro-indentation experiment geometry with exterior of highlighted region representing an approximate surface of constant maximum shear stress of the same magnitude as in (A) for the region of the cell in contact with the indenter. (C) Nano-indentation experiment geometry with exterior of highlighted region representing an approximate surface of constant maximum shear stress of the same magnitude as in (A) and (B).

models. Discrete models idealize the elastic response of the cell as one or more spring components. These models can be useful surrogates for a full description of the materials that constitute the cell. Continuum models describe the physics of a pressurized shell under compression. These models may be useful in separating the material properties of the constituent materials of the cell from the subcellular structure, but decoupling the contributions from each component to find a unique set of solutions from an indentation experiment is still an active area of research [14, 23, 29].

### Discrete Models

A discrete mechanical model of the elasticity of a cell under compression is one or more springs which deform a distance  $\Delta$  under compression from the load  $F$ . Hooke's law states that the linear constant which relates the deformation of each spring to the applied load on that spring is the spring constant  $k$  ( $F = k\Delta$ ). Two springs acting in parallel deform the same distance  $\Delta$ , and so the total resistance from both springs to the applied load is simply the sum of their constituent stiffnesses ( $k_{\text{effective}} = k_1 + k_2$ ). Two springs acting in series distribute the applied load equivalently between them, so a more compliant spring will deform a higher distance

than a stiffer spring. The equivalent stiffness for two springs in series is:

$$\frac{1}{k_{\text{effective}}} = \frac{1}{k_1} + \frac{1}{k_2} \quad (1.4)$$

A direct implication of the equivalent stiffness equation for two springs acting in series is that the effective stiffness of the overall assembly can only be as stiff as its softest component. Similarly, as the stiffness of one component approaches infinity (perfect rigidity), the stiffness of the other component dominates the compliance of the assembly.

### Single-Spring Model

The simplest mechanical model of a material is a one-dimensional spring which represents the entire body. This model is useful to represent an entire cell in indentation experiments with a relatively large probe because it removes the need to make any assumptions about the internal structure of the cell, and overall stiffness can be a reliable diagnostic for cell health. When cells are healthy and growing they maintain a higher turgor pressure and a correspondingly high cell wall stress state, which makes them appear stiffer overall. When the cell wall has been damaged, or the cell is under other environmental stress, they lose turgor pressure and appear softer overall. In micro-indentation experiments, the stiffness has been measured by interpolating the initial slope of the reaction force-indentation depth curve [15]. In nano-indentation experiments, the stiffness of the cell wall alone can be determined because the stress is located just underneath the small indenter, and is isolated to the cell wall [25].

However, it is not clear from a single spring model if a change in observed stiffness is achieved through a change in the cell wall stiffness or through a change in the internal turgor pressure. For example, a thickening of the cell wall may allow the cell to hold higher turgor pressure, so both the cell wall and the overall cell will appear stiffer under indentation. Alternatively, a higher environmental osmotic pressure may cause the turgor pressure inside the cell to increase to maintain equilibrium with the environment. As turgor pressure increases, the cell wall experiences higher stresses, and residual stresses are known to affect indentation measurements [29, 36]. So, both the cell wall and the overall cell may again appear stiffer under indentation in this stressed state, even though the mechanism for the stiffening is different. Discerning between these two mechanisms is important to further our understanding of fundamental cellular biology, and for more practical applications,

like understanding the mechanism by which a new antibiotic weakens an infectious bacterial species [38].

### **Two-Spring Model**

A natural extension of the single spring model is the addition of a second spring in series or in parallel. To my knowledge, I am the first to propose this type of discrete model for an isolated cell in an indentation experiment [39, 40]. The separation of stiffness contributions from the cell wall and cytoplasm allows further insight into the interactions between the mechanics of various subcellular structures. For example, in both types of plant cell studied using this model, the stiffness of the primary cell wall in hypoosmotic conditions was far beyond the stiffness of any other isolated component, including the underlying cytoplasm itself in hypoosmotic conditions. Others have observed cell wall stress stiffening of live plant and bacterial cells in response to turgor pressure, and we confirm this observation with a new type of cell and a new analysis [15, 29]. For more details on the two-spring model, see Chapters 2 and 3.

### **Continuum Models**

The most established method to model the mechanics of a walled cell under indentation is through continuum mechanics [13, 14, 22, 26, 28, 34]. Continuum models reveal the separate contributions of material properties and structure in overall stiffness measurements. For example, growing lily pollen tubes were believed to be softer at the tip and stiffer in the shank from micro-compression measurements of stiffness [33]. This was also in agreement with the differing biochemical composition of the cell wall in the tip and the shank [41]. However, a continuum FEM revealed that the material properties of the cell wall do not differ in these two locations of indentation, despite their difference in biochemical composition [34]. The difference in stiffness can be explained entirely through differences in geometry, which are not accounted for in discrete spring models.

The most commonly used model for the contact mechanics of a micro- or nano-indentation probe with a cell is the Hertz contact model [42], or some derivative thereof, like the Sneddon model for non-spherical indenter shapes [43] or the Johnson-Kendall-Roberts model for samples with high adhesion [44]. The Hertz model for contact between a sphere and an elastic half-space can be used to relate

the measured force ( $F$ ) and indentation depth ( $\Delta$ )

$$F = \frac{4}{3}E^*R^{\frac{1}{2}}\Delta^{\frac{3}{2}} \quad (1.5)$$

where  $R$  is the radius of the sphere and  $E^*$  is the plane strain Young's modulus of the elastic half-space. The plane strain Young's modulus is given by

$$E^* = \frac{E}{1 - \nu^2} \quad (1.6)$$

where  $E$  is the Young's modulus and  $\nu$  is the Poisson's ratio of the elastic half-space. This model is excellent for calculating the distribution of contact stresses in homogeneous materials. At shallow indentation depths, the material in contact with the indenter can often be assumed to be an infinite elastic half-space, because contact stresses do not develop outside of the homogeneous surface layer of material. In living and walled cells, the assumption of an elastic half-space quickly breaks down with increasing indentation depth, especially in Gram-negative bacteria where the thickness of the cell wall is only a few nanometers. In this case, the cell wall must be modeled as a material (typically a two-dimensional shell) which encapsulates the cytoplasm. A majority of these models can be categorized as constant pressure or constant volume models, depending on which constraint is placed on the fluid-filled cytoplasm.

### Constant Pressure Models

The most simplified models for this problem are those that assume constant zero pressure inside a shell under a point load. Reissner proposed the first solution to the shallow indentation of a hollow spherical shell under point load [45]. The solution provided by Reissner provides a linear relationship between the indentation depth ( $\Delta$ ) and the contact force ( $F$ )

$$F = \frac{8Et^2}{\sqrt{12(1 - \nu^2)}}\Delta \quad (1.7)$$

where  $E$  is the Young's modulus of the shell material,  $t$  is the thickness of the shell, and  $\nu$  is the Poisson ratio of the shell material.

Pogorelov described the mirror buckling effect observed in hollow spherical shells under large indentation from a point load [46]. Because this buckling phenomenon is an instability in the configuration of the shell, the indentation depth can be related to the geometry of the shell alone, which includes the radius of the spherical shell ( $R$ )

and the angle that the ridge of the buckled region makes with the vertical centerline of the shell ( $\alpha$ )

$$\Delta = 2R(1 - \cos \alpha). \quad (1.8)$$

Notice that the indentation depth does not depend on the applied load. This is the nature of a buckling instability; a large increase in deformation is possible without much increase in the applied load.

More recently, Vella et al. described the response of a spherical shell with a high internal pressure undergoing asymptotically small and large indentations [14]. For both small and large point loads, the relationship between indentation depth ( $\Delta$ ) and contact force ( $F$ ) is linear

$$F = k\Delta \quad (1.9)$$

For small point loads, the constant  $k = k_1$ , which is dependent on the geometry of the sphere, the pressure inside the shell, and the material properties of the shell

$$k_1 = \frac{4\pi D}{l_b^2 \sqrt{\tau^2 - 1}} \quad (1.10)$$

where  $D$  is the bending rigidity of the shell,  $l_b$  is the bending length scale, and  $\tau$  represents a dimensionless pressure. For large point loads, the constant  $k = k_2$ , which is again dependent on the geometry of the sphere and the pressure inside the shell

$$k_2 = \pi p R \quad (1.11)$$

where  $p$  is the pressure inside the sphere and  $R$  is the radius of the sphere.

In summary, the relationship between the contact force and indentation depth is linear for small indentations of unpressurized (Reissner) and pressurized shells (Vella et al.), albeit with a different constant. The contact force is proportional to the square root of the indentation depth for large indentations of unpressurized shells (Pogorelov), but the relationship becomes linear again for highly pressurized shells at large indentation depths (Vella et al.).

### Constant Volume Models

Numerical simulations have been carried out for a thick, fluid-filled shell with a constant volume in previous literature [47]. Simulations executed by Taber combined the solutions of Reissner and Pogorelov for spherical shells with no internal pressure with the stretching energy from fluid pressure inside a cell and bending energy

from the edges of the buckled region. The solution revealed a transition in the response of the fluid-filled spherical shell from one dominated by bending energy to one dominated by stretching energy after the indentation depth is greater than approximately 20% of the radius of the sphere.

### 1.3 Outline of This Thesis

This thesis is organized into three main chapters, excluding the introduction and conclusion chapters. Each chapter presents a different parameter fitting method which is matched with a mechanical model of the cell. The chapters are presented in order of increasing complexity of regression analysis and mechanical model. In Chapter 2, a simple analysis using the newly proposed two-spring model is used to determine the relative magnitude of each spring constant. This analysis is applied to micro-indentation data on differentiating *Arabidopsis thaliana* cells in different stages of differentiation and in solutions of different osmotic pressure. The analysis reveals that the primary cell wall under high stress from osmotic pressure is stiffer than the secondary cell wall, but the secondary cell wall is stiffer than the primary cell wall in plasmolyzing conditions. The analysis also reveals the first experimental evidence that differentiation leads to a measurable increase in the stiffness of the cytoplasm, which we suspect is due to bundling of the filaments of the cytoskeleton to prepare for deposition of the secondary cell wall. In Chapter 3, a Bayesian analysis of the two-spring model is used to determine the maximum a posteriori (MAP) spring stiffnesses that represent components of the cell wall and cytoplasm. The analyzed data come from micro-indentation experiments on *Nicotiana tabacum* cells in solutions of different osmotic pressures and with different drug treatments to remove specific filaments in the cytoskeleton. The results of the analysis from the two-spring models in Chapters 2 and 3 are validated using shallow nano-indentations to extract the Young's modulus of the isolated cell wall(s). Finally, in Chapter 4 an inverse analysis of a continuum model built using finite-element software is used to deeply explore the relationship between turgor pressure and cell wall stiffness in the Gram-negative bacterium *Escherichia coli*. I found that using the standard least squares regression would lead to a relationship between turgor pressure and Young's modulus that could not be decoupled with a single indentation measurement. However, using a combination of different objective functions, which isolate different facets of the force-indentation data, errors in the predicted CW modulus decreased by 15% and errors in the predicted turgor pressure decreased by 10% on average.

## References

- [1] Elisabeth Fischer-Friedrich et al. “Quantification of surface tension and internal pressure generated by single mitotic cells”. In: *Scientific Reports* 4.1 (Aug. 29, 2014). Number: 1 Publisher: Nature Publishing Group, p. 6213. ISSN: 2045-2322. DOI: 10.1038/srep06213. URL: <https://www.nature.com/articles/srep06213> (visited on 02/22/2021).
- [2] D. S. Cayley, H. J. Guttman, and M. T. Record. “Biophysical characterization of changes in amounts and activity of Escherichia coli cell and compartment water and turgor pressure in response to osmotic stress”. In: *Biophysical Journal* 78.4 (Apr. 2000), pp. 1748–1764. ISSN: 0006-3495. DOI: 10.1016/S0006-3495(00)76726-9.
- [3] Daniel J. Cosgrove. “Assembly and enlargement of the primary cell wall in plants”. In: *Annual Review of Cell and Developmental Biology* 13.1 (1997). PMID: 9442872, pp. 171–201. DOI: 10.1146/annurev.cellbio.13.1.171. eprint: <https://doi.org/10.1146/annurev.cellbio.13.1.171>. URL: <https://doi.org/10.1146/annurev.cellbio.13.1.171>.
- [4] Kenneth W. Foster. “Chapter 47 - Flagella, Cilia, Actin- and Centrin-based Movement”. In: *Cell Physiology Source Book (Fourth Edition)*. Ed. by Nicholas Sperelakis. San Diego: Academic Press, Jan. 1, 2012, pp. 823–853. ISBN: 978-0-12-387738-3. DOI: 10.1016/B978-0-12-387738-3.00047-0. URL: <https://www.sciencedirect.com/science/article/pii/B9780123877383000470> (visited on 02/22/2021).
- [5] Wieland Fricke. “Turgor Pressure”. In: *eLS*. Ed. by John Wiley & Sons Ltd. Chichester, UK: John Wiley & Sons, Ltd, Jan. 16, 2017, pp. 1–6. ISBN: 978-0-470-01590-2 978-0-470-01617-6. DOI: 10.1002/9780470015902.a0001687.pub2. URL: <http://doi.wiley.com/10.1002/9780470015902.a0001687.pub2> (visited on 02/04/2021).
- [6] Daniel J. Cosgrove, Elizabeth Van Volkenburgh, and Robert E. Cleland. “Stress relaxation of cell walls and the yield threshold for growth”. In: *Planta* 162.1 (Sept. 1, 1984), pp. 46–54. ISSN: 1432-2048. DOI: 10.1007/BF00397420. URL: <https://doi.org/10.1007/BF00397420> (visited on 02/22/2021).
- [7] Fred Chang and Kerwyn Casey Huang. “How and why cells grow as rods”. In: *BMC Biology* 12.1 (Aug. 2, 2014), p. 54. ISSN: 1741-7007. DOI: 10.1186/s12915-014-0054-8. URL: <https://doi.org/10.1186/s12915-014-0054-8> (visited on 02/22/2021).
- [8] E. Steudle. “Pressure probe techniques: basic principles and application to studies of water and solute relations at the cell, tissue and organ level”. In: *Water deficits* (1993), pp. 5–36. URL: <https://docuserve.library.caltech.edu/illiad/illiad.dll?Action=10&Form=75&Value=531985> (visited on 02/05/2021).

- [9] A. Deri Tomos and Roger A. Leigh. “THE PRESSURE PROBE: A Versatile Tool in Plant Cell Physiology”. In: *Annual Review of Plant Physiology and Plant Molecular Biology* 50.1 (1999), pp. 447–472. DOI: 10.1146/annurev.arplant.50.1.447. URL: <https://doi.org/10.1146/annurev.arplant.50.1.447> (visited on 02/04/2021).
- [10] Roger R. Lew. “How does a hypha grow? The biophysics of pressurized growth in fungi”. In: *Nature Reviews Microbiology* 9.7 (July 2011). Number: 7 Publisher: Nature Publishing Group, pp. 509–518. ISSN: 1740-1534. DOI: 10.1038/nrmicro2591. URL: <https://www.nature.com/articles/nrmicro2591> (visited on 02/04/2021).
- [11] Anthony Edward Walsby. “The pressure relationships of gas vacuoles”. In: *Proceedings of the Royal Society of London. Series B. Biological Sciences* 178.1052 (Aug. 3, 1971), pp. 301–326. ISSN: 0080-4649, 2053-9193. DOI: 10.1098/rspb.1971.0067. URL: <https://royalsocietypublishing.org/doi/10.1098/rspb.1971.0067> (visited on 02/04/2021).
- [12] Raymond W. Bourdeau et al. “Acoustic reporter genes for noninvasive imaging of microorganisms in mammalian hosts”. In: *Nature* 553.7686 (Jan. 3, 2018), pp. 86–90. ISSN: 1476-4687. DOI: 10.1038/nature25021.
- [13] M. Arnoldi et al. “Bacterial turgor pressure can be measured by atomic force microscopy”. In: *Physical Review. E, Statistical Physics, Plasmas, Fluids, and Related Interdisciplinary Topics* 62.1 (July 2000), pp. 1034–1044. ISSN: 1063-651X. DOI: 10.1103/physreve.62.1034.
- [14] Dominic Vella et al. “The indentation of pressurized elastic shells: from polymeric capsules to yeast cells”. In: *Journal of The Royal Society Interface* 9.68 (Mar. 7, 2012), pp. 448–455. ISSN: 1742-5689, 1742-5662. DOI: 10.1098/rsif.2011.0352. URL: <https://royalsocietypublishing.org/doi/10.1098/rsif.2011.0352> (visited on 11/11/2019).
- [15] Anne-Lise Routier-Kierzkowska et al. “Cellular Force Microscopy for in Vivo Measurements of Plant Tissue Mechanics”. In: *Plant Physiology* 158.4 (2012), pp. 1514–1522. ISSN: 0032-0889. DOI: 10.1104/pp.111.191460. eprint: <http://www.plantphysiol.org/content/158/4/1514.full.pdf>. URL: <http://www.plantphysiol.org/content/158/4/1514>.
- [16] Gang Bao and Subra Suresh. “Cell and molecular mechanics of biological materials”. In: *Nature materials* 2.11 (2003), pp. 715–725.
- [17] Amir J Bidhendi and Anja Geitmann. “Methods to quantify primary plant cell wall mechanics”. In: *Journal of Experimental Botany* 70.14 (July 2019), pp. 3615–3648. ISSN: 0022-0957. DOI: 10.1093/jxb/erz281. eprint: <https://academic.oup.com/jxb/article-pdf/70/14/3615/28985115/erz281.pdf>. URL: <https://doi.org/10.1093/jxb/erz281>.

- [18] S Aguayo et al. “Single-bacterium nanomechanics in biomedicine: unravelling the dynamics of bacterial cells”. In: *Nanotechnology* 26.6 (2015), p. 062001.
- [19] Alexis Peaucelle, Raymond Wightman, and Herman Höfte. “The control of growth symmetry breaking in the *Arabidopsis hypocotyl*”. In: *Current Biology* 25.13 (2015), pp. 1746–1752.
- [20] Siobhan A. Braybrook and Alexis Peaucelle. “Mechano-Chemical Aspects of Organ Formation in *Arabidopsis thaliana*: The Relationship between Auxin and Pectin”. In: *PLOS ONE* 8.3 (Mar. 2013), pp. 1–10. DOI: 10.1371/journal.pone.0057813. URL: <https://doi.org/10.1371/journal.pone.0057813>.
- [21] Chung-Souk Han, Seyed HR Sanei, and Farid Alisafaei. “On the origin of indentation size effects and depth dependent mechanical properties of elastic polymers”. In: *Journal of Polymer Engineering* 36.1 (2016), pp. 103–111.
- [22] Ksenija Radotić et al. “Atomic force microscopy stiffness tomography on living *Arabidopsis thaliana* cells reveals the mechanical properties of surface and deep cell-wall layers during growth”. eng. In: *Biophysical Journal* 103.3 (Aug. 2012), pp. 386–394. ISSN: 1542-0086. DOI: 10.1016/j.bpj.2012.06.046.
- [23] Pascale Milani, Siobhan A. Braybrook, and Arezki Boudaoud. “Shrinking the hammer: micromechanical approaches to morphogenesis”. In: *Journal of Experimental Botany* 64.15 (July 2013), pp. 4651–4662. ISSN: 0022-0957. DOI: 10.1093/jxb/ert169. eprint: <https://academic.oup.com/jxb/article-pdf/64/15/4651/18043081/ert169.pdf>. URL: <https://doi.org/10.1093/jxb/ert169>.
- [24] Arun Sampathkumar et al. “Subcellular and supracellular mechanical stress prescribes cytoskeleton behavior in *Arabidopsis* cotyledon pavement cells”. In: *eLife* 3 (Apr. 2014). Ed. by Dominique Bergmann, e01967. ISSN: 2050-084X. DOI: 10.7554/eLife.01967. URL: <https://doi.org/10.7554/eLife.01967>.
- [25] Siobhan A. Braybrook. “Chapter 13 - Measuring the elasticity of plant cells with atomic force microscopy”. In: *Biophysical Methods in Cell Biology*. Ed. by Ewa K. Paluch. Vol. 125. Methods in Cell Biology. Academic Press, 2015, pp. 237–254. DOI: <https://doi.org/10.1016/bs.mcb.2014.10.006>. URL: <http://www.sciencedirect.com/science/article/pii/S0091679X14000077>.
- [26] Elham Forouzesh et al. “In vivo extraction of *Arabidopsis* cell turgor pressure using nanoindentation in conjunction with finite element modeling”. In: *The Plant Journal* 73.3 (2013), pp. 509–520.

- [27] Léna Beauzamy, Julien Derr, and Arezki Boudaoud. “Quantifying hydrostatic pressure in plant cells by using indentation with an atomic force microscope”. In: *Biophysical journal* 108.10 (2015), pp. 2448–2456.
- [28] Alain Weber et al. “Measuring the mechanical properties of plant cells by combining micro-indentation with osmotic treatments”. In: *Journal of Experimental Botany* 66.11 (Apr. 2015), pp. 3229–3241. ISSN: 0022-0957. DOI: [10.1093/jxb/erv135](https://doi.org/10.1093/jxb/erv135). eprint: <https://academic.oup.com/jxb/article-pdf/66/11/3229/17137090/erv135.pdf>. URL: <https://doi.org/10.1093/jxb/erv135>.
- [29] Yi Deng, Mingzhai Sun, and Joshua W. Shaevitz. “Direct Measurement of Cell Wall Stress Stiffening and Turgor Pressure in Live Bacterial Cells”. In: *Physical Review Letters* 107.15 (Oct. 6, 2011). Publisher: American Physical Society, p. 158101. DOI: [10.1103/PhysRevLett.107.158101](https://doi.org/10.1103/PhysRevLett.107.158101). URL: <https://link.aps.org/doi/10.1103/PhysRevLett.107.158101> (visited on 02/07/2021).
- [30] Alexis Peaucelle et al. “Pectin-induced changes in cell wall mechanics underlie organ initiation in Arabidopsis”. In: *Current biology* 21.20 (2011), pp. 1720–1726.
- [31] D. B. MacManus et al. “Dynamic mechanical properties of murine brain tissue using micro-indentation”. In: *Journal of Biomechanics* 48.12 (Sept. 18, 2015), pp. 3213–3218. ISSN: 0021-9290. DOI: [10.1016/j.jbiomech.2015.06.028](https://doi.org/10.1016/j.jbiomech.2015.06.028). URL: <https://www.sciencedirect.com/science/article/pii/S002192901500370X> (visited on 02/24/2021).
- [32] Camilo Velez, Robin E. Carroll, and David P. Arnold. “Direct measurement and microscale mapping of nanoNewton to milliNewton magnetic forces”. In: *AIP Advances* 7.5 (Mar. 7, 2017). Publisher: American Institute of Physics, p. 056809. DOI: [10.1063/1.4978316](https://doi.org/10.1063/1.4978316). URL: <https://aip.scitation.org/doi/full/10.1063/1.4978316> (visited on 02/24/2021).
- [33] Dimitris Felekis et al. “Quantifying growth mechanics of living, growing plant cells in situ using microrobotics”. In: *Micro & Nano Letters* 6.5 (2011), pp. 311–316.
- [34] Hannes Vogler et al. “The pollen tube: a soft shell with a hard core”. In: *The Plant Journal* 73.4 (2013), pp. 617–627.
- [35] J.-E. Bolduc et al. “Finite-element analysis of geometrical factors in micro-indentation of pollen tubes”. In: *Biomechanics and Modeling in Mechanobiology* 5.4 (Nov. 2006), pp. 227–236. ISSN: 1617-7959. DOI: [10.1007/s10237-005-0010-1](https://doi.org/10.1007/s10237-005-0010-1).
- [36] Evan A. Zamir and Larry A. Taber. “On the effects of residual stress in microindentation tests of soft tissue structures”. In: *Journal of Biomechan-*

- ical Engineering* 126.2 (Apr. 2004), pp. 276–283. ISSN: 0148-0731. DOI: 10.1115/1.1695573.
- [37] A Flamant et al. “Sur la répartition des pressions dans un solide rectangulaire chargé transversalement”. In: *CR Acad. Sci. Paris* 114 (1892), pp. 1465–1468.
- [38] Catherine Volle et al. “Measuring the Effect of Antimicrobial Peptides on the Biophysical Properties of Bacteria using Atomic Force Microscopy”. In: *Biophysical Journal* 114.3 (Feb. 2018), 354a. ISSN: 00063495. DOI: 10.1016/j.bpj.2017.11.1969. URL: <https://linkinghub.elsevier.com/retrieve/pii/S0006349517332010> (visited on 02/16/2021).
- [39] Leah Ginsberg et al. “Structure and Biomechanics during Xylem Vessel Transdifferentiation in *Arabidopsis thaliana*”. en. In: *Plants* 9.12 (Dec. 2020), p. 1715. ISSN: 2223-7747. DOI: 10.3390/plants9121715. URL: <https://www.mdpi.com/2223-7747/9/12/1715>.
- [40] Leah Ginsberg et al. “Cell wall and cytoskeletal contributions in single cell biomechanics of *Nicotiana tabacum*”. In: *Plant and Cell Physiology* (In review).
- [41] C Ferguson et al. “Location of cellulose and callose in pollen tubes and grains of *Nicotiana tabacum*”. In: *Planta* 206.3 (1998), pp. 452–460.
- [42] H. Hertz. “Über die Berührung fester elastischer Körper (On the contact of elastic solids)”. In: *Journal für die reine und angewandte Mathematik* 82 (1882), pp. 156–171.
- [43] Ian N. Sneddon. “The relation between load and penetration in the axisymmetric boussinesq problem for a punch of arbitrary profile”. In: *International Journal of Engineering Science* 3.1 (May 1, 1965), pp. 47–57. ISSN: 0020-7225. DOI: 10.1016/0020-7225(65)90019-4. URL: <https://www.sciencedirect.com/science/article/pii/0020722565900194> (visited on 02/23/2021).
- [44] Kenneth Langstreth Johnson et al. “Surface energy and the contact of elastic solids”. In: *Proceedings of the Royal Society of London. A. Mathematical and Physical Sciences* 324.1558 (Sept. 8, 1971). Publisher: Royal Society, pp. 301–313. DOI: 10.1098/rspa.1971.0141. URL: <https://royalsocietypublishing.org/doi/10.1098/rspa.1971.0141> (visited on 02/23/2021).
- [45] Eric Reissner. “Stresses and Small Displacements of Shallow Spherical Shells. I”. In: *Journal of Mathematics and Physics* 25.1 (Apr. 1946), pp. 80–85. ISSN: 00971421. DOI: 10.1002/sapm194625180. URL: <http://doi.wiley.com/10.1002/sapm194625180> (visited on 11/06/2019).

- [46] A Pogorelov. *Bendings of Surfaces and Stability of Shells*. Vol. 72. Translations of Mathematical Monographs. Providence, Rhode Island: American Mathematical Society, 1988. ISBN: 978-0-8218-4525-7 978-1-4704-4486-0. DOI: 10.1090/mmono/072. URL: <http://www.ams.org/mmono/072> (visited on 02/03/2021).
- [47] L. A. Taber. “Large Deflection of a Fluid-Filled Spherical Shell Under a Point Load”. In: *Journal of Applied Mechanics* 49.1 (Mar. 1, 1982), pp. 121–128. ISSN: 0021-8936, 1528-9036. DOI: 10.1115/1.3161953. URL: <https://asmedigitalcollection.asme.org/appliedmechanics/article/49/1/121/388706/Large-Deflection-of-a-FluidFilled-Spherical-Shell> (visited on 11/06/2019).

*Chapter 2***STRUCTURE AND BIOMECHANICS DURING XYLEM  
VESSEL TRANSDIFFERENTIATION IN *ARABIDOPSIS  
THALIANA***

This chapter is adapted from:

- [1] Leah Ginsberg et al. “Structure and Biomechanics during Xylem Vessel Transdifferentiation in *Arabidopsis thaliana*”. en. In: *Plants* 9.12 (Dec. 2020), p. 1715. ISSN: 2223-7747. DOI: 10.3390/plants9121715. URL: <https://www.mdpi.com/2223-7747/9/12/1715>.

**Abstract**

Individual plant cells are the building blocks for all plantae and artificially constructed plant biomaterials, like biocomposites. Secondary cell walls (SCWs) are a key component for mediating mechanical strength and stiffness in both living vascular plants and biocomposite materials. In this chapter, we study the structure and biomechanics of cultured plant cells during the cellular developmental stages associated with SCW formation. We use a model culture system that induces transdifferentiation of *Arabidopsis thaliana* cells to xylem vessel elements, upon treatment with dexamethasone (DEX). We group the transdifferentiation process into three distinct stages, based on morphological observations of the cell walls. The first stage includes cells with only a primary cell wall (PCW), the second covers cells that have formed a SCW, and the third stage includes cells with a ruptured tonoplast and partially or fully degraded PCW. We adopt a multi-scale approach to study the mechanical properties of cells in these three stages. We perform large-scale indentations with a micro-compression system in three different osmotic conditions. Atomic force microscopy (AFM) nanoscale indentations in water allow us to isolate the cell wall response. We propose a spring-based model to deconvolve the competing stiffness contributions from turgor pressure, PCW, SCW and cytoplasm in the stiffness of differentiating cells. Prior to triggering differentiation, cells in hypotonic pressure conditions are significantly stiffer than cells in isotonic or hypertonic conditions, highlighting the dominant role of turgor pressure. Plasmolyzed cells with a SCW reach similar levels of stiffness as cells with maximum turgor pressure.

The stiffness of the PCW in all of these conditions is lower than the stiffness of the fully-formed SCW. Our results provide the first experimental characterization of the mechanics of SCW formation at single cell level.

**Keywords:** plant biomechanics; turgor pressure; micro-compression; AFM; *Arabidopsis thaliana*; differentiation

## 2.1 Introduction

Plantae and plant-based materials are specialized conglomerates of plant cells. Therefore, studying the mechanical properties of single cells and resolving further sub-cellular contributions provides a basis for further analysis of the heterogeneous tissue and plant-level biomechanics. In vascular plant tissues, the micro-structure and composition of secondary cell wall (SCW) governs, to a large extent, the mechanical properties of the entire tissue [48, 49]. Thus, it is of paramount importance to investigate the mechanical properties of the SCW, especially during the initial stages of formation, which have not been explored to date.

Plant cells have two key structural elements that collectively govern their mechanical properties: the cell wall and the cytoskeleton. The key structural component of the cell wall is cellulose, which has a Young's modulus ( $E = 110\text{--}220$  GPa) comparable to that of high-performance engineering materials like carbon fiber or steel [50]. Cellulose is immersed in an amorphous matrix of softer biopolymers, hemicellulose, pectin, proteins, and lignin, giving rise to a complex heterogeneous multilayered cell wall structure [51]. The support provided to plant cells by the cell wall allows them to hold water at high pressures ( $p = 0.3\text{--}1.0$  MPa), mainly through swelling of the vacuole [3]. This phenomenon in plants is known as turgor pressure, and it is essential to the structural integrity and rigidity of the cell. Additional structural support is provided to the cell by the cytoskeleton, largely through actin filaments ( $E = 1.0\text{--}4.0$  kPa) and microtubules ( $E = 1.1\text{--}1.3$  GPa) [52–54]. In the same work, plant cells were treated with a microtubule destabilizing drug, which reduced the elastic modulus of the protoplast to half of its original value, demonstrating that microtubules (MTs) contribute to the overall stiffness of the cell. Sampathkumar et al. used live-imaging of *Arabidopsis thaliana* (*Arabidopsis*) plants, particularly in epithelial cells, and a mechanistic model to find that there is a direct correlation between microtubule organization and geometry-derived mechanical stresses [24]. Apparently, the maximum stress in the cell wall is found in areas with highest cellulose concentration, which is driven by the MTs in the cytoplasm. Taken

together, the results of Durand-Smet et al. and Sampathkumar et al. show that MTs contribute to the overall stiffness of cells intrinsically, and through an interaction with the cell wall. Here, in order to understand the mechanical contributions of the subcellular components, like the cell wall(s) and cytoplasm, throughout the transdifferentiation process, we propose a robust multi-scale mechanics assay that includes nano-indentation to capture cell wall properties, chemical treatments to control osmotic conditions and micro-indentation to evaluate global cell properties.

We choose to focus on xylem vessel element differentiation, which is one of the most extensively used systems to study SCW development and thickening [55, 56]. Xylem vessel elements develop a precisely patterned SCW beneath the primary cell wall (PCW), giving rise to an entangled multilayered heterostructure. The deposition of SCW in xylem vessel elements is intricately linked to programmed cell death (PCD), and both processes are happening concurrently during differentiation [57]. Therefore, quantifying the mechanical contributions of the cell wall(s) and cytoplasm during differentiation of xylem vessel elements is a convoluted problem, and one that has not yet been solved. Our multi-scale biomechanical assay is designed to capture mechanical contributions from the PCW, the SCW, their potential coupled effects, as well as the cytoskeleton at various turgor pressures and osmotic conditions.

Early in vitro SCW induction systems for *Zinnia elegans* facilitated physiological, biochemical, and molecular studies that elucidated the tracheary element (TE) differentiation mechanism [58–60]. The Demura group introduced the post-translational induction system of VASCULAR-RELATED NAC-DOMAIN7 (VND7) genes which induce transdifferentiation of various types of plant cells into xylem vessel elements upon treatment with a glucocorticoid, such as dexamethasone (DEX) [55, 56]. The induction system has been demonstrated successfully in Arabidopsis plants and cell cultures, as well as *Populus tremula x tremuloides* plantlets, and *Nicotiana tabacum* cell cultures [55]. The system causes the activation of transcriptional activity of VND7 to induce ectopic transdifferentiation of Arabidopsis cultured cells into protoxylem vessel-like cells [55].

In this study, we use the VND7 system in Arabidopsis suspension-culture cells because it is a robust model with a high efficiency in transdifferentiation and uniformity in cell culture. To decouple the effects of cell wall stress, cytoskeleton rearrangement, and turgor pressure on observed cell stiffness, we test transgenic Arabidopsis cells in an extensive multi-scale biomechanical assay. To validate the

cell wall stiffness decoupled from turgor pressure, we perform AFM indentations [61]. We propose a mechanistic spring model to represent the stiffness of the cell in compression, which allows the decoupling of stiffness contributions from the cell wall(s) and cytoplasm.

## 2.2 Results and Discussion

### Morphological Observations of the VND7-Inducible Arabidopsis Cells

The VND7-inducible Arabidopsis cells were stained and observed under a laser scanning confocal microscope at various stages of their differentiation. We document that transdifferentiation of VND7-inducible cells follows the same general stages as TE differentiation seen in other plant systems [58–60]. Common morphological observations during differentiation of TEs in *Zinnia elegans*, *Populus deltoides*, and Arabidopsis, in the order that they occur, are: (i) the differentiating cell expands and becomes highly vacuolated and the nucleus is confined, pushing against the cell wall and marking the initiation of PCD; (ii) the cytoskeleton rearranges as the cell produces vesicles which have been associated with substance exchange between the cytoplasm and cell wall for SCW deposition; (iii) tonoplast ruptures as SCW is deposited and starts thickening; (iv) following SCW thickening, in planta, PCW perforation is observed [57, 62–64]. From the transmitted and confocal fluorescent images, as well as optical microscopy images (see Figure 2.6A–C), we can robustly identify three distinct stages of cell transdifferentiation based on the cell wall(s) and cytoplasm, as presented in Figure 2.1A–F. Specifically, in the VND7 system we study in this work, we classify the stages as follows: (i) Stage 0: cells prior to induction of transdifferentiation (prior to adding DEX in the solution), having only a PCW developed and visible. (ii) Stage 1: cells having been induced (exposed to DEX for a minimum of 24 h) and having only a PCW developed. (iii) Stage 2: cells having been induced (exposed to DEX for a minimum of 24 h) and having an intact PCW and a SCW developed. The cytoplasmic contents of these cells are visible and still inside the cell. In our observations, cytoplasm retraction and detachment from the cell wall happens soon after SCW deposition. (iv) Stage 3: cells having been induced (exposed to DEX for a minimum of 48 h) having a thickened SCW, and partially perforated PCW. With or without perforated PCW, in stage 3 the majority of cytoplasmic contents are removed from the cells (indicating the tonoplast rupture). Using the confocal fluorescent images, we compile three-dimensional reconstructions for each identifiable stage of transdifferentiation, presented in Figure 2.1G–I, which allow the evaluation of the PCW thickness, as

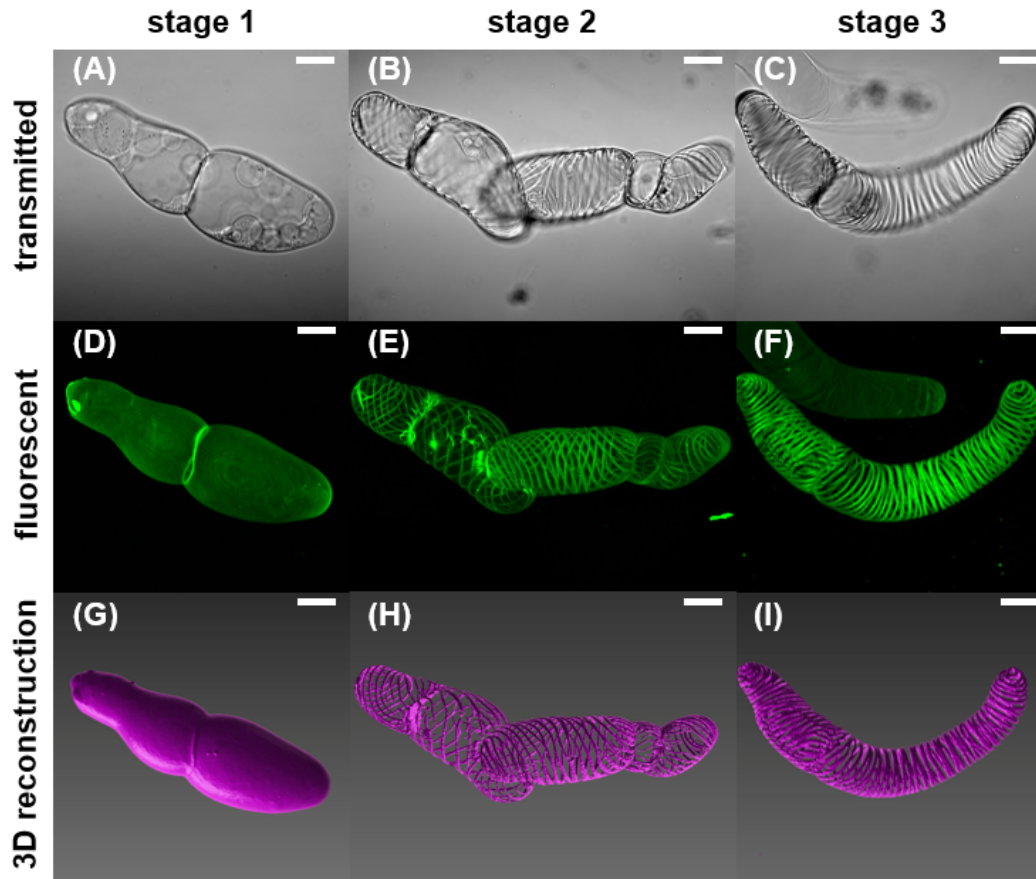


Figure 2.1: Transmitted, fluorescent, and 3D reconstructions of confocal images of the elongated VND7-inducible cells in the three stages of transdifferentiation. (A,D,G) Living cells which have only developed a PCW are identified as stage 1. The PCW is under stress from the internal turgor pressure. (B,E,H) Cells in stage 2 have both a PCW and the beginnings of a SCW. In this stage, the PCW has possibly begun hydrolyzing, and thin spiral bundles of SCW can be distinguished. The spiral patterning is characteristic of protoxylem vessels. (C,F,I) In stage 3, SCW thickening is observed; PCD has progressed; the tonoplast has ruptured and cytoplasmic contents have been removed from the cell. All scale bars are 20  $\mu\text{m}$ .

well as visualization of the bundled SCW thickenings.

From confocal and additional light microscopy images (data not presented here), we discern two equally represented shapes in the cell population, based on their aspect ratio: rounded and elongated. Elongated cells have a mean aspect ratio of approximately 2:1, whereas rounded cells have a mean aspect ratio of approximately 1:1. Even though the microscopy images denote that approximately half of the population of cells are rounded, and half are elongated, we observe that rounded cells tend to be tightly clustered, while elongated cells are found more likely in an

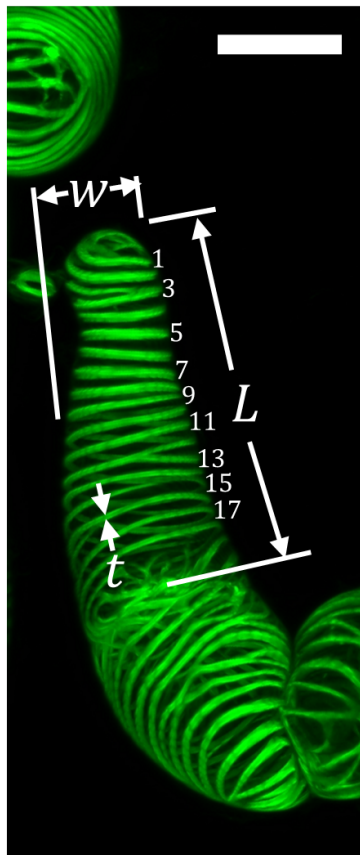


Figure 2.2: Illustration of measured principal dimensions and feature sizes of elongated VND7-inducible cells from confocal fluorescent microscopy image. Scale bar is 20  $\mu\text{m}$ .

isolated state or located on the edges of large clusters. For that reason, all mechanical data in the following sections are measured from elongated cells, and we will focus on the morphology of those cells in this section. For all dimensions and feature sizes of both rounded and elongated cells, see Tables 2.2 and 2.3. The principal dimensions and feature sizes of elongated cells, along with an illustrative example, are shown in Table 2.1 and Figure 2.2, respectively.

Confocal imaging reveals a PCW in stage 1 (thickness  $580 \pm 10$  nm (Mean  $\pm$  Standard Error)), while bundles of SCW in spiral patterns are observed in stages 2 and 3 of transdifferentiation. In stage 2, the early SCW bundles are deposited, and the cell begins to undergo PCD. In stage 3, as PCD progresses, the SCW bundles are thickened further, the tonoplast ruptures, contents of the cytoplasm are degraded and removed from the cell, and the PCW is at least partially hydrolyzed [49]. (See Figure 2.7 for partial PCW perforation at stage 3). During the last stage of differentiation,

Table 2.1: Measured principal dimensions and feature sizes of elongated VND7-inducible cells in the three stages of transdifferentiation. Length ( $L$ ), width ( $w$ ), and thickness ( $t$ ) of SCW bundles are measured using image processing. Volume ( $V$ ) is calculated from measured length and width, assuming cells are cylindrical in shape. The density of SCW bundles ( $\rho$ ) is calculated by counting the number of bundles observed in a particular cell, and dividing by the cross-sectional area in the image.

<b>Dimension</b>	<b>Mean <math>\pm</math> SE</b>
$L_{\text{stage 1}}$ ( $\mu\text{m}$ )	$60.4 \pm 2.4$
$L_{\text{stage 2}}$ ( $\mu\text{m}$ )	$56.4 \pm 4.9$
$L_{\text{stage 3}}$ ( $\mu\text{m}$ )	$61.6 \pm 3.7$
$w_{\text{stage 1}}$ ( $\mu\text{m}$ )	$30.7 \pm 1.0$
$w_{\text{stage 2}}$ ( $\mu\text{m}$ )	$31.2 \pm 2.8$
$w_{\text{stage 3}}$ ( $\mu\text{m}$ )	$34.7 \pm 1.6$
$V_{\text{stage 1}}$ ( $\mu\text{m}^3$ )	$44,700 \pm 2100$
$V_{\text{stage 2}}$ ( $\mu\text{m}^3$ )	$43,100 \pm 5300$
$V_{\text{stage 3}}$ ( $\mu\text{m}^3$ )	$58,300 \pm 4100$
$\rho_{\text{stage 2}}$ ( $\#/\mu\text{m}^2$ )	$0.056 \pm 0.005$
$\rho_{\text{stage 3}}$ ( $\#/\mu\text{m}^2$ )	$0.060 \pm 0.004$
$t_{\text{stage 2}}$ ( $\mu\text{m}$ )	$1.05 \pm 0.01$
$t_{\text{stage 3}}$ ( $\mu\text{m}$ )	$1.45 \pm 0.01$

the SCW bundles thicken by approximately 40%. The bundle density does not change notably between stages 2 and 3.

### **Biomechanics of Differentiating VND7-Inducible Arabidopsis Cells**

All reported mechanical data in the following sections are measured from elongated cells in an isolated state. In the mechanical testing, we add stage 0 to the differentiation stages, which describes transgenic cells prior to exposure to DEX, reflecting cells in their state before transdifferentiation is induced. There is no observable difference between stages 0 and 1 using the confocal or light microscope, but it has been reported that from stage 0 to 1, the MT and actin filaments reorganize the cytoplasmic fibrillar network into a bundled conformation that will later guide the spiral SCW patterning [65, 66]. In fact, the MT-rearrangement in particular has been visualized in the VND7-inducible system and has been reported in literature [67].

The elongated cells were compressed using a micro-compression tool that covered most of their top surface area. We propose a spring model to describe the overall cell stiffness, as pictured in Figure 2.3. The pictured model has two springs in

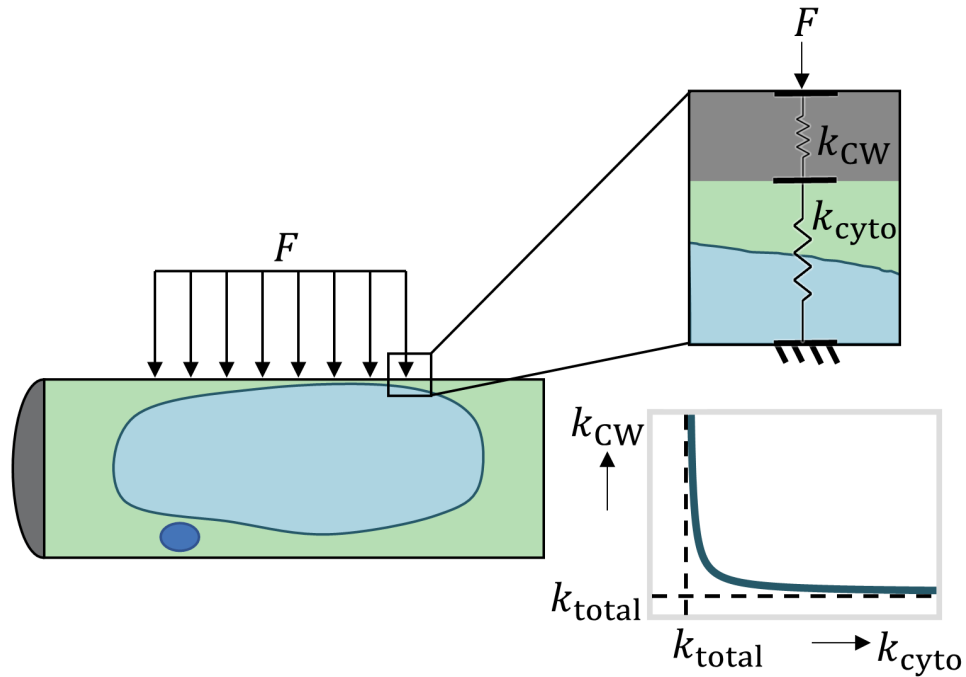


Figure 2.3: Proposed series spring model to analyze cell stiffness from micro-compression testing. The total stiffness measured by the micro-compression tool is the equivalent stiffness for the two springs in series, given by Equation (2.1), and it must be less than the intrinsic stiffness of either constituent spring in the series. For a given overall stiffness,  $k_{total}$ , the included plot illustrates the relationship between the stiffness of the two springs,  $k_{CW}$  and  $k_{cyto}$ .

series, one which represents the stiffness of the cell wall, and the other represents the stiffness of the cytoplasm. The combined stiffness of these two springs is given by the following equation:

$$k_{total} = \frac{k_{CW}k_{cyto}}{k_{CW} + k_{cyto}}. \quad (2.1)$$

A direct result of using this model is that the overall stiffness must be less than the stiffness of either constituent springs. In the following sections we will use this proposed model to deconvolute the stiffness contributions from the cell wall(s) and cytoplasm. The result is a ranking of the stiffness contributions from the cell wall(s) and cytoplasm in each stage of differentiation. It is important to note that this ranking depends on the validity of the assumptions outlined in the following paragraph.

In using this simplified model, we assume that the cell wall and cytoplasm behave as linear elastic materials at small indentation depths, and we ignore any nonlinear

effects like adhesion, viscosity, or plasticity. For shallow indentations, the effects from stress at the boundaries of the cell also become negligible [68]. This simplified one-dimensional model allows us to quantify the relative stiffness contributions of each component. Stiffness is not an intrinsic material property, like Young's modulus which is independent of the shape and dimensions of the material, since by definition stiffness is a function of both the material and its geometry. To relate spring stiffness to Young's modulus would require a three-dimensional model which captures the structural mechanics of a pressurized cell with a heterogeneous membrane undergoing large deformations. Due to the lack of such a model in the current literature, we adopt this one-dimensional spring model, which allows us to decouple the relative contributions from the cytoplasm and cell wall(s), although we cannot yet directly obtain intrinsic material properties for either component. See Figure 2.8 for the specific spring models used to represent cells in each stage of transdifferentiation, and in each solution with different osmolarity.

For the micro-indentation tests, we extract cells from their normal growth conditions (in growth media) at different time points before and after exposure to DEX, from 24 h to several days, evaluate their morphology in an optical microscope (see Figure 2.6A–C), and identify their stage of transdifferentiation. Testing of cells at different time points after exposure to DEX allows us to capture them at each of the four identified differentiation stages. We confirm the stage of differentiation and cell morphology through the optical microscope embedded in the micro-mechanical testing system (see Figure 2.6D–F). After the extraction from normal growth conditions, we treat the cells in three different osmotic conditions and maintain them during the mechanical testing, which is conducted in solution. We refer to the testing conditions as hypertonic, when cells are in sorbitol, isotonic, when cells are in growth media, and hypotonic, when cells are in deionized water. See Table 2.4 for details on the calculation of the osmotic pressure in each solution. In hypertonic conditions, the cells are visibly plasmolyzed as evident from optical microscopy images after the first minute of exposure to sorbitol (see Figure 2.9). We note that the plasmolysis is evident for cells in stages 0–2 when the cytoplasm is still inside the cells. In isotonic and hypotonic conditions, the cell physiology as studied by optical microscopy is the same as in their normal growth conditions (cells are turgid, cytoplasm pushing against the cell wall). While we refer to cells treated with growth media as being in an isotonic condition, they are turgid, and the turgor pressure drives their growth and development. We use the term isotonic in a relative sense, as compared to the high osmotic pressure differential in hypotonic conditions. In the

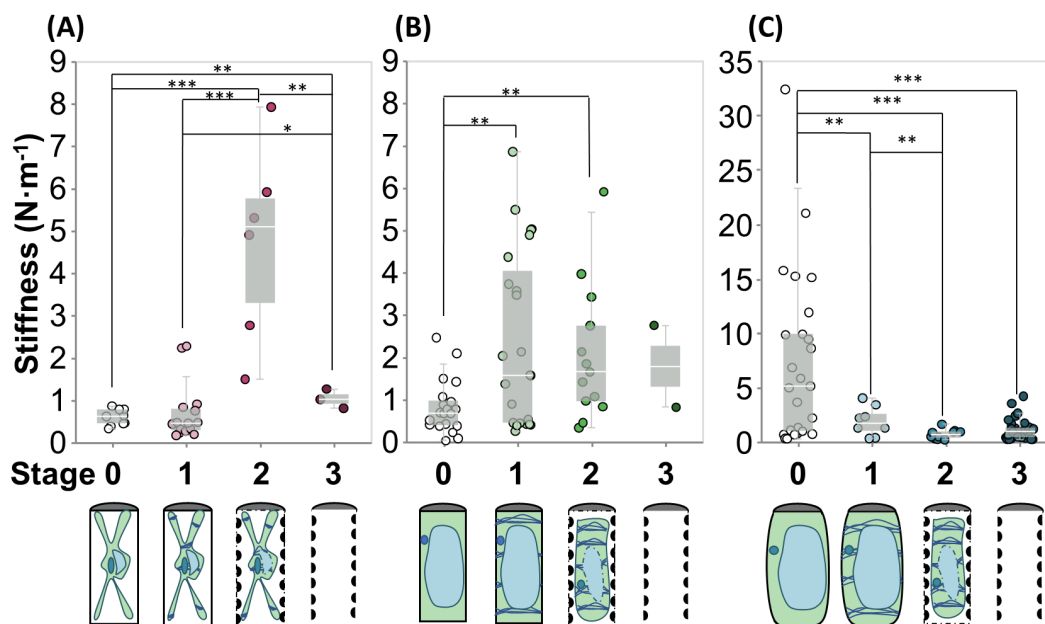


Figure 2.4: Panel showing the stiffness in four stages of transdifferentiation in three types of solutions with different osmolarity: (A) sorbitol; (B) growth medium; (C) water. Note the difference in scale on the y-axis in (C) from the extreme stiffness of cells in hypotonic conditions before induction of differentiation. Bottom line graphically represents the morphology of the cells in each condition and stage. Stars indicate significant differences in distribution according to the nonparametric Kolmogorov-Smirnov test. \*  $p < 0.1$ , \*\*  $p < 0.05$ , \*\*\*  $p < 0.01$ . (Data shown correspond to  $2 < n < 35$ . Each indentation test on an individual cell is represented by a point in the plot.)

case of deionized water-suspended cells, the higher osmotic pressure (see Table 2.4) causes higher stress on the cell walls [69]. In Figure 2.4 the initial effective stiffness values for the overall cell in each stage of differentiation are presented grouped by osmolarity of solution. Underneath each category is a graphical illustration of the morphology of the cells. The initial effective stiffness is measured from the first  $1\ \mu\text{m}$  of indentation data after contact. This depth of indentation ensures that we capture some contribution to the overall stiffness from turgor pressure and/or the cytoplasm, since the measured (hydrated) PCW and SCW thicknesses are both close to  $1\ \mu\text{m}$  [23]. See Figure 2.10 for an alternative grouping of the stiffness measurements by stage and osmolarity of solution.

## Hypertonic Condition

In hypertonic conditions, i.e., the sorbitol condition (Figure 2.4A), water flows out of the vacuole and across the cell membrane as the cell is plasmolyzed. The relief of turgor pressure allows for isolation of the mechanical response of the cell wall [25, 70]. So, in these conditions we model the stiffness response of the cell as a single spring which represents the cell wall(s). When uninduced cells (stage 0) are placed in hypertonic conditions, the measured stiffness ( $k_{\text{hyper,stage 0}} = 0.59 \pm 0.06$  N/m) corresponds to that of unstressed PCW.

$$k_{\text{hyper, stage 0}} = k_{\text{hyper,PCW}} \quad (2.2)$$

After DEX exposure, but before the formation of the SCW begins, we do not expect to see a difference in the stiffness of the PCW. Indeed, we do not detect any statistically significant difference in stiffness between stages 0 and 1 in hypertonic conditions ( $k_{\text{hyper,stage 1}} = 0.69 \pm 0.17$  N/m).

$$k_{\text{hyper, stage 1}} = k_{\text{hyper,PCW}} \quad (2.3)$$

In stage 2, the PCW is expanded and modified to allow space for the deposition of the SCW [64]. The coupled stiffness of the thin SCW bundles and the modified PCW interact in a way that produces a significant increase on the cellular effective stiffness ( $k_{\text{hyper,stage 2}} = 4.71 \pm 2.31$  N/m); this value is over five times the value observed in the prior stages, and more than double the addition of the isolated PCW stiffness and isolated SCW stiffness from stages 0 and 3. We propose two possible reasons for the observed increase in stiffness.

The presence of sorbitol may cause an increase of the cell wall stiffness through enhanced molecular interactions between the polysaccharide chains of the PCW and SCW. We hypothesize that in the presence of sorbitol, a polyalcohol with six hydroxyl groups per molecule, these side groups can interact with the available surface hydroxyl groups of the various polysaccharide chains (i.e., cellulose, hemicellulose, pectin) in the PCW and SCW. These polysaccharides are present on each cell wall in different amounts and configurations, and the interactions between them are a topic of active investigations [71]. The introduction of sorbitol may therefore contribute additional hydrogen bonding between the PCW and SCW, supporting our micro-indentation experimental observations.

Alternatively, the collapse of the cell in hypertonic conditions may cause buckling or folding of the PCW over the SCW bundles. Cell wall buckling or folding would result

in a higher amount of cell wall material being compressed under the indenter, thereby justifying more stiffness. This apparent stiffening in plasmolyzing conditions due to cell wall buckling has been suggested also for plant tissue indentations [25]. Again, this phenomenon would exist in all stages, but would be enhanced when the PCW is in contact with the spiral SCW. The gaps between the spiral SCW bundles provide channels in between which the PCW could fold, giving the overall cell wall material a thicker and more organized shape.

These two proposed mechanisms for stiffening are not mutually exclusive. The sorbitol may be interacting with cellulose in the PCW as it buckles to provide an even further increase in stiffness for the reorganized overall cell wall structure. In any case, the combined cell walls (CCWs) are the material which provides stiffness to the cell in the hypertonic condition.

$$k_{\text{hyper, stage 2}} = k_{\text{hyper, CCW}} \quad (2.4)$$

As PCD proceeds, all contents of the cytoplasm are lost and the PCW is at least partially hydrolyzed. At the end of transdifferentiation, the main remaining structural component of the xylem vessel element is a thickened SCW. In the final stage, in all solutions, we attribute all the measured stiffness to the thickened SCW ( $k_{\text{hyper, stage 3}} = 1.03 \pm 0.13 \text{ N/m}$ ).

$$k_{\text{hyper, stage 3}} = k_{\text{SCW}} \quad (2.5)$$

We measure a statistically significant higher stiffness in stage 3 when compared to stages 0 and 1 in hypertonic conditions. This result suggests that the fully developed SCW is stiffer than the PCW before and after induction. We also measure a statistically significant lower stiffness in stage 3 when compared to stage 2 in hypertonic conditions. The loss of the PCW as PCD proceeds eliminates the stiffening that was observed in stage 2, through either (or both) chemical and physical interactions explained in the paragraphs above.

### **Isotonic Condition**

In isotonic conditions (Figure 2.4B), the cells are growing, so the turgor pressure is above the osmotic pressure of the solution, but not as high as in the hypotonic condition discussed in the next section (see Table 2.4). In growth media the cells are turgid, the cytoplasm pushes against the cell wall, presenting a distinct morphological difference compared to the plasmolyzed cells which are shriveled and have a

retracted cytoplasm. As shown in literature, turgor pressure (from the vacuole and the cytoplasm) provides additional mechanical stiffness to the cell underneath the cell wall [23, 28, 72]. The vacuole and cytoplasm are represented by a new spring in our model connected in series to the cell wall(s). Before PCD is initiated, in stages 0 and 1, due to the presence of turgor pressure, we expect the stiffness of the PCW to be higher than in the same stages in hypertonic conditions because it is stressed ( $k_{\text{iso,PCW}} > k_{\text{hyper,PCW}}$ ).

In stage 0, before transdifferentiation is initiated, we observe the lowest stiffness among the cells tested in isotonic solution ( $k_{\text{iso,stage 0}} = 0.82 \pm 0.52$  N/m). From our spring model, the overall stiffness of the cell in isotonic conditions in stage 0 is

$$k_{\text{iso, stage 0}} = \frac{k_{\text{iso,PCW}}(k_{\text{n-b,iso}})}{k_{\text{iso,PCW}} + k_{\text{n-b,iso}}}. \quad (2.6)$$

There is no statistically significant difference between the effective stiffness of cells in stage 0 in hypertonic and isotonic conditions. For the effective spring constants in both of these models to be equivalent, the two springs in series in the isotonic model must be stiffer than the single spring in the hypertonic model (see plot in Figure 2.3). This implies that the PCW and the combined cytoplasm and vacuole in isotonic conditions must be stiffer than the PCW in hypertonic conditions. In other words, our model confirms that the PCW is stiffened through stress exerted from turgor pressure that exists in isotonic conditions.

Upon induction of transdifferentiation, the effective stiffness of the cells increases significantly. In stage 1, the model still contains 2 springs: one for the stressed PCW ( $k_{\text{iso,PCW}}$ ), and one for the bundled cytoplasm in isotonic conditions ( $k_{\text{b,iso}}$ ). The mean effective stiffness in stage 1 is  $k_{\text{iso,stage 1}} = 2.40 \pm 0.52$  N/m.

$$k_{\text{iso, stage 1}} = \frac{k_{\text{iso,PCW}}(k_{\text{b,iso}})}{k_{\text{iso,PCW}} + k_{\text{b,iso}}} \quad (2.7)$$

Assuming that there is no change in the PCW stiffness from stages 0 to 1, as observed in sorbitol (Figure 2.4A), our model indicates that the cytoplasmic contribution in stage 0 must be less than in stage 1 in isotonic conditions ( $k_{\text{n-b, iso}} < k_{\text{b, iso}}$ ).

As transdifferentiation proceeds to stage 2, a series of concurrent events influence the mechanical behavior of the cells: (i) the PCW is modified (loosened to allow for elongation for the SCW deposition and possibly entering the hydrolysis stage), (ii) the beginnings of SCW bundles are deposited, and (iii) the anisotropic fibrillar

cytoplasm starts detaching from the cell walls as the turgor pressure is reduced as a result of the cell entering the PCD stage upon differentiation [64]. The stiffness of the new CCW is represented in the spring model as  $k_{\text{iso, CCW}}$ , and the spring from the cytoplasm is removed, since the cytoplasm is no longer in contact with the cell wall. These mechanisms act together to determine the effective stiffness of the cell ( $k_{\text{iso, stage 2}} = 2.06 \pm 0.44 \text{ N/m}$ ). The reduced turgor pressure, loss of cytoplasmic contribution as the cell dies, and the PCW loosening reduce the effective stiffness of the system. The deposition of SCW increases the stiffness of the cell wall spring component, and therefore the overall system. According to our experiments, the cells have the same stiffness in stages 1 and 2. Thus, assuming that the cytoplasmic contribution is negligible at stage 2, the stressed PCW of stage 1 must be stiffer than the CCW of stage 2 ( $k_{\text{iso, CCW}} < k_{\text{iso, PCW}}$ ). This highlights the significant effects of turgor pressure stiffening the PCW in stages 0 and 1.

$$k_{\text{iso, stage 2}} = k_{\text{iso, CCW}} \quad (2.8)$$

At the last stage of differentiation when the SCW is fully developed and thickened, the measured effective stiffness ( $k_{\text{iso, stage 3}} = 1.78 \pm 0.97 \text{ N/m}$ ) is not statistically significant from the overall stiffnesses in stages 1 and 2. In order for cells in stage 3 to have the same overall stiffness as cells in stage 1, each component of the springs in series in stage 1 must be stiffer than the single spring in stage 3 ( $k_{\text{SCW}} < k_{\text{iso, PCW}}$ ). This highlights again the increased stiffness of a PCW under turgor pressure in stages 0 and 1.

$$k_{\text{iso, stage 3}} = k_{\text{SCW}} \quad (2.9)$$

### Hypotonic Condition

In water (Figure 2.4C), before the DEX induction, we measure the absolute stiffest cell response ( $k_{\text{hypo, stage 0}} = 7.37 \pm 1.58 \text{ N/m}$ ). This demonstrates that in hypotonic conditions, the high turgor pressure increases the stiffness of cytoplasm and the PCW. This is in agreement with the findings of Routier-Kierzkowska et al. and many others who have studied the effects of turgor pressure on cell and tissue mechanics [15, 27, 28, 73, 74].

$$k_{\text{hypo, stage 0}} = \frac{k_{\text{hypo, PCW}}(k_{\text{n-b, hypo}})}{k_{\text{hypo, PCW}} + k_{\text{n-b, hypo}}} \quad (2.10)$$

According to the two-spring model, this means that both the stiffness of the PCW and the cytoplasm in hypotonic conditions in stage 0 must be greater than any other directly measured stiffness.

As differentiation begins, the overall stiffness of the cell ( $k_{\text{hypo, stage 1}} = 1.89 \pm 0.48$  N/m) is drastically reduced.

$$k_{\text{hypo, stage 1}} = \frac{k_{\text{hypo}^*,\text{PCW}}(k_{\text{b,hypo}})}{k_{\text{hypo}^*,\text{PCW}} + k_{\text{b,hypo}}} \quad (2.11)$$

Assuming that there is no decrease in the cytoplasmic stiffness from stages 0 to 1, there must be lower stress in the PCW in stage 1, which we will denote  $k_{\text{hypo}^*,\text{PCW}}$ . We hypothesize that the stress exerted on the cell wall is reduced as the cell prepares for SCW deposition ( $k_{\text{hypo,PCW}} > k_{\text{hypo}^*,\text{PCW}}$ ). Loosening of the PCW to prepare for elongation prior to addition of PCW material has been previously reported, and here we propose that this same mechanism governs SCW deposition [51]. This loosening should be occurring in all osmotic conditions, but we propose that it is only distinguishable in hypotonic conditions because in these conditions the PCW is under the highest amount of stress since it is subjected to the highest turgor pressure. An alternative, or additional possible mechanism for this observed weakening is an early hydrolysis of the PCW. Both of these possibilities are supported by literature [64]. Our analysis could not distinguish the stiffness of the PCW in water stage 1 ( $k_{\text{hypo}^*,\text{PCW}}$ ) from the stiffness of the PCW in growth medium at the same stage ( $k_{\text{iso,PCW}}$ ).

As SCW is deposited, we measure that the effective stiffness at stage 2 is the lowest among all stages in hypotonic treatment ( $k_{\text{hypo, stage 2}} = 0.71 \pm 0.14$  N/m).

$$k_{\text{hypo, stage 2}} = k_{\text{hypo, CCW}} \quad (2.12)$$

As seen before, the balance between PCW modification (loosening/hydrolysis), early SCW deposition, and loss of turgor and cytoplasmic contribution determines the overall system stiffness. The effective stiffness of cells at stage 2 in hypotonic conditions is significantly lower than that of cells at stage 2 in isotonic and hypertonic conditions (see Figure 2.10). This difference in stiffness between water and other solutions in stage 2 supports the prior proposal that there is weakening of PCW due to early hydrolysis in water.

Finally, in the last stage, the measured stiffness ( $k_{\text{hypo, stage 3}} = 1.12 \pm 0.15$  N/m) corresponds solely to the fully developed SCW.

$$k_{\text{hypo, stage 3}} = k_{\text{SCW}} \quad (2.13)$$

Our results indicate that the combined CW stiffness of stage 2 is weaker than the mature SCW ( $k_{\text{hypo, CCW}} < k_{\text{SCW}}$ ). As expected, we measure that the thickened

SCW in any solution has the same stiffness, which shows that the properties of the fully developed SCW are not affected by the treatments. We have two cases of exceptionally high stiffness; uninduced cells in hypotonic conditions and plasmolyzed cells in stage 2 of transdifferentiation. Besides these two exceptional cases, the SCW alone is at least as stiff as any combined stiffnesses in any other case.

To summarize, the isolated CW stiffnesses can be ordered:

$$k_{PCW} < k_{SCW} < k_{iso,PCW}, k_{hypo^*,PCW} < k_{hypo,PCW}. \quad (2.14)$$

Again, we see that turgor pressure governs the overall mechanical response of the cell to compression through prestressing the PCW. We also confirm that the SCW bundles are stiffer than the PCW material without any prestress.

The CCW stiffnesses can be ordered as follows:

$$k_{hypo, CCW} < k_{iso, CCW} < k_{hyper, CCW} \quad (2.15)$$

The proposed molecular mechanisms governing the stiffness of the CCW are the hydrolysis of the PCW in water, and the stiffening of cellulose chains in the presence of sorbitol. Buckling or folding of the PCW in hypertonic conditions may also act to further stiffen the CCW response.

Finally, the stiffness representing the cytoplasm can be constrained with two inequalities:

$$k_{n-b, iso} < k_{b, iso} < k_{n-b, hypo} \quad (2.16)$$

$$k_{n-b, iso} < k_{b, hypo} \quad (2.17)$$

See Figure 2.11 for a visual representation of the magnitude of each stiffness component. Our assay allows us to directly assess, for the first time, the mechanical contributions of the cytoskeleton in the effective stiffness of intact plant cells, highlighting their important role in the mechanics of the system.

### **AFM Analysis of Differentiating VND7-Inducible Arabidopsis Cells**

AFM nano-indentation tests were conducted in water to evaluate cell wall indentation moduli in each stage of differentiation, as shown in Figure 2.5. We use a spherical bead with a 1  $\mu\text{m}$  diameter, which is able to capture the response of a rather large representative area of the PCW, considering the fact that cellulose fibrils are organized in bundles with 5–50 nm thickness [50]. The average indentation depth

for the force-controlled experiment is  $79.5 \pm 3.9$  nm (Mean  $\pm$  Standard Error), which is less than 10% of the average thickness of the hydrated PCW or SCW bundles. Therefore, the indentation depth is adequately shallow to assume that we can isolate the response of the cell wall, even though the cells are turgid [22–25]. Young's moduli measured from the PCW in stage 1 in hypotonic conditions ( $E_{\text{hypo, stage 1}} = 372 \pm 51$  kPa) is higher than in other stages of differentiation, which is in agreement with our micro-indentation results. The Young's moduli measured from the CCW in stage 2 ( $E_{\text{hypo, stage 2}} = 192 \pm 13$  kPa) is the lowest of the three stages, again confirming our measurements from the micro-indentation test. Finally, the Young's moduli measured in stage 3 ( $E_{\text{hypo, stage 3}} = 271 \pm 15$  kPa) has an intermediate stiffness, which further validates our micro-indentation results.

Measurements with AFM illustrate the extremely heterogeneous structure of the CW. In stage 1, where the PCW is the only CW of the system, the indentation modulus is measured in a range of 58.7 to 1840 kPa as shown in the histogram and map inset of Figure 2.5B. This large distribution arises from the heterogeneous, fibrillar structure of the PCW. The distribution of rigid cellulose fibrils in the compliant heterogeneous matrix of polysaccharides, proteins, and phenolic compounds is causing the local distribution of stiffness we observe with AFM. The high stress in the PCW in hypotonic solution leads to a high stress in the fibers of the PCW, which amplifies the observed heterogeneous stress distribution. In stage 2, the indentation modulus is measured in a range of 31.0 to 601 kPa (Figure 2.5C). The higher number of measurements with low moduli in stage 2 illustrates the degradation of the PCW, especially between SCW bundles, which was also suggested from the micro-compression tests. The overlay of line scan measurements on images of the cell reveals that we observe the higher moduli when testing over the combined early SCW bundles and PCW. In the example shown as an inset in Figure 2.5C, we see a modulus of approximately 600 kPa over the SCW bundle, and moduli around 300 kPa between the bundles. In stage 3, the indentation modulus is measured in a range of 5.6 to 676 kPa. The inset of Figure 2.5D shows a line scan over an area containing two SCW bundles. The line scan shows that the moduli on top of the bundles is as high as 700 kPa, and between the bundles they are about 150 kPa. The indentation moduli measured in stage 3 are more uniformly distributed between the minimum and maximum values than in stage 2. As the SCW bundles thicken, they become stiffer and eliminate the intermittent spaces, leading to fewer measurements over only degraded PCW.

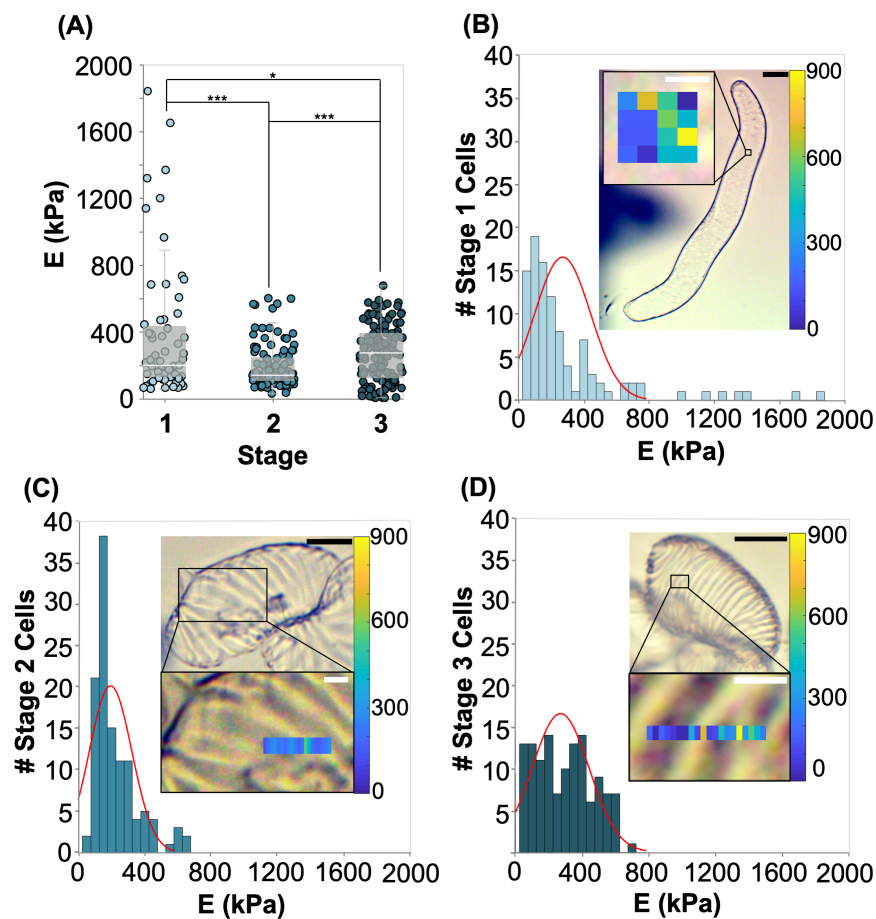


Figure 2.5: (A) Young's modulus for differentiating VND7-inducible Arabidopsis cells in each stage of differentiation measured with AFM. Stars indicate significant differences in distribution according to a Kolmogorov-Smirnov test. \*  $p < 0.1$ , \*\*\*  $p < 0.01$ . (Data shown correspond to  $n > 60$ . Each nano-indentation test is represented by a point in the plot. A minimum of 7 individual cells were tested in each stage.) (B) Histogram of Young's moduli measured in stage 1 of differentiation. Inset shows example location of measurement and map of stiffness in the area. (C) Histogram of Young's moduli measured in stage 2 of differentiation. Inset shows example location of measurement on cell and line map of stiffness in the area. (D) Histogram of Young's moduli measured in stage 3 of differentiation. Inset shows example location of measurement on cell and line map of stiffness in the area. Inset image scale bars are 20  $\mu\text{m}$  (black). Zoomed-in inset scale bars are 2  $\mu\text{m}$  (white).

## 2.3 Materials and Methods

### Cell Culture and Differentiation Induction

A suspension culture of transgenic *Arabidopsis thaliana* cells (VND7-inducible line, VND7-VP16-GR) was prepared from T87 cell line as described by [55]. The cells were maintained as callus form by the culture on solid agar medium, and transferred to new medium every three weeks. Parts of the callus of VND7-inducible cells were used to initiate a suspension culture, which was passaged weekly and was kept in flasks on a rotary shaker at 130 rpm at 23 °C. The VND7-inducible cell suspension was maintained in a modified Murashige and Skoog (MS) medium (Duchefa, Haarlem, the Netherlands) supplemented with 87 mM sucrose, 1nM 2,4-dichlorophenoxyacetic acid, 555 nM myo-inositol, 2 nm thiamin, 34 nM kanamycin, and 1.5 mM Potassium phosphate. To induce differentiation, dexamethasone (DEX) was introduced to the liquid media at a final concentration of 10 µM. Cells were collected post induction from the cultures at different time points, and their stages were classified from their morphological features as mentioned in Section 2.2. All chemicals and reactants were purchased from MilliporeSigma (St. Louis, MO, USA).

### Microscopy Observations

Cell walls were stained with 0.005% (w/v) calcofluor white and observed under a laser scanning confocal microscope (LSM880, Zeiss, Oberkochen, Germany). Cells were extracted from the culture, immersed in staining solution, and imaged without any other treatment. Z-stacks were acquired using a 40X water immersion objective (NA 1.2), and Imaris 9.5 (Bitplane, Zurich, Switzerland) was used for 3D rendering and bundle width determination. Specifically the Imaris Measurement Points module was used to quantify the bundles, and the surface module was used to reconstruct the PCW and SCW.

For light microscopy observations, which were performed to measure the dimensions of the cells, the cell walls of freshly extracted cells from culture were stained with 1 vol% solution of alcian blue in 3 vol% acetic acid, and observed with an AxioScope A1 (Zeiss, Oberkochen, Germany). Image analysis was carried out in ImageJ (<http://rsb.info.nih.gov/ij/>). From individual length measurements we report the statistical mean and standard error in the main part of the manuscript.

### Mechanical Testing

We tested the mechanical properties of the cells in three different osmotic conditions: in pure deionized water, in 1M sorbitol, and in growth media (composition mentioned above).

The micro-compression tests were performed using a FT-MTA02 system equipped with FT-S1000-LAT (liquid design) sensing probes with a  $50 \times 50 \mu\text{m}^2$  square tip (FemtoTools AG, Zurich, Switzerland) and an optical microscope. The obtained data of the indentations were position-corrected to account for contributions of the system's stiffness. Microscope glass slides (AmScope, Irvine, CA, USA) were cleaned with isopropyl alcohol, surface activated with a high frequency generator for 1 min (BD-20A, Electro-Technic Products, Chicago, IL, USA), and a thin layer of 0.5 mL of poly-l-lysine was spin coated on top of the slides (SUSS MicroTec, Garching, Germany). Cells were extracted from culture and pipetted on the coated glass slides. The cells were washed several times with the selected treatment solution to effectively decluster them and keep only the ones that adhered better to the substrate. For testing, 1–3 mL of the selected solution were added on top of the washed and diluted cells, and force-controlled indentations to 900  $\mu\text{N}$  were conducted by immersing the sensing probe in liquid. The corresponding average indentation depth was  $29.2 \pm 0.93 \mu\text{m}$  (Mean  $\pm$  Standard Error), which is close to the average width of the cell reported in Table 2.2 because we compress most cells to failure. In the plots on Figure 2.4, each point corresponds to the compression of an individual cell. Representative force indentation curves of cells in stage 0 in all tested osmotic conditions are presented in Figure 2.12A.

Short-range nano-indentations to evaluate the properties of the cell wall were conducted with AFM (Asylum Research, MFP-3D-Bio, Goleta, CA, USA). For the indentations, we used custom tips with a silicon dioxide spherical particle (diameter 1  $\mu\text{m}$ ) on a silicon nitride (SN) cantilever with a stiffness of  $0.63 \pm 0.03 \text{ N/m}$  (Mean  $\pm$  Standard Error) and a virtual deflection of  $14.9 \pm 4.5 \text{ mV}/\mu\text{m}$  (Mean  $\pm$  Standard Error) (Novascan, Boone, IA, USA). The AFM indentations were conducted in deionized water, in glass slides treated as mentioned before for the micro-compression tests. For every tested glass slide, the system was allowed to reach thermal equilibrium for 2–3 h. We conducted force-controlled indentations to 3nN and applied the Hertz model (Equation 1.5) to calculate the indentation modulus,  $E$ . Each point in Figure 2.5A corresponds to an indentation test. We conducted multiple indentations for a given cell, and tested a minimum of 7 cells in each stage. A representative

force indentation curve in which the indentation part has been fitted with a Hertz model is presented in Figure 2.12B.

### Analysis

Most of the data processing for the micro-compression tests follows that of Routier-Kierzkowska et al. [15]. First, to account for the compliance of the sensor, a reference measurement is obtained by compressing an area of the glass slide with no cells present for 1–2  $\mu\text{m}$ . The linear indentation part of data are linearly fitted. The sensor stiffness ( $S$ ) is typically above 200 N/m. All data sets are then transformed by

$$\delta_{\text{corrected}} = \delta - \frac{F}{S} \quad (2.18)$$

where  $\delta_{\text{corrected}}$  is the corrected displacement,  $\delta$  is the measured displacement,  $F$  is the measured force, and  $S$  is the sensor stiffness determined by calibration.

Next, we offset the measured force-displacement data so that the average force up until the contact point is zero. The contact point is defined as the point where the force exceeds a user-defined threshold. The force thresholding and offsetting are repeated using increasingly sensitive force thresholds. The final selected threshold value is typically less than 1  $\mu\text{m}$ . Then, a Savitsky-Golay moving-window data filter is applied to smooth the data. The window size is 25 data points which are fit to a 2nd order polynomial.

Finally, the first 1  $\mu\text{m}$  of indentation data after the located contact point is linearly fitted. The interpolated slope is taken as the overall stiffness of the cell. The overall stiffnesses of cells are compared between stages of transdifferentiation and between osmolarities of testing solutions. A Kolmogorov-Smirnov statistical test is performed, which compares the empirical cumulative distribution functions of each grouping.

The data processing for AFM nano-indentations was executed by Asylum Research software (AR 16.10.211) in Igor Pro 6.3. The software was used to identify the contact point and extract a Young's modulus through the application of the Hertz model.

All data processing was performed using the Python programming language (Python Software Foundation, <https://www.python.org/>). All statistical visualizations were created using Altair [75].

## 2.4 Conclusions

We designed a multi-scale biomechanical assay to experimentally isolate the mechanical contributions from the cytoplasm and cell wall during the differentiation of transgenic Arabidopsis cells to protoxylem vessel elements. The mechanical data at different scales and in different osmotic conditions in combination with the proposed two-spring model allow us to decouple the contributions from each structural element of the cell as it responds to changes in turgor pressure at various stages of the differentiation process. At the micro-scale, we performed indentations that covered most of the cell area and measured the overall stiffness from the first 1  $\mu\text{m}$  of indentation data, ensuring that we probe stiffness contributions from the cell wall and cytoplasm, which we represent as two springs in series in our proposed spring model. The resulting deconvoluted stiffnesses from the cell wall(s) and cytoplasm are dependent on the validity of the assumptions required to implement the spring model, which includes neglecting any nonlinear mechanical effects, like adhesion, viscosity or plasticity. At the nano-scale, we performed AFM indentations that covered a smaller area of the cell wall, and indented a few tens of nanometers, to isolate the mechanical behavior of the cell wall. Our analysis provides experimental evidence that the SCW is stiffer than the relaxed PCW in a living cell system. This conclusion is reached by comparing measured cell stiffnesses in hypertonic conditions, where the cell wall is effectively decoupled from the cytoplasm. In isotonic and hypotonic conditions, turgor pressure gives rise to an increased stress in PCW, causing it to stiffen beyond the SCW. We also measure a quantifiable loosening of the PCW in stage 1 in hypotonic conditions, as the cell prepares for deposition of the SCW. This is the first time a mechanical weakening is measured on the PCW before the SCW deposition in living cells. From measurements in isotonic and hypotonic conditions, we also find evidence of a quantifiable difference in cytoplasmic stiffness as a consequence of active bundling of the filaments in the cytoplasm, guided by differentiation.

These findings provide insight into the mechanisms of xylem vessel element differentiation. They suggest that inter- and/or intra-cellular mechanical signals regulate cell differentiation and SCW deposition.

## Acknowledgements

This work was supported in part by the Resnick Sustainability Institute at Caltech (C.D.) and by the MEXT KAKENHI Grant Numbers JP18H05484 and JP18H05489

(M.O. and T.D.). We would like to acknowledge the contributions of Jenny Martinez, who conducted part of the micro-indentations in water, and Luca Bonanomi for helpful discussions.

## **Appendix**

The mean principal dimensions and standard errors for each cell shape (rounded and elongated) are reported in Table 2.2. The confocal analysis reveals that in stage 1, the PCW thickness of rounded and elongated cells is the same, measured at  $580 \pm 10$  nm (Mean  $\pm$  Standard Error) in both cases. The population of rounded cells that have transitioned into stage 2 and have deposited SCW bundles have on average a total cell volume 72% higher than rounded cells at stage 1. Cells that are found to be in stage 3, with fully developed SCW and ruptured tonoplast, have on average an insignificantly changed total volume, compared to cells at stage 2. Our observations indicate a different trend in elongated cells. In that case, the volume of cells in stages 1 and 2 is almost the same. Between elongated cells in stages 2 and 3, we notice that cells at the last stage of differentiation are about 35% on average larger in volume. The higher volume of cells in stage 3 reflects larger dimensions in both the lateral (11% average increase in width) and longitudinal directions (9% average increase in length). Comparing the volumes of the two shapes, elongated cells are approximately 69% larger than rounded cells in stage 1. In stage 2, elongated and rounded cells have similar volumes. Finally, in stage 3, elongated cells have 22% more volume than rounded cells on average. Apparently, rounded cells are able to enlarge more significantly than elongated cells just prior to SCW deposition.

In Table 2.3 we present the thickness and areal densities of SCW bundles in rounded and elongated cells. We measure that the elongated and rounded cells have similar bundle densities and thicknesses in stage 2. We observe that the SCW thickening during the last stage of differentiation leads to the same bundle thickness in both elongated and rounded cells. In both cases the SCW thickens by approximately 40%, as presented in Table 2.3. The bundle density does not change significantly between stages 2 and 3 for either elongated or rounded cells. The measured bundle density is about 7% higher for elongated cells than for rounded cells. We propose that this is a result of the inherent structural requirement of elongated vessels to be able to support higher stresses in their walls than spherical vessels when experiencing the same amount of pressure.

The relationship between turgor pressure and osmolarity is described by the follow-

Table 2.2: Principal dimensions of elongated and round-shaped cells. Length, width, and diameter were measured from light microscopy images. Volumes were calculated using formula for a cylinder for elongated cells and a sphere for round cells. The data shown correspond to Mean  $\pm$  Standard Error (SE) ( $n > 20$ ).

Cell Shape & Stage	Dimension	Mean $\pm$ SE
Elongated Stage 1	Length ( $\mu\text{m}$ )	60.4 $\pm$ 2.4
Elongated Stage 2	Length ( $\mu\text{m}$ )	56.4 $\pm$ 4.9
Elongated Stage 3	Length ( $\mu\text{m}$ )	61.6 $\pm$ 3.7
Elongated Stage 1	Width ( $\mu\text{m}$ )	30.7 $\pm$ 1.0
Elongated Stage 2	Width ( $\mu\text{m}$ )	31.2 $\pm$ 2.8
Elongated Stage 3	Width ( $\mu\text{m}$ )	34.7 $\pm$ 1.6
Round Stage 1	Diameter ( $\mu\text{m}$ )	37.0 $\pm$ 0.9
Round Stage 2	Diameter ( $\mu\text{m}$ )	44.2 $\pm$ 2.1
Round Stage 3	Diameter ( $\mu\text{m}$ )	45.0 $\pm$ 2.0
Elongated Stage 1	Volume ( $\mu\text{m}^3$ )	44,700 $\pm$ 2100
Elongated Stage 2	Volume ( $\mu\text{m}^3$ )	43,100 $\pm$ 5300
Elongated Stage 3	Volume ( $\mu\text{m}^3$ )	58,300 $\pm$ 4100
Round Stage 1	Volume ( $\mu\text{m}^3$ )	26,500 $\pm$ 1000
Round Stage 2	Volume ( $\mu\text{m}^3$ )	45,500 $\pm$ 3300
Round Stage 3	Volume ( $\mu\text{m}^3$ )	47,700 $\pm$ 3400

Table 2.3: SCW bundle feature sizes for rounded and elongated VND7-inducible cells. Bundle densities were measured from optical microscopy images. Bundle thicknesses were measured from confocal three-dimensional reconstructions. The data shown correspond to Mean  $\pm$  Standard Error (SE) ( $n > 45$ ).

Cell Shape & Stage	Dimension ( $\mu\text{m}$ )	Mean $\pm$ SE
Elongated Stage 2	bundle density ( $\#/\mu\text{m}^2$ )	0.056 $\pm$ 0.005
Elongated Stage 3	bundle density ( $\#/\mu\text{m}^2$ )	0.060 $\pm$ 0.004
Round Stage 2	bundle density ( $\#/\mu\text{m}^2$ )	0.051 $\pm$ 0.005
Round Stage 3	bundle density ( $\#/\mu\text{m}^2$ )	0.050 $\pm$ 0.008
Elongated Stage 2	bundle thickness ( $\mu\text{m}$ )	1.05 $\pm$ 0.01
Elongated Stage 3	bundle thickness ( $\mu\text{m}$ )	1.45 $\pm$ 0.01
Round Stage 2	bundle thickness ( $\mu\text{m}$ )	1.09 $\pm$ 0.04
Round Stage 3	bundle thickness ( $\mu\text{m}$ )	1.52 $\pm$ 0.03

Table 2.4: Osmotic pressure calculated for each of the three solutions used for mechanical testing.

Solution	$P$ (MPa)
water	137.5
T87 Growth Medium	11.4
sorbitol	2.5

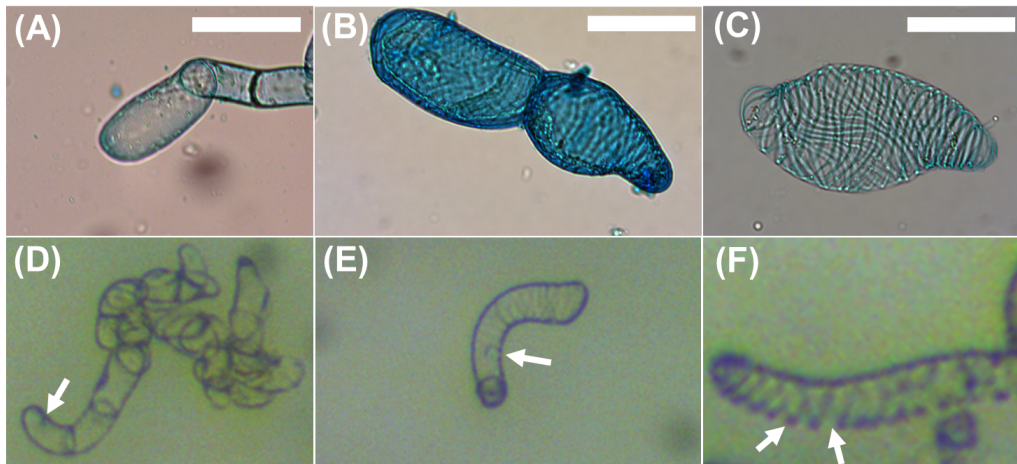


Figure 2.6: (A–C) Optical microscopy images and (D–F) images from the micro-mechanical testing device to demonstrate cell classification process. (A,D) Living cells in stage 1 of transdifferentiation (only PCW observed, arrow points to cell nucleus). (B,E) Living cells in stage 2 of transdifferentiation (PCW and SCW are both present, cytoplasm is still inside the cell, arrow points to cell nucleus); (C,F) Living cells in stage 3 of transdifferentiation (SCW and partially perforated PCW, cytoplasmic contents almost entirely removed, arrow points to locations where PCW is degraded). All scale bars are 20  $\mu\text{m}$ .

ing equation

$$P = MiRT \quad (2.19)$$

where  $P$  is the osmotic pressure,  $M$  is the molarity of the solution,  $i$  is the Van't Hoff factor which represents the number of distinct particles produced when the substance is dissolved,  $R$  is the universal gas constant, and  $T$  is temperature [69].

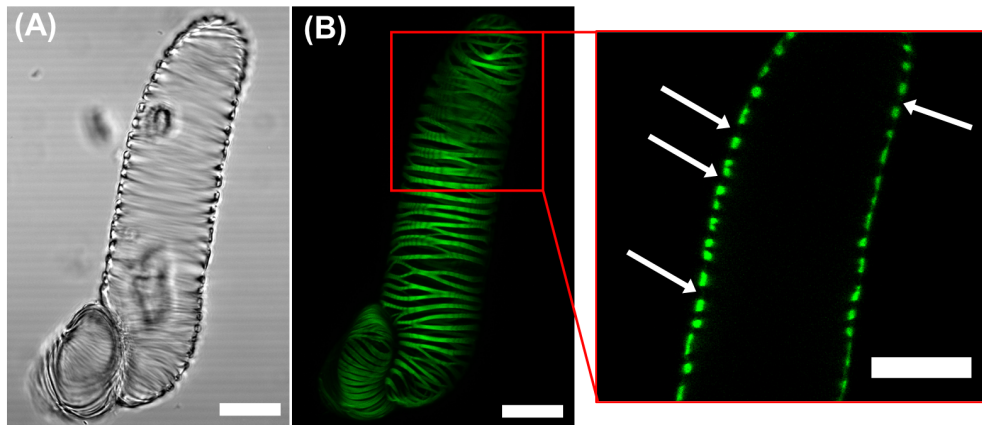


Figure 2.7: Transmitted and fluorescent images of an elongated VND7-inducible cell in stage 3 of transdifferentiation with visible hydrolyzed PCW. (A) Transmitted light image of the cell showing loss of most cytoplasmic contents. (B) Fluorescent image of cell highlighting location of SCW bundles. (inset) Single slice of fluorescent confocal image with arrows pointing to gaps in the cell wall, showing that we indeed have loss of PCW material in some locations. All scale bars 20  $\mu\text{m}$ .

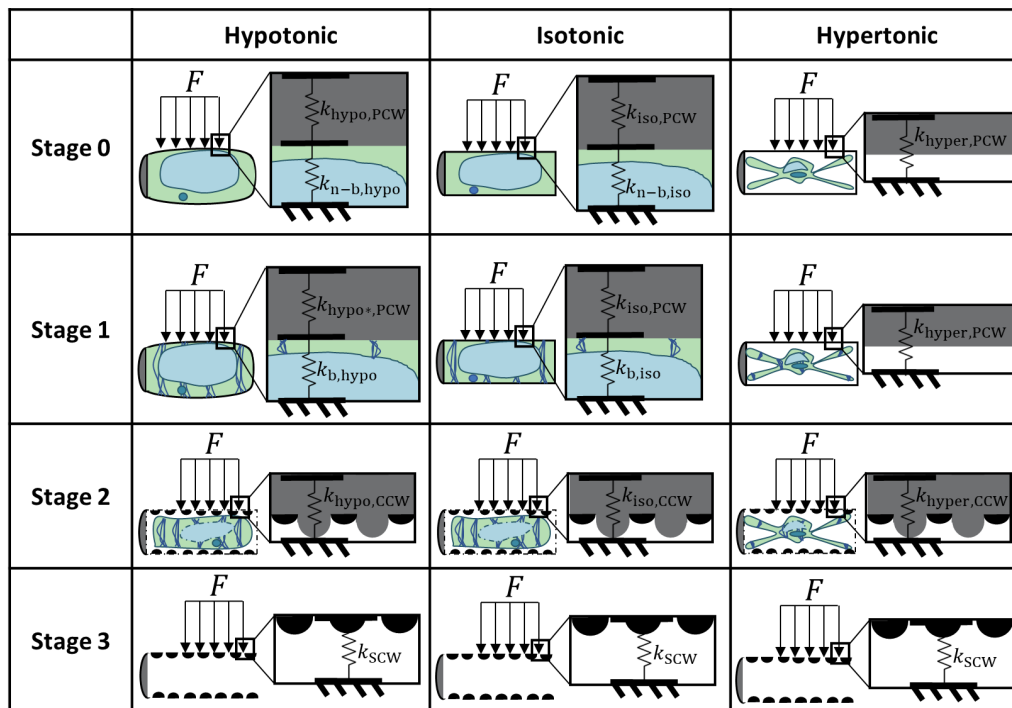


Figure 2.8: Spring models for all treatments/stages.

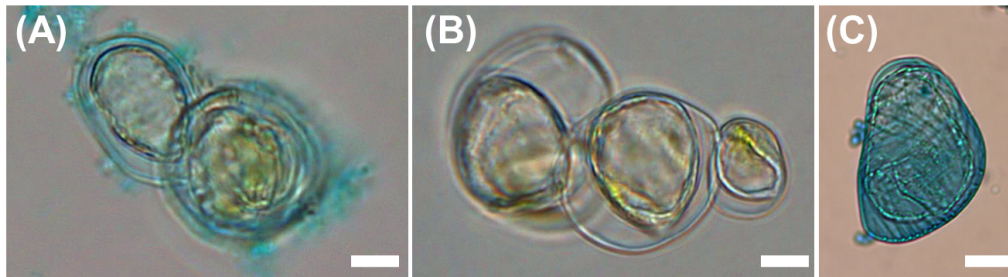


Figure 2.9: Transmitted light images of VND7-inducible cells immersed in sorbitol solution for 1 min visualizing the immediate effects of plasmolyzing conditions. Cytoplasm retraction upon plasmolysis is observed for cells at (A) stage 0, (B) stage 1, (C) stage 2. All scale bars 20  $\mu\text{m}$ .

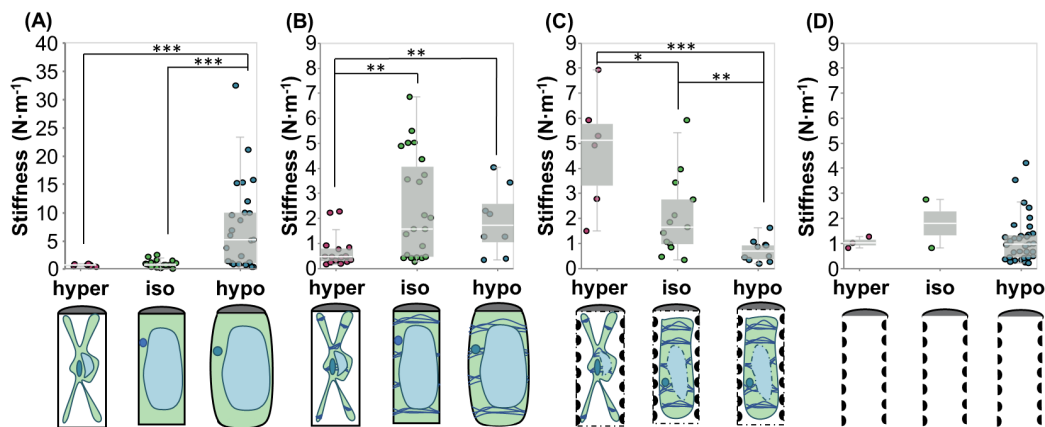


Figure 2.10: Panel showing stiffness in hypertonic, isotonic, and hypotonic solutions in 4 stages of transdifferentiation: (A) stage 0; (B) stage 1; (C) stage 2; (D) stage 3. Stars indicate significant differences in distribution according to a Kolmogorov-Smirnov test. \*  $p < 0.1$ , \*\*  $p < 0.05$ , \*\*\*  $p < 0.01$ .

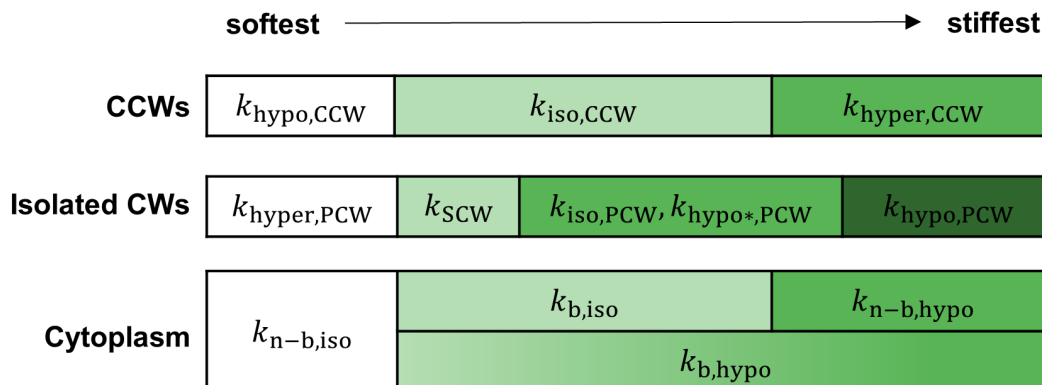


Figure 2.11: Stiffness comparison for each component of spring models.

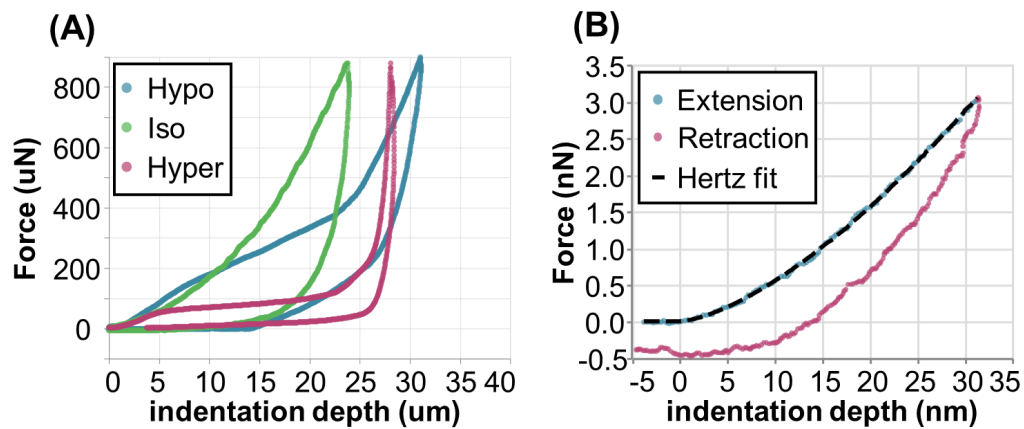


Figure 2.12: Example force-indentation data for (A) micro-compression experiment on three different cells in each of the three osmotic treatments: hypotonic, isotonic, and hypertonic; and (B) AFM experiment with extension (blue line) and retraction (pink line) data with Hertz fit (dash line) overlay.

## References

- [3] Daniel J. Cosgrove. “Assembly and enlargement of the primary cell wall in plants”. In: *Annual Review of Cell and Developmental Biology* 13.1 (1997). PMID: 9442872, pp. 171–201. DOI: 10.1146/annurev.cellbio.13.1.171. eprint: <https://doi.org/10.1146/annurev.cellbio.13.1.171>. URL: <https://doi.org/10.1146/annurev.cellbio.13.1.171>.
- [15] Anne-Lise Routier-Kierzkowska et al. “Cellular Force Microscopy for in Vivo Measurements of Plant Tissue Mechanics”. In: *Plant Physiology* 158.4 (2012), pp. 1514–1522. ISSN: 0032-0889. DOI: 10.1104/pp.111.191460. eprint: <http://www.plantphysiol.org/content/158/4/1514.full.pdf>. URL: <http://www.plantphysiol.org/content/158/4/1514>.
- [22] Ksenija Radotić et al. “Atomic force microscopy stiffness tomography on living *Arabidopsis thaliana* cells reveals the mechanical properties of surface and deep cell-wall layers during growth”. eng. In: *Biophysical Journal* 103.3 (Aug. 2012), pp. 386–394. ISSN: 1542-0086. DOI: 10.1016/j.bpj.2012.06.046.
- [23] Pascale Milani, Siobhan A. Braybrook, and Arezki Boudaoud. “Shrinking the hammer: micromechanical approaches to morphogenesis”. In: *Journal of Experimental Botany* 64.15 (July 2013), pp. 4651–4662. ISSN: 0022-0957. DOI: 10.1093/jxb/ert169. eprint: <https://academic.oup.com/jxb/article-pdf/64/15/4651/18043081/ert169.pdf>. URL: <https://doi.org/10.1093/jxb/ert169>.
- [24] Arun Sampathkumar et al. “Subcellular and supracellular mechanical stress prescribes cytoskeleton behavior in *Arabidopsis* cotyledon pavement cells”. In: *eLife* 3 (Apr. 2014). Ed. by Dominique Bergmann, e01967. ISSN: 2050-084X. DOI: 10.7554/eLife.01967. URL: <https://doi.org/10.7554/eLife.01967>.
- [25] Siobhan A. Braybrook. “Chapter 13 - Measuring the elasticity of plant cells with atomic force microscopy”. In: *Biophysical Methods in Cell Biology*. Ed. by Ewa K. Paluch. Vol. 125. Methods in Cell Biology. Academic Press, 2015, pp. 237–254. DOI: <https://doi.org/10.1016/bs.mcb.2014.10.006>. URL: <http://www.sciencedirect.com/science/article/pii/S0091679X14000077>.
- [27] Léna Beauzamy, Julien Derr, and Arezki Boudaoud. “Quantifying hydrostatic pressure in plant cells by using indentation with an atomic force microscope”. In: *Biophysical journal* 108.10 (2015), pp. 2448–2456.
- [28] Alain Weber et al. “Measuring the mechanical properties of plant cells by combining micro-indentation with osmotic treatments”. In: *Journal of Experimental Botany* 66.11 (Apr. 2015), pp. 3229–3241. ISSN: 0022-0957. DOI: 10.1093/jxb/erv135. eprint: <https://academic.oup.com/>

- jxb/article-pdf/66/11/3229/17137090/erv135.pdf. URL: <https://doi.org/10.1093/jxb/erv135>.
- [48] Lorna J Gibson. “The hierarchical structure and mechanics of plant materials”. In: *Journal of the royal society interface* 9.76 (2012), pp. 2749–2766.
- [49] Ruiqin Zhong, Dongtao Cui, and Zheng-Hua Ye. “Secondary cell wall biosynthesis”. In: *New Phytologist* 221.4 (2019), pp. 1703–1723. DOI: 10.1111/nph.15537. eprint: <https://nph.onlinelibrary.wiley.com/doi/pdf/10.1111/nph.15537>. URL: <https://nph.onlinelibrary.wiley.com/doi/abs/10.1111/nph.15537>.
- [50] Robert J. Moon et al. “Cellulose nanomaterials review: structure, properties and nanocomposites”. In: *Chem. Soc. Rev.* 40 (7 2011), pp. 3941–3994. DOI: 10.1039/C0CS00108B. URL: <http://dx.doi.org/10.1039/C0CS00108B>.
- [51] Daniel J. Cosgrove. “Plant cell wall extensibility: connecting plant cell growth with cell wall structure, mechanics, and the action of wall-modifying enzymes”. In: *Journal of Experimental Botany* 67.2 (Nov. 2015), pp. 463–476. ISSN: 0022-0957. DOI: 10.1093/jxb/erv511. eprint: <https://academic.oup.com/jxb/article-pdf/67/2/463/9366332/erv511.pdf>. URL: <https://doi.org/10.1093/jxb/erv511>.
- [52] Ovijit Chaudhuri, Sapun H. Parekh, and Daniel A. Fletcher. “Reversible stress softening of actin networks”. In: *Nature* 445.7125 (2007), pp. 295–298. ISSN: 1476-4687. DOI: 10.1038/nature05459. URL: <https://doi.org/10.1038/nature05459>.
- [53] F Gittes et al. “Flexural rigidity of microtubules and actin filaments measured from thermal fluctuations in shape.” In: *Journal of Cell Biology* 120.4 (Feb. 1993), pp. 923–934. ISSN: 0021-9525. DOI: 10.1083/jcb.120.4.923. eprint: <https://rupress.org/jcb/article-pdf/120/4/923/384296/923.pdf>. URL: <https://doi.org/10.1083/jcb.120.4.923>.
- [54] Pauline Durand-Smet et al. “A Comparative Mechanical Analysis of Plant and Animal Cells Reveals Convergence across Kingdoms”. In: *Biophysical Journal* 107.10 (2014), pp. 2237–2244. ISSN: 0006-3495. DOI: <https://doi.org/10.1016/j.bpj.2014.10.023>. URL: <http://www.sciencedirect.com/science/article/pii/S0006349514010741>.
- [55] Masatoshi Yamaguchi et al. “VASCULAR-RELATED NAC-DOMAIN6 and VASCULAR-RELATED NAC-DOMAIN7 Effectively Induce Transdifferentiation into Xylem Vessel Elements under Control of an Induction System”. en. In: *Plant Physiology* 153.3 (July 2010). Publisher: American Society of Plant Biologists Section: BREAKTHROUGH TECHNOLOGIES, pp. 906–914. ISSN: 0032-0889, 1532-2548. DOI: 10.1104/pp.110.154013.

URL: <http://www.plantphysiol.org/content/153/3/906> (visited on 07/31/2020).

- [56] Minoru Kubo et al. “Transcription switches for protoxylem and metaxylem vessel formation”. In: *Genes & Development* 19.16 (2005), pp. 1855–1860. DOI: 10.1101/gad.1331305. eprint: <http://genesdev.cshlp.org/content/19/16/1855.full.pdf+html>.
- [57] Sacha Escamez and Hannele Tuominen. “Programmes of cell death and autolysis in tracheary elements: when a suicidal cell arranges its own corpse removal”. en. In: *Journal of Experimental Botany* 65.5 (Mar. 2014). Publisher: Oxford Academic, pp. 1313–1321. ISSN: 0022-0957. DOI: 10.1093/jxb/eru057. URL: <https://academic.oup.com/jxb/article/65/5/1313/452788> (visited on 07/31/2020).
- [58] Hiroo Fukuda. “Tracheary Element Differentiation.” In: *The Plant Cell* 9.7 (July 1997), pp. 1147–1156. ISSN: 1040-4651. URL: <https://www.ncbi.nlm.nih.gov/pmc/articles/PMC156987/> (visited on 08/01/2020).
- [59] Elena T Iakimova and Ernst J Woltering. “Xylogenesis in zinnia (*Zinnia elegans*) cell cultures: unravelling the regulatory steps in a complex developmental programmed cell death event”. In: *Planta* 245.4 (2017), pp. 681–705.
- [60] Anna Kákošová et al. “Galactoglucomannan oligosaccharides are assumed to affect tracheary element formation via interaction with auxin in *Zinnia* xylogenic cell culture”. In: *Plant cell reports* 32.4 (2013), pp. 479–487.
- [61] Hannes Vogler et al. “Measuring the Mechanical Properties of Plant Cell Walls”. In: *Plants* 4.2 (2015), pp. 167–182. ISSN: 2223-7747. DOI: 10.3390/plants4020167. URL: <https://www.mdpi.com/2223-7747/4/2/167>.
- [62] Zengfang Yin and Ruwen Fan. “Ultrastructural analysis of the differentiation process of secondary xylem vessel element in *Populus deltoides*”. en. In: *Frontiers of Forestry in China* 4.484 (July 2009). Publisher: Springer. ISSN: 1673-3630. DOI: 10.1007/s11461-009-0067-6. URL: <https://link.springer.com/article/10.1007%5C%2Fs11461-009-0067-6> (visited on 08/30/2020).
- [63] Miranda J Meents, Yoichiro Watanabe, and A Lacey Samuels. “The cell biology of secondary cell wall biosynthesis”. In: *Annals of Botany* 121.6 (Feb. 2018), pp. 1107–1125. ISSN: 0305-7364. DOI: 10.1093/aob/mcy005. eprint: <https://academic.oup.com/aob/article-pdf/121/6/1107/24805712/mcy005.pdf>. URL: <https://doi.org/10.1093/aob/mcy005>.
- [64] Benjamin Bollhöner, Jakob Prestele, and Hannele Tuominen. “Xylem cell death: emerging understanding of regulation and function”. en. In: *Journal of Experimental Botany* 63.3 (Feb. 2012). Publisher: Oxford Academic, pp. 1081–1094. ISSN: 0022-0957. DOI: 10.1093/jxb/err438. URL: <https://doi.org/10.1093/jxb/err438>.

- [://academic.oup.com/jxb/article/63/3/1081/475758](https://academic.oup.com/jxb/article/63/3/1081/475758) (visited on 08/01/2020).
- [65] Yoshihisa Oda and Seiichiro Hasezawa. “Cytoskeletal organization during xylem cell differentiation”. en. In: *Journal of Plant Research* 119.3 (May 2006), pp. 167–177. ISSN: 1618-0860. DOI: 10.1007/s10265-006-0260-8. URL: <https://doi.org/10.1007/s10265-006-0260-8> (visited on 08/03/2020).
- [66] Takema Sasaki, Hiroo Fukuda, and Yoshihisa Oda. “CORTICAL MICROTUBULE DISORDERING1 Is Required for Secondary Cell Wall Patterning in Xylem Vessels”. In: *The Plant Cell* 29.12 (2017), pp. 3123–3139. ISSN: 1040-4651. DOI: 10.1105/tpc.17.00663. eprint: <http://www.plantcell.org/content/29/12/3123.full.pdf>. URL: <http://www.plantcell.org/content/29/12/3123>.
- [67] Rene Schneider et al. “Two Complementary Mechanisms Underpin Cell Wall Patterning during Xylem Vessel Development”. In: *The Plant Cell* 29.10 (2017), pp. 2433–2449. ISSN: 1040-4651. DOI: 10.1105/tpc.17.00309. eprint: <http://www.plantcell.org/content/29/10/2433.full.pdf>. URL: <http://www.plantcell.org/content/29/10/2433>.
- [68] Joseph Boussinesq. “Application des potentials al’etude de l’equilibre et des mouvements des solides elastiques”. In: *Paris, Ganther-Villars* (1885).
- [69] Léna Beauzamy, Naomi Nakayama, and Arezki Boudaoud. “Flowers under pressure: ins and outs of turgor regulation in development”. In: *Annals of botany* 114.7 (2014), pp. 1517–1533.
- [70] Amir J Bidhendi and Anja Geitmann. “Methods to quantify primary plant cell wall mechanics”. In: *Journal of Experimental Botany* 70.14 (July 2019), pp. 3615–3648. ISSN: 0022-0957. DOI: 10.1093/jxb/erz281. eprint: <https://academic.oup.com/jxb/article-pdf/70/14/3615/28985115/erz281.pdf>. URL: <https://doi.org/10.1093/jxb/erz281>.
- [71] Y. Watanabe et al. “Visualization of cellulose synthases in Arabidopsis secondary cell walls”. en. In: *Science* 350.6257 (Oct. 2015). Publisher: American Association for the Advancement of Science Section: Report, pp. 198–203. ISSN: 0036-8075, 1095-9203. DOI: 10.1126/science.aac7446. URL: <https://science.sciencemag.org/content/350/6257/198> (visited on 08/03/2020).
- [72] Pascale Milani et al. “In vivo analysis of local wall stiffness at the shoot apical meristem in Arabidopsis using atomic force microscopy”. In: *The Plant Journal* 67.6 (2011), pp. 1116–1123. DOI: <https://doi.org/10.1111/j.1365-313X.2011.04649.x>. eprint: <https://onlinelibrary.wiley.com/doi/pdf/10.1111/j.1365-313X.2011.04649.x>. URL:

<https://onlinelibrary.wiley.com/doi/abs/10.1111/j.1365-313X.2011.04649.x>.

- [73] Olivier Hamant and Elizabeth S. Haswell. “Life behind the wall: sensing mechanical cues in plants”. en. In: *BMC Biology* 15.1 (Dec. 2017), p. 59. ISSN: 1741-7007. DOI: 10.1186/s12915-017-0403-5. URL: <http://bmcbiol.biomedcentral.com/articles/10.1186/s12915-017-0403-5> (visited on 09/19/2020).
- [74] P Durand-Smet et al. “Estimation of turgor pressure through comparison between single plant cell and pressurized shell mechanics”. In: *Physical Biology* 14.5 (2017), p. 055002.
- [75] Jacob VanderPlas et al. “Altair: Interactive Statistical Visualizations for Python”. In: *Journal of Open Source Software* (Dec. 2018). DOI: 10.21105/joss.01057. URL: <https://doi.org/10.21105/joss.01057>.

*Chapter 3***CELL WALL AND CYTOSKELETAL CONTRIBUTIONS IN SINGLE-CELL BIOMECHANICS OF *NICOTIANA TABACUM***

This chapter is adapted from:

- [1] Leah Ginsberg et al. “Cell wall and cytoskeletal contributions in single cell biomechanics of *Nicotiana tabacum*”. In: *Plant and Cell Physiology* (In review).

**Abstract**

We study the mechanical response of individual *Nicotiana tabacum* cells from a suspension culture and evaluate the mechanical contributions of the cell wall (CW), cytoplasm, and the underlying cytoskeleton. To separate the stiffness contributions, we design a multiscale biomechanical assay. We further elucidate the influence of turgor pressure by testing cells in different osmotic conditions. The role played by the microtubules (MTs) and actin filaments (AFs) is deconvoluted through the use of drug treatments which selectively remove MTs and AFs. The stiffness of the CW is isolated by shallow indentations with an atomic-force microscope (AFM), while bulk cell behavior is probed through micro-indentations. Cell stiffness and total dissipated energy are calculated from micro-indentations. To decouple the contribution of the CW and cytoplasm to the relative stiffness, and in particular that of the MTs and AFs, we propose a generative statistical model of the cell. We idealize the cell as two springs acting in series and use the experimentally determined initial stiffnesses as input to the model to determine the relative stiffness contributions of the CW, cytoplasm, turgor pressure, MTs, and AFs. Analysis of the initial stiffness and energy dissipation calculated from micro-indentation tests indicates that the cytoskeleton contributes significantly to the mechanical response of a cell under compression. Micro and nano-indentation tests confirm that turgor pressure is the most significant contributor to the stiffness response of turgid cells in compression. Finally, our results reveal that turgor pressure exerts stress on the CW, which leads to a measurable CW stiffening.

**Keywords:** Cell wall; cytoskeleton; micro-indentation; nano-indentation; *Nicotiana tabacum*; statistical modeling

### 3.1 Introduction

To further our knowledge of the structure and mechanics of plant-based materials, the investigation of their building blocks, the individual plant cells, is crucial. The structure of a plant cell is comprised of two key components: the cell wall (CW) and the cytoplasm, which contains the vacuole, cytoskeleton, cytosol, nucleus, and other organelles. Cellulose, the load-bearing component of the CW, plays a central role in the structure and mechanics of the CW. Pure cellulose has been reported to have a Young's modulus ( $E = 110 - 220$  GPa) comparable to that of carbon fiber or steel [50]. The stiffness of the CW allows the cell to survive in environments with high osmolarity by holding enormous turgor pressures ( $p = 0.3 - 1.0$  MPa) in the vacuole without rupturing the cell [3]. The cytoskeleton is made of filamentous proteins, including microtubules (MTs) and actin filaments (AFs). Recent work suggests that, beyond their functional roles, the MTs and AFs in the cytoskeleton can play a significant role in the ability of a cell to resist mechanical compression [24, 54].

The ability to isolate and compress single cells has led to a surge of research interest into single-cell biomechanics. Wang et al. compressed isolated tomato cells between a flat micromanipulation probe and a glass surface [76]. They used an analytical mechanical model of a fluid-filled sphere to extract the Young's modulus of the CW and found preliminary results suggesting that the Young's modulus of the CW is minimized at a pH of 4.5, which is the optimum pH for expansin activity. In direct contradiction to these results, Radotić et al. found that CW stiffness at the beginning and end of the growth cycle were almost an order of magnitude lower than during the exponential growth phase using AFM indentation [22]. Clearly, the internal structure of the cell is changing as it prepares to divide, and this changing structure affects the apparent stiffness of the CW in mechanical measurements on growing cells.

Turgor pressures in growing cells has been reported at least as high as 0.9 MPa, which results in estimated tensile wall stresses as high as 50 MPa [77, 78]. These incredibly high stress conditions can increase the effective stiffness of the cell [79]. Routier-Kierzkowska et al. observed this stiffening on top of turgid onion epidermis cells using a cellular-force microscope [15]. This new experimental apparatus was used to create stiffness maps of the onion epidermis peels, and they found that the cells appeared stiffer over the top of a turgid cell than over a junction between two or more cells. Further, the turgor pressure, which plays a significant role in the

apparent stiffness of a growing cell, has been a historically difficult parameter to measure, and is still an active area of research [27, 80].

MTs are hollow cylinders, about 24 nm in diameter, which form a fibrillar network underneath the plasma membrane of plant cells. A key function of MTs in growing cells is to guide the deposition of new cellulose in the expanding CW [81]. MTs tend to align transverse to the direction of cell growth, which is the circumferential direction of elongated cells [82–84]. In protoplasts with controlled geometries, it was found that MTs are always more anisotropically distributed than AFs [85]. AFs are smaller than MTs, at about 7 nm in diameter, and have a much shorter persistence length than MTs [53]. Durand-Smet et al. measured the rheological properties of spherical *Arabidopsis thaliana* protoplasts before and after depolymerizing MTs and AFs [54]. They found that protoplasts were significantly stiffer with MTs, but that depolymerizing AFs had no significant effect on the rheology of the protoplasts.

In this paper, we study the biomechanics of elongated and intact *Nicotiana tabacum* Bright Yellow-2 (BY-2) cells under mechanical indentations spanning from nanometer to micrometer scale. This multiscale biomechanical assay allows us to probe mechanics across the widely different size scales of each subcellular component. We calculate mechanical contributions from the cytoskeletal fibers that are a few nanometers in diameter, the cell wall, which when hydrated is around a micrometer thick, and the bulk cytoplasm which is tens of micrometers in diameter and length. To determine the effect of turgor pressure, the cells are tested in solutions of two different osmolarities. To isolate the mechanical contribution of the cytoskeleton, drug treatments are used to depolymerize MTs and remove AFs. Using a generative statistical model and a simplified mechanical spring model to analyze the results of the micro-indentation experiment, we can determine the relative stiffness contributions from the CW and cytoplasm. The stiffness contribution from the cytoplasm is further deconvoluted into the contributions from MTs, AFs, and the rest of the cytoplasm (including the vacuole). To validate the stiffness measurement of the CW from this model, we perform shallow nano-indentations on cells in the same osmotic conditions.

## **3.2 Results and Discussion**

### **Cell Morphology**

We observe the morphology of the unstained BY-2 cells using light microscopy, and upon staining with calcofluor white, the cells are also imaged with confocal

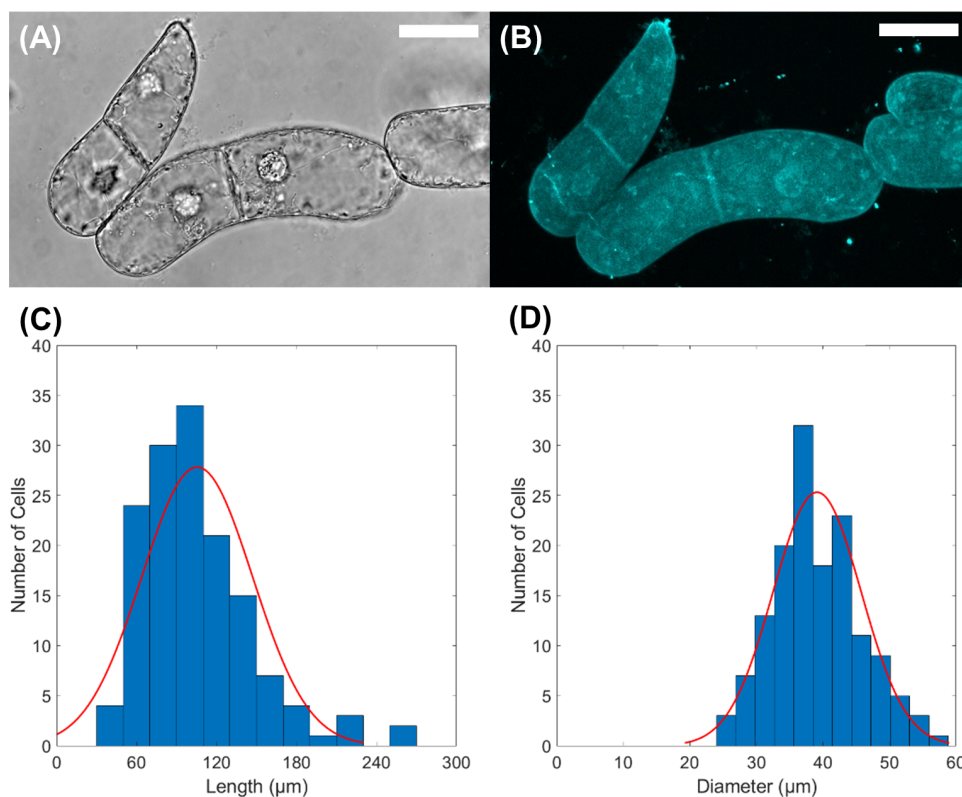


Figure 3.1: (A) Transmitted light image from BY-2 cells under confocal microscope. (B) Fluorescent image of BY-2 cells under confocal microscope. (C) Histogram showing distribution of cell length for observed BY2 cells under confocal microscope. (D) Histogram showing distribution of cell diameter for observed BY2 cells under confocal microscope. All scale bars are 40  $\mu\text{m}$ . The total number of observed cells is  $N = 145$ .

laser scanning microscopy. The CW, nucleus, and large vacuoles are visible through the transmitted and fluorescent light images (Figure 3.1A-B). The hydrated CW thickness is measured from confocal images to be  $0.88 \pm 0.02 \mu\text{m}$  (Mean  $\pm$  Standard Error), which is similar to values reported for other thin-walled cells in the literature [86]. The observed BY-2 cells are elongated, approximately cylindrical in shape, with cell length and diameter values presented in Figure 3.1C-D, as measured from light microscopy images. The mean observed cell length is  $105.43 \pm 3.45 \mu\text{m}$ , and the mean observed cell diameter is  $39.12 \pm 0.55 \mu\text{m}$ , which is similar to values previously reported in literature [83, 87].

### AFM Analysis

BY-2 cells are subjected to AFM nano-indentation tests in GM (growth media) and PS (plasmolyzing solution) to evaluate indentation moduli of the CW in solutions of different osmotic pressures. To determine the stiffness reduction of the CW upon removal of the cytoskeleton, a drug treatment which depolymerizes MTs (as in [54]) or removes AFs (as in [88, 89]) is added to the GM or PS. There are six total testing conditions: GM, GM-MT, GM-AF, PS, PS-MT, PS-AF, where -MT indicates that the drug which depolymerizes MTs was used, and -AF indicates that the drug which removes AFs was used. The osmotic pressure of testing conditions with GM is approximately 4.0 MPa, and the osmotic pressure of testing conditions with PS is approximately 2.5 MPa. See Supplementary Material for more details on the calculation of the osmotic pressure.

The AFM tip has a spherical bead of 1  $\mu$  diameter. This size tip allows us to probe the bulk behavior of the CW, as cellulose fibrils are known to be organized in the CW in bundles of 5-50 nm thickness [50]. The average indentation depth is  $126.7 \pm 7.9$  nm, which is shallow enough (with respect to the cell wall thickness) to assume that the observed mechanical response is from the CW alone [20, 22–25]. Typical force-indentation and retraction data with an overlaid Hertz model fit (Equation 1.5) is presented in Figure 3.2A, with example images from cells in each solution in the insets.

The Young's modulus results separated by treatment are presented in Figure 3.2B-C. Young's moduli measured from cells in GM are  $3.45 \pm 0.31$  MPa, while in PS they are  $231.8 \pm 15.8$  kPa. Of the drug treatments, the removal of AFs resulted in the largest reduction of average Young's modulus, in cells in both GM and PS. The depolymerization of MTs also reduced the Young's modulus in GM, but did not make a significant difference in the Young's modulus in PS. From the nano-scale measurements, we observe the evident interconnection between the cytoskeleton and CW, which is manifested through CW softening in response to the cell being subjected to drug treatments targeting the cytoskeleton. Using the non-parametric Kolmogorov-Smirnov test, the CW moduli in GM and PS are significantly different, with  $p = 4.4 * 10^{-16}$ . This  $p$ -value (comparing GM and PS moduli) is 11 orders of magnitude lower than any of the  $p$ -values comparing within the GM and PS groups. Therefore, when analyzing the less-sensitive micro-indentation data, we will only consider changes in CW stiffness in response to changes in turgor pressure.

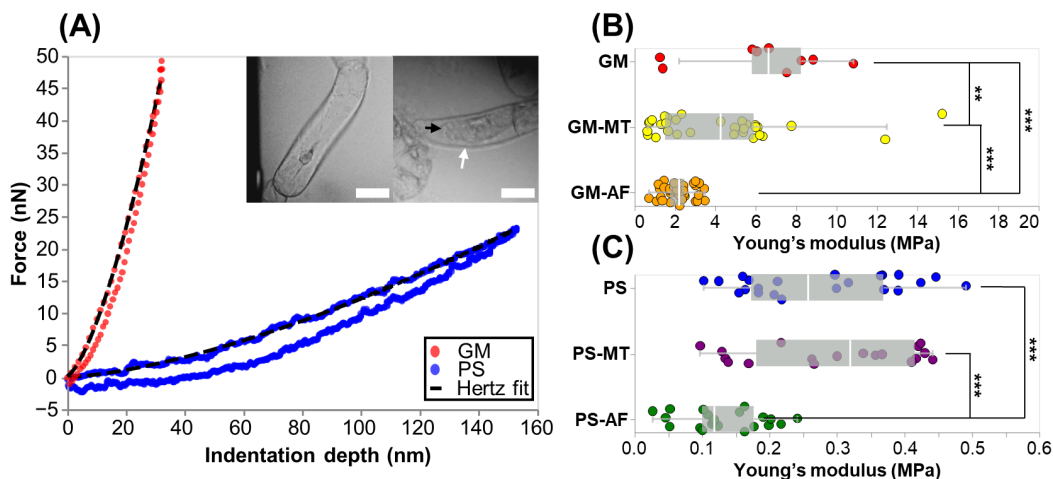


Figure 3.2: (A) Typical AFM force-indentation and retraction data from a cell in GM and in PS with Hertz fit to indentation data overlaid. Insets show corresponding images of cells in the AFM test in GM (left) and PS (right). Arrows point to cell wall (white) and retracted plasma membrane (black). Scale bars are 40  $\mu\text{m}$ . (B) Plot of indentation moduli for cells in all drug treatments in GM. (C) Plot of indentation moduli for cells in all drug treatments in PS. Note the difference in scales between (B) and (C). Each point in (B) and (C) represents an indentation test on a different cell ( $n > 9$ ). Stars indicate significant differences in distributions according to the nonparametric Kolmogorov-Smirnov test. \*\*  $p < 0.05$ , \*\*\*  $p < 0.01$ .

### Micro-Indentation Experiments & Generative Spring Model

For the micro-indentation experiments, BY-2 cells are extracted from cell culture and tested in the same six testing conditions as in the AFM experiment: GM, GM-MT, GM-AF, PS, PS-MT, PS-AF. Representative force curves and images from the micro-indentation test are provided in Figure 3.3. In Figure 3.3C, a cell in the PS is imaged with plasmolysis effects visible as the plasma membrane is peeled away from the outer CW and the cytoplasm is retracted.

The initial effective stiffness is calculated by a linear fit to the first 1 m of indentation data after contact is initiated. This indentation depth is close to the thickness of the CW measured from confocal microscopy, and hence the mechanical response of the cell is attributed to a combination of the CW and cytoplasmic materials. The empirical cumulative distribution functions (ECDFs) shown in Figure 3.4A plot stiffness thresholds against the percentage of measurements at or below that threshold. The ECDF plots enable the visualization of the distribution of stiffness measurements across treatments. Two distinct groupings of distributions are observed: suspensions of GM, and suspensions of PS. In the plots of Figure 3.4B, the quantiles of each data

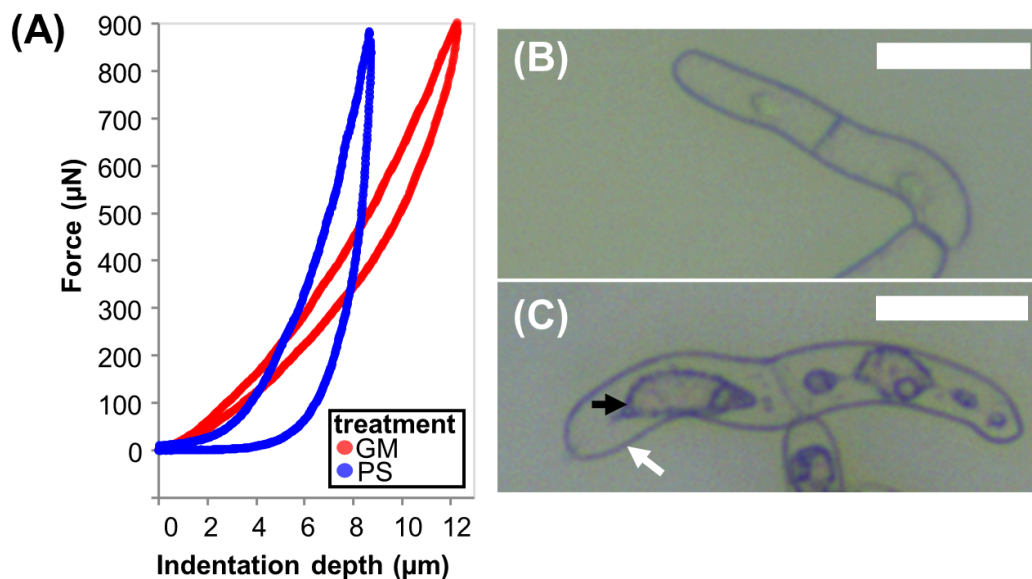


Figure 3.3: (A) Representative force-indentation and retraction data obtained in micro-indentation experiments on cells in GM (growth media) and in PS (plasmolyzing solution). (B) Image of BY-2 cell in GM taken from optical microscope of the micro-indentation testing apparatus. (C) Image of BY-2 cell in PS taken from optical microscope in micro-indentation testing apparatus with arrows pointing to the CW (white) and retracted plasma membrane (black). Scale bars are 100 μm.

set are overlaid as a boxplot on the stiffness data. There was a statistically significant difference between the PS-AF treatment and the PS-MT and PS treatments. There was no statistically significant difference between any of the groups within the GM category.

Although there was no statistically significant difference between the directly measured stiffnesses of the cells in all of the different treatments, a mechanical model is helpful to elucidate trends and effects caused by the different treatments on the mechanical contributions of sub-cellular components. In our prior work, we developed the generalized two-spring model presented in Figure 3.5 [39]. In the model, the mechanical response of a cell to micro-indentation experiments is modeled as two springs acting in series. Others have modeled the mechanical response of a cell as a single spring by reporting apparent cell stiffness [27]. In our model, the spring constants  $k_{CW}$  and  $k_{cyto}$  represent the stiffnesses of the CW and the cytoplasm, respectively, because we are interested in separating the stiffness contributions from these components. The effective stiffness of the overall cell response,  $k_{total}$ , can then

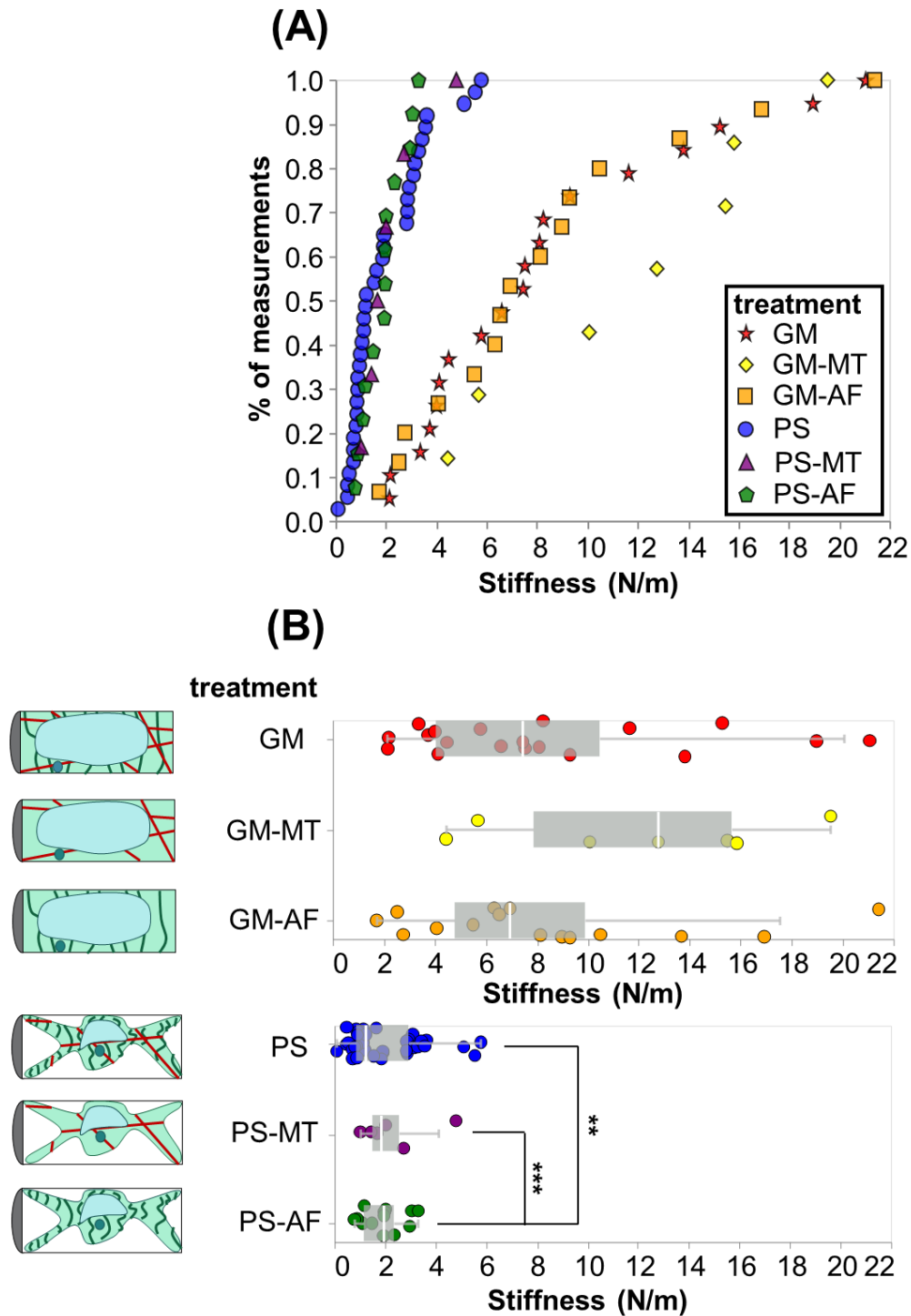


Figure 3.4: (A) Empirical cumulative distribution functions (ECDFs) for initial cell stiffness in each test condition. Each point in the plot represents an indentation test on a different cell. (B) Plot of initial cell stiffness in each test condition. Each point in the plot represents an indentation test on a different cell ( $n > 7$ ). Stars indicate significant differences in distributions according to the nonparametric Kolmogorov-Smirnov test. \*\*  $p < 0.05$ , \*\*\*  $p < 0.01$ .

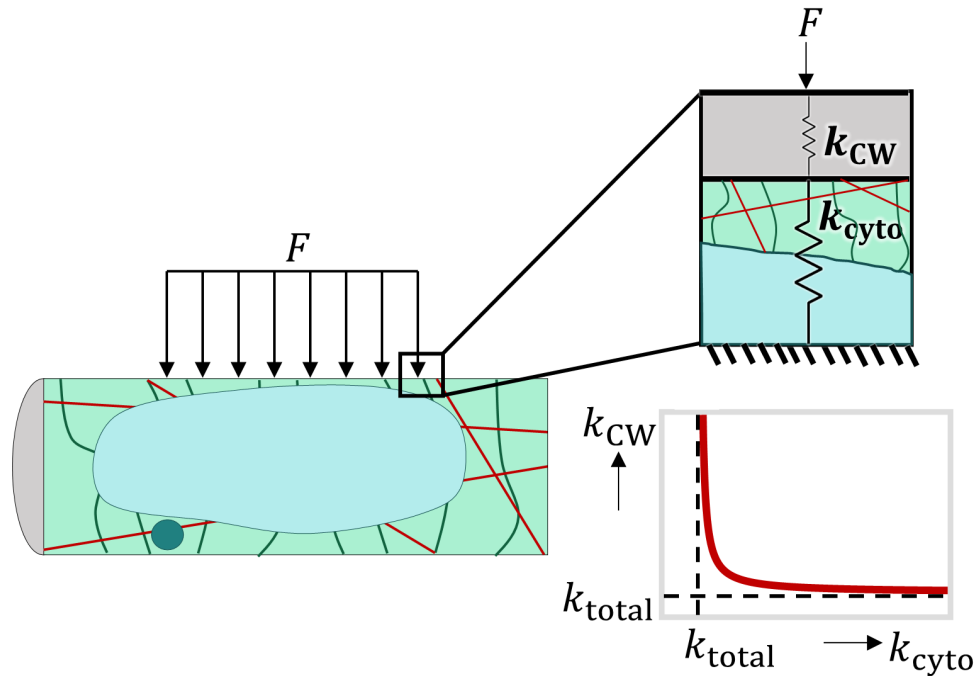


Figure 3.5: Generalized spring model for BY-2 cells in the micro-indentation test. The  $k_{CW}$  spring represents the stiffness of the CW while the  $k_{cyto}$  spring represents the total stiffness of all cytoplasmic components (including the vacuole, AFs (red lines), and MTs (green lines)).

be calculated as the combined stiffness of these two springs:

$$k_{total} = \frac{k_{CW}k_{cyto}}{k_{CW} + k_{cyto}}. \quad (3.1)$$

This simplified model of the cell response relies upon many assumptions about the structure and materials that constitute the cell. The CW and cytoplasmic materials are assumed to behave as homogeneous, isotropic, linear elastic materials at shallow indentation depths, and any nonlinear behaviors, such as viscosity, adhesion, or plasticity, are ignored. The stress in the cell away from the indenter is assumed to be negligible for shallow indentations [68].

It is important to note that stiffness here is not a material property, because it contains information about both the elastic properties of the constitutive material as well as its structure. The interpretation of stiffness with respect to subcellular structures is somewhat controversial due to the heterogeneity, anisotropy, and variability inherent to biological systems. The use of a simplified spring model reduces the number of assumptions required in the analysis as compared to a three-

dimensional model that captures the physics of a pressurized cylindrical capsule under indentation.

An illustration of the spring model adapted to each test condition is presented in Figure 3.6. We are interested in identifying the stiffness contributions from the MTs and AFs, so we model them as springs in parallel to the rest of the cytoplasmic response, with coefficients  $k_{MT}$  and  $k_{AF}$ . The cytoplasmic response is differentiated between cells in GM and cells in PS. The GM is a hypotonic solution that allows the cell to maintain turgor pressure, nutrients to flow into the cell, and the cell to expand. The PS is a hypertonic solution since the osmotic pressure of a solution that causes plasmolysis (instant response visible through microscopic views of both mechanical testing methods) must be less than the osmotic pressure of the cell. The stiffness contributions from all cytoplasmic components, except the MTs and AFs, in GM and PS solutions are represented by the spring constants  $k_{hypo}$  and  $k_{hyper}$ . To study the effects of osmotic pressure on the stiffness of the CW, we perform AFM tests in different solutions. We observe that the CW response is different between cells in GM and cells in PS, as reflected by the extracted values of the spring constants  $k_{CW,hypo}$  and  $k_{CW,hyper}$ , respectively. Results from the AFM tests also showed that changes in the CW's elastic modulus caused by depolymerizing MTs and removing AFs were much less significant than the change caused by different osmotic pressures. In our analysis we assume that the CW stiffness remains constant across drug treatments but not across osmotic solutions. We also assume that the MT and AF do not have a different stiffness in the two osmotic treatments.

In total, we have six spring stiffnesses that will be calculated through our analysis:  $k_{CW,hypo}$ ,  $k_{CW,hyper}$ ,  $k_{hypo}$ ,  $k_{hyper}$ ,  $k_{MT}$ , and  $k_{AF}$ . We also have six measurements of the effective stiffnesses from the six testing conditions: GM, GM-MT, GM-AF, PS, PS-MT, and PS-AF. Therefore, a unique solution to the system of effective stiffness equations could exist. However, the equations are nonlinear and cannot be solved analytically. Instead, we develop a statistical model.

To separate the stiffnesses of each component in the one-dimensional spring models presented in Figure 3.6, we build a generative statistical model [90, 91]. This type of analysis is used to build a posterior probability distribution  $g(\theta | y)$ , which is the probability that a set of parameters  $\theta$  describes the given experimental data  $y$ . In our case, we are interested in the posterior probability distribution for the parameters  $\theta = [k_{CW,hypo}, k_{CW,hyper}, k_{hypo}, k_{hyper}, k_{AF}, k_{MT}]$  given the data set  $y = [k_{GM}, k_{GM-MT}, k_{GM-AF}, k_{PS}, k_{PS-MT}, k_{PS-AF}]$ , where each variable in  $y$  represents a

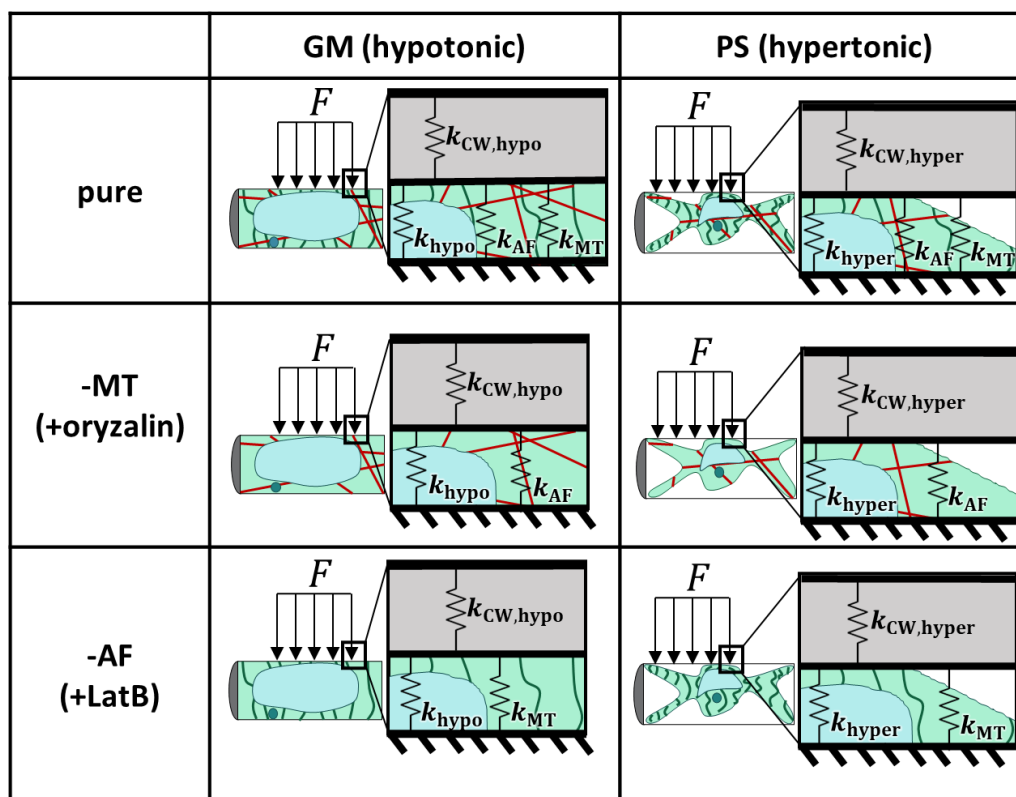


Figure 3.6: Table illustrating the spring model for each test condition. Left column represents cells in growth media (GM), which is a hypotonic solution for the cells, and right column represents cells in plasmolyzing solution (PS), which is a hypertonic solution for the cells. Top row represents cells with no added drug treatment. Second row represents cells with oryzalin drug treatment, which depolymerizes microtubules (MTs). Bottom row represents cells with Latrunculin B (LatB) drug treatment, which removes actin filaments (AFs).

vector of measurements of the stiffness from the selected treatment. Bayes' theorem provides the relationship between the posterior distribution which we would like to solve for,  $g(\theta | y)$ , the likelihood of observing our experimental data given a selected set of parameters,  $f(y | \theta)$ , and prior information about our parameters of interest,  $g(\theta)$ . The likelihood is defined separately for each treatment using a Gaussian distribution, and the prior distribution is defined empirically. See Appendix for the detailed model and implementation.

We model the overall stiffness of each cell measured in each test condition using the one-dimensional spring model in Figure 3.1. Adaptations of Equation 3.1 for each testing condition give the relationship between the mean overall stiffness in each

treatment and the stiffness of each subcellular component. The equivalent equations for the spring stiffness ( $\mu$ ) are:

$$\mu_{\text{GM}} = \frac{k_{\text{CW,hypo}} (k_{\text{hypo}} + k_{\text{AF}} + k_{\text{MT}})}{k_{\text{CW,hypo}} + k_{\text{hypo}} + k_{\text{AF}} + k_{\text{MT}}} \quad (3.2)$$

$$\mu_{\text{GM-MT}} = \frac{k_{\text{CW,hypo}} (k_{\text{hypo}} + k_{\text{AF}})}{k_{\text{CW,hypo}} + k_{\text{hypo}} + k_{\text{AF}}} \quad (3.3)$$

$$\mu_{\text{GM-AF}} = \frac{k_{\text{CW,hypo}} (k_{\text{hypo}} + k_{\text{MT}})}{k_{\text{CW,hypo}} + k_{\text{hypo}} + k_{\text{MT}}} \quad (3.4)$$

$$\mu_{\text{PS}} = \frac{k_{\text{CW,hyper}} (k_{\text{hyper}} + k_{\text{AF}} + k_{\text{MT}})}{k_{\text{CW,hyper}} + k_{\text{hyper}} + k_{\text{AF}} + k_{\text{MT}}} \quad (3.5)$$

$$\mu_{\text{PS-MT}} = \frac{k_{\text{CW,hyper}} (k_{\text{hyper}} + k_{\text{AF}})}{k_{\text{CW,hyper}} + k_{\text{hyper}} + k_{\text{AF}}} \quad (3.6)$$

$$\mu_{\text{PS-AF}} = \frac{k_{\text{CW,hyper}} (k_{\text{hyper}} + k_{\text{MT}})}{k_{\text{CW,hyper}} + k_{\text{hyper}} + k_{\text{MT}}} \quad (3.7)$$

With these six equations, we can transform the means of each of the six treatments to identify the six parameters of interest,  $\theta = [k_{\text{CW,hypo}}, k_{\text{CW,hyper}}, k_{\text{hypo}}, k_{\text{hyper}}, k_{\text{AF}}, k_{\text{MT}}]$ .

To optimize the posterior distributions for all six parameters of interest simultaneously, we combine the posterior distributions into one objective function and add six coefficients ( $a$ ,  $b$ ,  $c$ ,  $d$ ,  $e$ , and  $f$ ) that will be optimized concurrently. Mathematically, we want to maximize:

$$F = a * g_{\text{GM}}(\theta | y) + b * g_{\text{GM-MT}}(\theta | y) + c * g_{\text{GM-AF}}(\theta | y) + \dots \\ d * g_{\text{PS}}(\theta | y) + e * g_{\text{PS-MT}}(\theta | y) + f * g_{\text{PS-AF}}(\theta | y), \quad (3.8)$$

and we would like to maximize  $F$  over  $a$ ,  $b$ ,  $c$ ,  $d$ ,  $e$ ,  $f$ , and  $\theta$ . Projections of the objective function into two-dimensional space are presented in Figure 3.7. These projections illustrate the correlations between each pair of the six stiffness parameters.

Coefficients  $a$ ,  $b$ ,  $c$ ,  $d$ ,  $e$ , and  $f$  are weights multiplied in front of the posterior distributions for each of the six parameters of interest. The weights should all sum up to unity. We also add constraints on the size of the coefficients and the size of the spring constants to ensure that all components are included, and none dominate the optimization function:

$$a + b + c + d + e + f = 1 \quad (3.9)$$

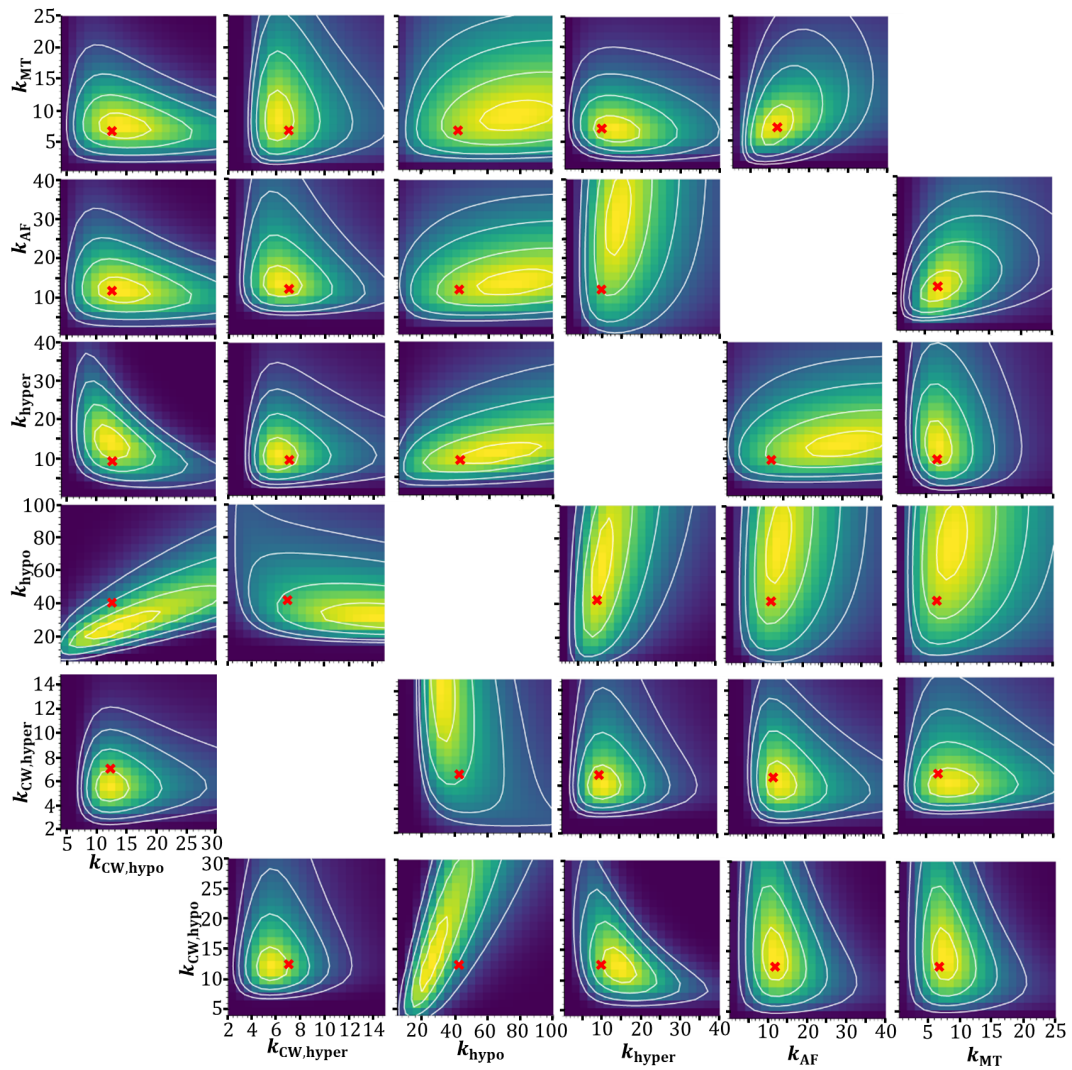


Figure 3.7: Contours of 6-dimensional posterior distribution projected in 2D space. Red x marks the point which maximizes the posterior distribution, known as the maximum a posteriori (MAP) estimate. All stiffness units are N/m.

$$0.05 \leq a, b, c, d, e, f \leq 0.5 \quad (3.10)$$

$$0.01 \leq \theta \leq 100 \quad (3.11)$$

Using a trust-region constrained optimization method, we can find the parameters  $\theta$  that maximize the posterior distributions in all treatments, under the above constraints. This point is marked by a red x in Figure 3.7. We can also construct a credible region by calculating the Hessian at the optimized point we found in parameter space. The optimum parameter values (also known as the maximum a posteriori or MAP parameter values) and credible region (which contains approximately 68% of the total probability) are reported in the following discussion as  $k_{\text{MAP}} \pm \sigma_{\text{MAP}}$  (Mean  $\pm$  Standard Deviation), and the results are visualized in Figure 3.8 for comparison.

By optimizing the objective function from the combined posterior distributions, we can decouple the relative stiffness contributions from the six identified subcellular components of interest, and the results are in line with previous reports in literature. The contribution from the cytoplasm without MTs and AFs in hypotonic conditions is the highest component evaluated ( $k_{\text{hypo}} = 42.03 \pm 2.01$  N/m), and about four times greater than that of the cytoplasm without MTs and AFs in hypertonic conditions ( $k_{\text{hyper}} = 9.68 \pm 1.50$  N/m). This is in agreement with literature which shows that turgor pressure supplies most of the stiffness for turgid cells in compression [54].

The CW in hypotonic conditions ( $k_{\text{hypo,PCW}} = 12.43 \pm 0.36$  N/m) is about twice as stiff as the CW in hypertonic conditions ( $k_{\text{hyper,PCW}} = 6.95 \pm 0.32$  N/m). The high turgor pressure in hypotonic conditions stresses the CW, making its response to compression appear stiffer. Thus, we reach the same conclusion as from AFM measurements.

The credible regions for the relative stiffness contribution from AFs ( $k_{\text{AF}} = 11.81 \pm 4.69$  N/m) and MTs ( $k_{\text{MT}} = 6.82 \pm 2.48$  N/m) overlap. However, the mere fact that these components are contributing to the mechanical resistance of the cell in compression on a similar scale as the CW and vacuole in hypertonic conditions is evidence that the cytoskeleton is an important structural component for the cell.

Cells in all treatments were indented to a force of at least 800  $\mu\text{N}$ , and the retraction force as a function of indentation depth was also measured. The area between the indentation and retraction curves represents the energy dissipated by the cell during the indentation experiment. The dissipated energies for cells in each treatment are presented as ECDFs and with overlaid boxplots in Figure 3.9. The two groups

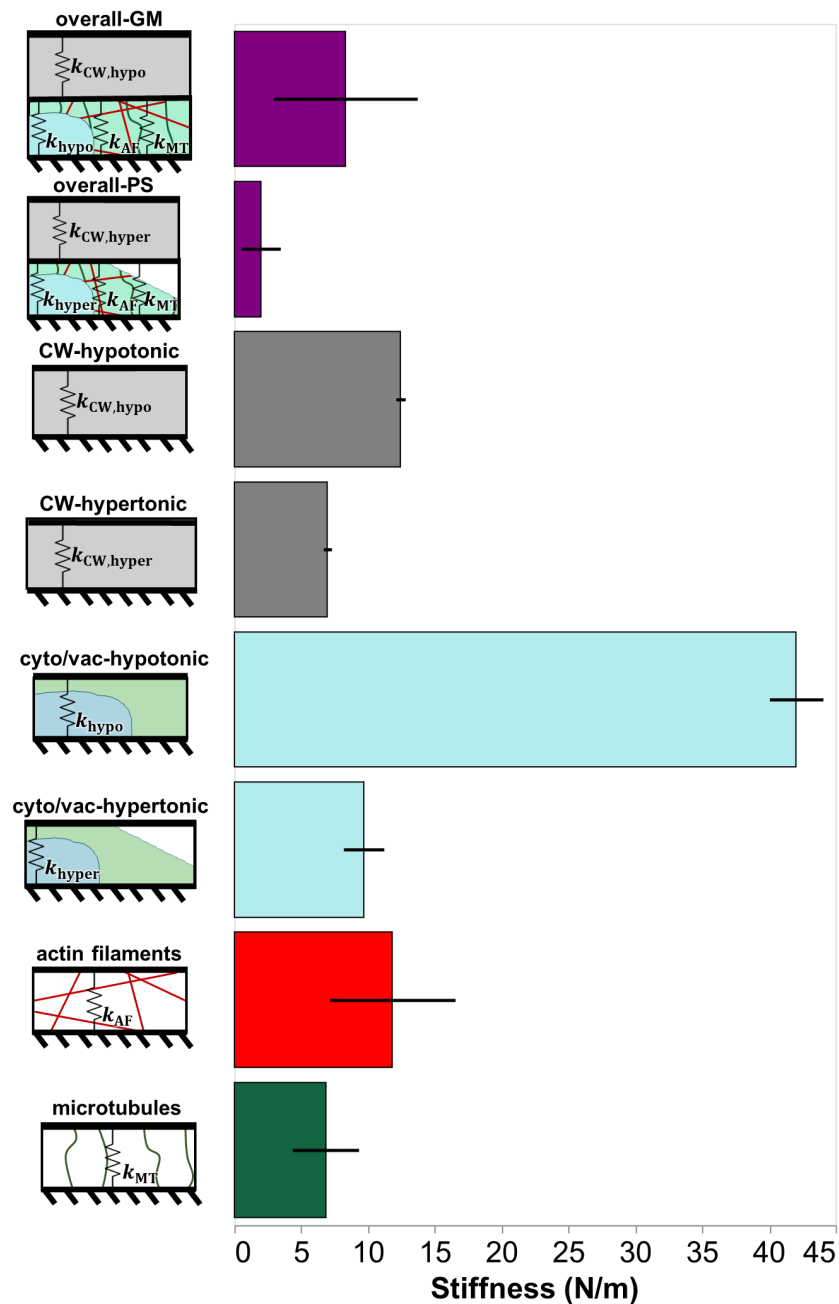


Figure 3.8: Comparison of stiffness values for the overall stiffnesses and each deconvoluted subcellular component. From top to bottom, each bar in the plot represents: overall stiffness in hypotonic and hypertonic solutions with no added drug treatments (purple), deconvoluted CW stiffness in hypotonic and hypertonic solution (grey), deconvoluted stiffness from the cytosol, vacuole, and other organelles in hypotonic and hypertonic solution (blue), deconvoluted stiffness from actin filaments (AFs) (red) and deconvoluted stiffness from the microtubules (MTs) (green). Error bars represent standard deviation, so that the range covered by the error bars represents approximately 68% of the total probability distribution for each stiffness.

of cells in GM and PS are separate, and there are significant differences detected within each of the groups. From within the GM and PS groups, the removal of AFs appears to have the most significant effect on energy dissipation calculations. Both MTs and AFs buckle under compression, which is an energy dissipation mechanism [92, 93]. The orientation of the MTs is more anisotropic than the orientation of AFs [85]. If the MTs were aligned parallel to the direction of indentation, we would expect to measure a higher dissipated energy as more of the MTs would be buckling under compression. If the MTs were aligned perpendicular to the direction of indentation, then they would not contribute to the dissipated energy. Because the cells are not always aligned the same way underneath the micro-indentation probe, the distribution of the measured dissipated energy with MTs is expected to be larger than that of AFs.

The removal of AFs seems to have the most significant effect on the energy dissipation when the significance is measured by the non-parametric Kolmogorov-Smirnov test. A non-parametric test is appropriate for these measurements, as we are trying to compare differences in the shapes of the distributions of measurements. Based on our results, we propose that removal of AFs could serve to amplify the effect of MT anisotropy on the dissipated energy, leading to a larger distribution of measurements. This hypothesis is supported further by the observation that the highest outliers of recorded energy dissipation are largely in treatments where the MTs have not been depolymerized.

Our results indicate that the cytoskeleton contributes significantly to the stiffness and dissipated energy of *Nicotiana tabacum* cells in compression. The stiffness analysis allows us to decouple the relative stiffness contributions of the MTs and AFs from the CW and the rest of the cytoplasm. The stiffness of the MTs and AFs was similar to those of all other isolated components in PS. This is in agreement with observations from Durand-Smet et al., who found that the rheological properties of protoplasts with depolymerized MTs were significantly lower than those of untreated protoplasts [54]. The removal of AFs caused the most significant difference between groups in the energy dissipation analysis, although the means of each group were not very different. This indicates that the anisotropic orientation of the MTs causes the distribution of dissipated energies to be larger, and this effect is magnified when the more isotropically distributed AFs are removed.

The highest stiffness contribution is from the cytoplasm, excluding contributions from MTs and AFs, in hypotonic conditions. This contribution is reduced by ap-

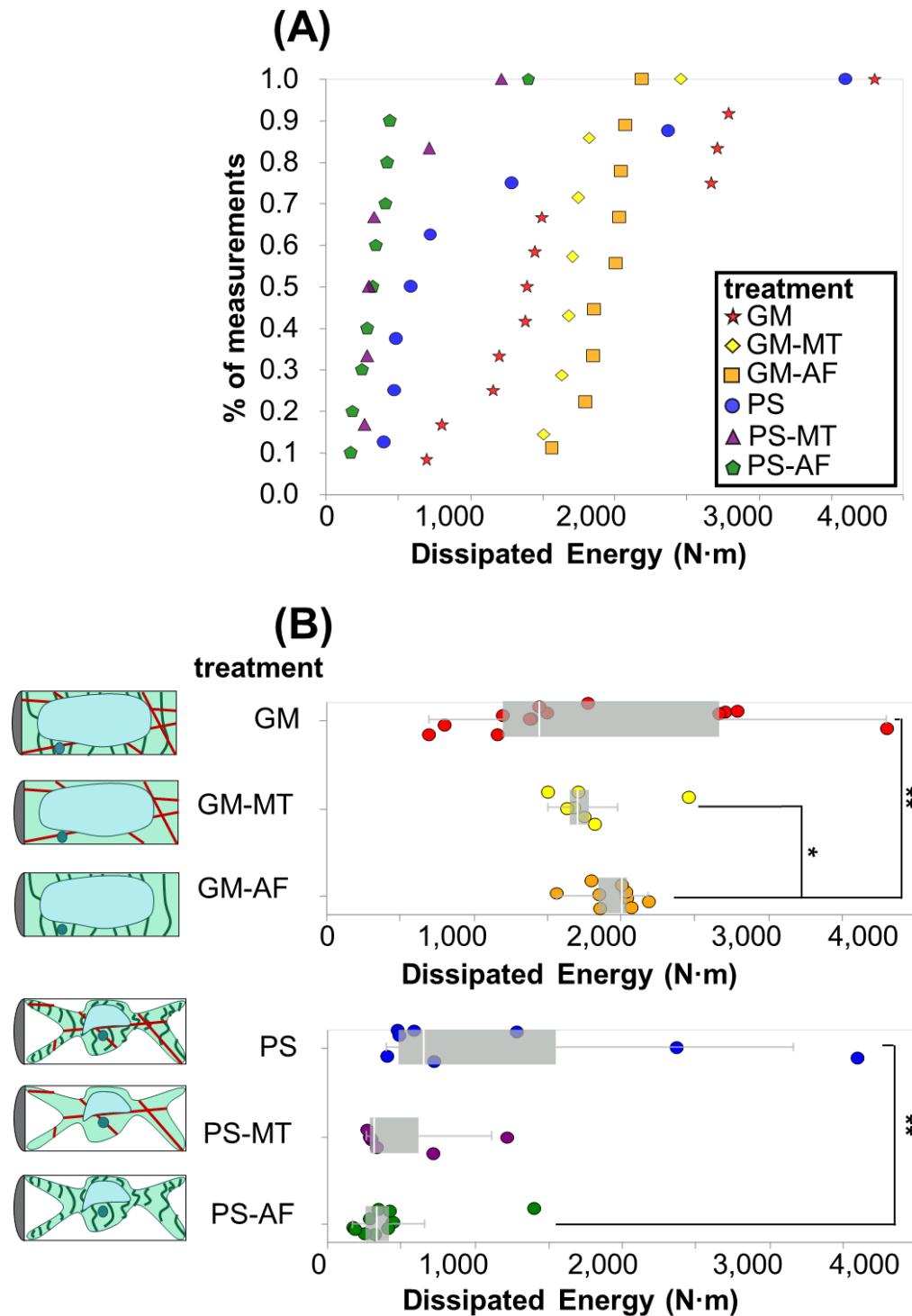


Figure 3.9: (A) Empirical cumulative distribution functions (ECDFs) for energy dissipated by cell in each test condition. Each point in the plot represents an indentation test on a different cell. (B) Plot of energy dissipated by cell in each test condition. Each point in the plot represents an indentation test on a different cell ( $n > 6$ ). Stars indicate significant differences in distributions according to the nonparametric Kolmogorov-Smirnov test. \*  $p < 0.1$ , \*\*  $p < 0.05$ .

proximately four times in hypertonic conditions, which indicates that turgor pressure is the dominant resisting component to compression. Weber et al. also reported that turgor pressure was the mechanical parameter with the most ability to resist compression, and we confirm their results with a new model and experiment [28].

Higher internal pressure stresses the CW and stiffens it. The stiffness of the CW in hypotonic conditions is estimated to be approximately twice as high as the stiffness of the CW in hypertonic conditions. This increase in stiffness in our experiment is confirmed by AFM. Cosgrove predicted that the high turgor pressures of plant cells would increase the stiffness of the CW through prestress [79]. Our results confirm this prediction.

Taken all together, the results of our AFM and micro-indentation measurements, and stiffness analysis support that (i) the cytoskeleton contributes significantly to the stiffness and energy dissipated by a cell in compression, (ii) the turgor pressure dominates the response of a turgid cell in compression, and (iii) the turgor pressure increases the stiffness of the CW through prestress.

### **3.3 Materials & Methods**

#### **Cell Cultures**

A cell culture of *Nicotiana tabacum* Bright Yellow-2 (BY-2) was maintained in suspension form and transferred in fresh media every 2 weeks at 1:10 – 1:60 dilutions. The cells were grown in 50 – 300 ml aliquots in 100 ml – 1L flasks which were kept on a rotary shaker at 130 rpm at 23°C. The cell suspension was maintained in a Linsmaier & Skoog medium with vitamins (HIMEDIA- PT040) with 3% (w/v) sucrose at a pH of 5.8. The following supplements were added: 1  $\mu$ M 2,4-dichlorophenoxyacetic acid (2,4-D), 1  $\mu$ M  $\alpha$ -naphthaleneacetic acid, and 1.46 mM KH<sub>2</sub>PO<sub>4</sub>. All chemicals and reactants were purchased from Sigma-Aldrich (St. Louis, MO, USA).

#### **Microscopy Observations**

CWs were stained with 0.005% (w/v) calcofluor white and observed under a laser scanning confocal microscope (Leica SP5 II). The cells were extracted from the culture, immersed in staining solution, and imaged without any other treatment. Z-stacks were acquired using a 40X water immersion objective (NA 1.2).

Light microscopy observations were performed to measure the dimensions of the cells. Image analysis was carried out in ImageJ (<http://rsb.info.nih.gov/ij/>). From

individual length measurements we report the statistical mean and standard error in this manuscript.

### **Mechanical Testing**

We tested the mechanical properties of the cells in two different osmotic conditions: in 1M sorbitol and in growth media (composition mentioned above).

The micro-indentation tests were performed using a FT-MTA02 system equipped with FT-S1000-LAT (liquid design) sensing probes with a 50 x 50 m<sup>2</sup> square tip (FemtoTools AG, Zurich, Switzerland) and an optical microscope. Data from indentations were position-corrected to account for contributions of the system's stiffness.

Microscope glass slides (AmScope, Irvine, CA, USA) were cleaned with isopropyl alcohol, surface activated with a high frequency generator for 1 min (BD-20A, Electro-Technic Products, Chicago, IL, USA), and a thin layer of 0.5 mL of poly-L-lysine was spin coated on top of the slides (SUSS MicroTec, Garching, Germany). Cells were extracted from culture and pipetted on the coated glass slides. The cells were washed several times with the selected treatment solution to effectively decluster them and keep only the ones that adhered better to the substrate. For testing, 1-3 mL of the selected solution were added on top of the washed and diluted cells, and force-controlled indentations to 900  $\mu$ N were conducted by immersing the sensing probe in liquid. The corresponding average indentation depth was  $13.45 \pm 0.66 \mu\text{m}$  (Mean  $\pm$  Standard Error). In the plots in Figure 3.4 and Figure 3.9, each point corresponds to the indentation of an individual cell.

Short-range nano-indentations to evaluate the properties of the CW were conducted with AFM (Asylum Research, CypherES, Goleta, CA, USA). For the indentations, we used custom tips with a silicon dioxide spherical particle (diameter 1  $\mu\text{m}$ ) on a silicon cantilever with a stiffness of 16 N/m (Novascan, Boone, IA, USA). The AFM indentations were conducted in growth media on glass slides treated for the micro-indentation tests. We conducted force-controlled indentations to 15-70 nN and applied the Hertz model (Equation 1.5) to calculate the indentation modulus,  $E$ . Each point in Figure 3.2B corresponds to an indentation test. We conducted multiple indentations for a given cell and tested a minimum of 5 cells.

## Analysis

To process the force-indentation and retraction data from the micro-indentation experiment, we follow Routier-Kierzkowska et al. [15]. In an indentation test, the compliance of the sensor increases the observed indentation depth for a given applied force to the cell. To subtract this compliance, a reference measurement is obtained by compressing an area of the glass slide with no cells to 1-2  $\mu\text{m}$ . The last 1  $\mu\text{m}$  of indentation data is fit to a line, and the slope of that line is taken to be the sensor stiffness,  $S$ . The sensor stiffness is typically at or above 200 N/m. All micro-indentation experimental data on cells are then transformed by

$$\delta_{\text{corrected}} = \delta - \frac{F}{S} \quad (3.12)$$

where  $\delta_{\text{corrected}}$  is the corrected indentation depth,  $\delta$  is the measured indentation depth, and  $F$  is the measured force.

As Routier-Kierzkowska et al., we determine the initial point of contact using a force thresholding method [15]. First, the force data is offset so that the average force up until a user-defined threshold force is zero. The contact point is then selected as the indentation depth where the force data crosses the user-defined threshold force. This offsetting and thresholding process is repeated with increasingly sensitive thresholds. The final selected threshold value is typically less than 1  $\mu\text{m}$ . A 2nd order Savitzky-Golay moving-window data filter is applied to smooth the data with a window size of 25 data points.

The first 1  $\mu\text{m}$  of filtered indentation data after the selected contact point are fit to a line. The interpolated slope is the reported stiffness of the cell in that experiment, corresponding to one data point in Figure 3.4. A Kolmogorov-Smirnov statistical test is used to compare the empirical cumulative distribution functions of initial cell stiffness in each tested treatment.

Sampling for the generative statistical modeling was performed using the Stan (2019) package within the Python programming language (Python Software Foundation, <https://www.python.org/>). The optimization to find the maximum a posteriori (MAP) parameters was performed using the SciPy (2020) optimization package, which contains a function to implement the trust-region interior point method described by Byrd et al. (1999). All data visualizations were created using Altair (2018).

AFM nano-indentation data was processed using Asylum Research software (AR 16.10.211) in Igor Pro 6.3. The software was used to identify the contact point and

extract a Young's modulus through the application of the Hertz contact model.

### **Funding**

This work was supported by the University of Washington and the Resnick Sustainability Institute at Caltech (CD).

### **Acknowledgements**

The authors thank Dr. Wai Pang Chan for obtaining the confocal microscopy images and Dr. Josep Vilarrasa-Blasi for preparing a subset of the solutions. We also thank Dr. Josep Vilarrasa-Blasi and Dr. Luca Bonanomi for the helpful discussions.

### **Appendix**

#### **Calculation of Osmotic Pressure in Each Treatment**

The osmotic pressure of the GM and PS was calculated using a form of the ideal gas law:

$$\Pi = iMRT, \quad (3.13)$$

where  $\Pi$  is the osmotic pressure,  $i$  is the van't Hoff factor,  $M$  is the Molar concentration of the solution,  $R$  is the ideal gas constant, and  $T$  is temperature. The osmotic pressure of the GM is approximately 4.0 MPa, and the osmotic pressure of the PS is approximately 2.5 MPa. The drug treatments used to knock out the MTs or AFs had a negligible effect on the osmotic pressure of the solution.

#### **Bayesian Generative Model Definition**

Bayes' theorem is:

$$g(\theta | y) = \frac{f(y | \theta)g(\theta)}{f(y)}. \quad (3.14)$$

Note that the denominator in Bayes' theorem,  $f(y)$ , called the evidence, does not depend on  $\theta$ , so it is a normalization constant. The evidence,  $f(y)$ , can be calculated:

$$f(y) = \int f(y | \theta)g(\theta)d\theta, \quad (3.15)$$

where the limits of this integral are the limits of all possible values of the parameters  $\theta$ . It is unnecessary for our purposes to consider this term explicitly.

The central limit theorem establishes that a measurement that depends on many subprocesses tends to be Gaussian distributed. Some of the many subprocesses that affect our measurements are the variations in the effect of the drug treatment and osmolarity of the solution in which the cells are tested in, the size and shape of

the cells, the orientation of the cell and subcellular components with respect to the indenter, and the adhesion of the cell to the substrate and any subsequent movement of the cell under the indenter. This is not an exhaustive list but includes the most significant processes. So, we will assume that each of our sets of experimental measurements  $(k_{\text{treatment}})_i$  is Gaussian distributed with mean  $\mu_{\text{treatment}}$  and standard deviation  $\sigma_{\text{treatment}}$ . We will also assume that each of our measurements within each treatment is independent and identically distributed. Therefore, we can define the probability density function of the likelihood for each of our measurements:

$$f((k_{\text{treatment}})_i | \mu_{\text{treatment}}, \sigma_{\text{treatment}}) = \frac{1}{\sqrt{2\pi\sigma_{\text{treatment}}^2}} e^{-\frac{((k_{\text{treatment}})_i - \mu_{\text{treatment}})^2}{2\sigma_{\text{treatment}}^2}}. \quad (3.16)$$

Since each measurement within a specified treatment is sampled independently, the likelihood of the entire data set is a multiplication of the likelihoods for each measurement in that treatment:

$$f(k_{\text{treatment}} | \mu_{\text{treatment}}, \sigma_{\text{treatment}}) = \prod_{i=1}^{n_{\text{treatment}}} \frac{1}{\sqrt{2\pi\sigma_{\text{treatment}}^2}} e^{-\frac{((k_{\text{treatment}})_i - \mu_{\text{treatment}})^2}{2\sigma_{\text{treatment}}^2}}, \quad (3.17)$$

where  $n_{\text{treatment}}$  is the total number of measurements in a specified treatment.

We use uninformative prior distributions for  $g(\theta, \sigma)$  because we have very little information about the values that these parameters will have before examining the experimental data. We know that all of the parameters must be greater than zero, and from literature on stiffness values of similar plant cells, we can anticipate that the stiffnesses will each be less than 100 N/m [15, 39]. By trial and error, a log-normal prior distribution for the parameters  $\theta$  was found to cover the range of expected values and give reasonable resulting data sets:

$$g(\theta) = \frac{1}{0.75 * \theta \sqrt{2\pi} e^{-\frac{(\ln x - \ln 15)^2}{2 * 0.75^2}}}. \quad (3.18)$$

The standard deviation in each treatment,  $\sigma$ , is assumed to be proportional to the magnitude of the mean stiffness in each treatment:

$$\sigma_{\text{treatment}} = 0.5 * \mu_{\text{treatment}}. \quad (3.19)$$

Finally, we assume that the distributions for  $\theta$  and  $\sigma$  are independent so that:

$$g(\theta, \sigma) = g(\theta)g(\sigma). \quad (3.20)$$

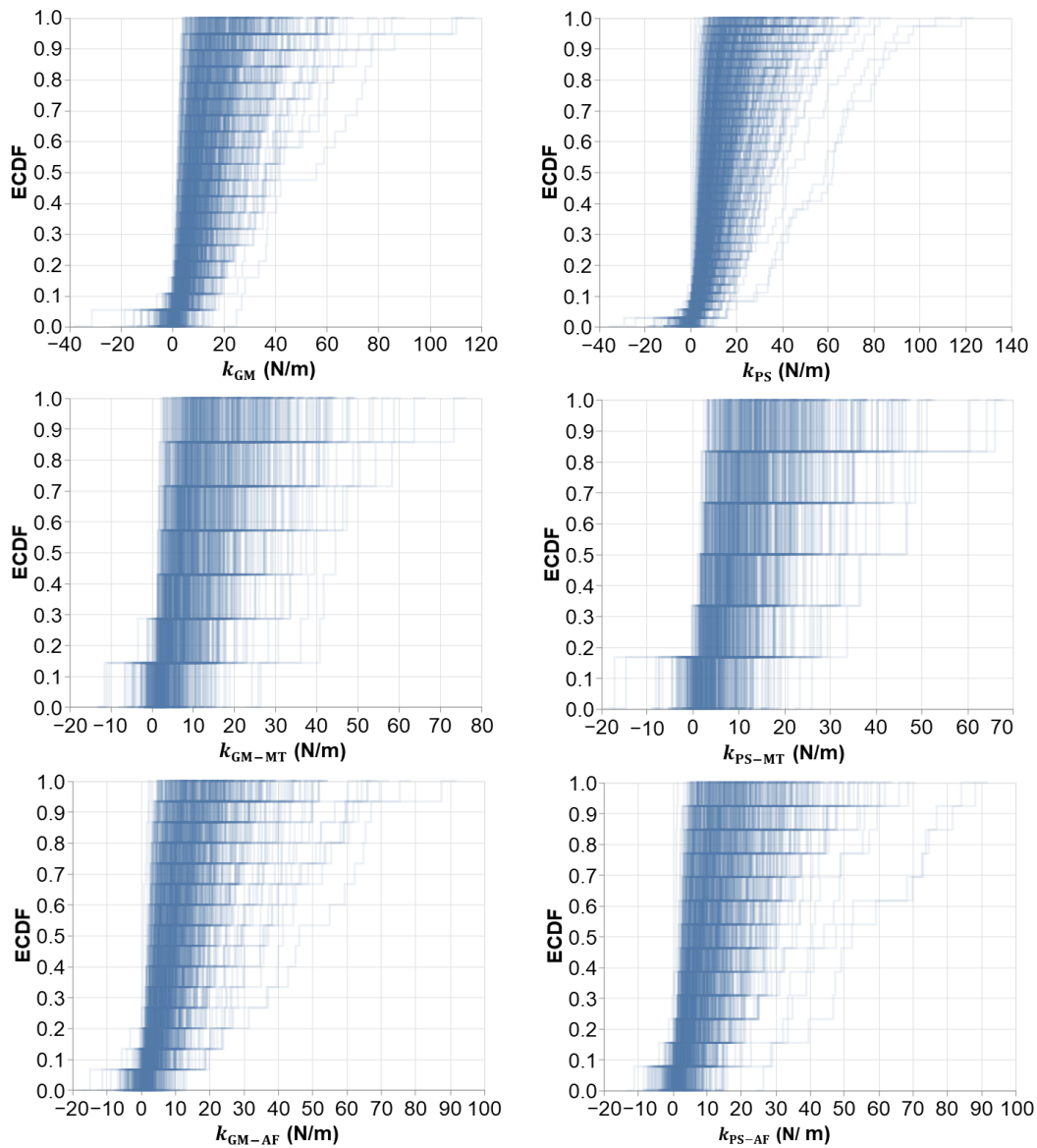


Figure 3.10: Prior predictive checks. Each line represents a sample data set drawn using the fully generative model described in equations above. Each subplot contains 500 draws of data sets that are the same size as the respective number of experimental samples in that treatment.

With the prior distributions defined, we can generate data sets from the fully generative model. These generated data sets are known as prior predictive checks, and they ensure that the model does not generate many unrealistic or unphysical values when drawing random data sets from the previously defined distributions. See Figure S1 for example data sets drawn from the completed generative model.

## References

- [3] Daniel J. Cosgrove. “Assembly and enlargement of the primary cell wall in plants”. In: *Annual Review of Cell and Developmental Biology* 13.1 (1997). PMID: 9442872, pp. 171–201. DOI: 10.1146/annurev.cellbio.13.1.171. eprint: <https://doi.org/10.1146/annurev.cellbio.13.1.171>. URL: <https://doi.org/10.1146/annurev.cellbio.13.1.171>.
- [15] Anne-Lise Routier-Kierzkowska et al. “Cellular Force Microscopy for in Vivo Measurements of Plant Tissue Mechanics”. In: *Plant Physiology* 158.4 (2012), pp. 1514–1522. ISSN: 0032-0889. DOI: 10.1104/pp.111.191460. eprint: <http://www.plantphysiol.org/content/158/4/1514.full.pdf>. URL: <http://www.plantphysiol.org/content/158/4/1514>.
- [20] Siobhan A. Braybrook and Alexis Peaucelle. “Mechano-Chemical Aspects of Organ Formation in *Arabidopsis thaliana*: The Relationship between Auxin and Pectin”. In: *PLOS ONE* 8.3 (Mar. 2013), pp. 1–10. DOI: 10.1371/journal.pone.0057813. URL: <https://doi.org/10.1371/journal.pone.0057813>.
- [22] Ksenija Radotić et al. “Atomic force microscopy stiffness tomography on living *Arabidopsis thaliana* cells reveals the mechanical properties of surface and deep cell-wall layers during growth”. eng. In: *Biophysical Journal* 103.3 (Aug. 2012), pp. 386–394. ISSN: 1542-0086. DOI: 10.1016/j.bpj.2012.06.046.
- [23] Pascale Milani, Siobhan A. Braybrook, and Arezki Boudaoud. “Shrinking the hammer: micromechanical approaches to morphogenesis”. In: *Journal of Experimental Botany* 64.15 (July 2013), pp. 4651–4662. ISSN: 0022-0957. DOI: 10.1093/jxb/ert169. eprint: <https://academic.oup.com/jxb/article-pdf/64/15/4651/18043081/ert169.pdf>. URL: <https://doi.org/10.1093/jxb/ert169>.
- [24] Arun Sampathkumar et al. “Subcellular and supracellular mechanical stress prescribes cytoskeleton behavior in *Arabidopsis* cotyledon pavement cells”. In: *eLife* 3 (Apr. 2014). Ed. by Dominique Bergmann, e01967. ISSN: 2050-084X. DOI: 10.7554/eLife.01967. URL: <https://doi.org/10.7554/eLife.01967>.
- [25] Siobhan A. Braybrook. “Chapter 13 - Measuring the elasticity of plant cells with atomic force microscopy”. In: *Biophysical Methods in Cell Biology*. Ed. by Ewa K. Paluch. Vol. 125. Methods in Cell Biology. Academic Press, 2015, pp. 237–254. DOI: <https://doi.org/10.1016/bs.mcb.2014.10.006>. URL: <http://www.sciencedirect.com/science/article/pii/S0091679X14000077>.

- [27] Léna Beauzamy, Julien Derr, and Arezki Boudaoud. “Quantifying hydrostatic pressure in plant cells by using indentation with an atomic force microscope”. In: *Biophysical journal* 108.10 (2015), pp. 2448–2456.
- [28] Alain Weber et al. “Measuring the mechanical properties of plant cells by combining micro-indentation with osmotic treatments”. In: *Journal of Experimental Botany* 66.11 (Apr. 2015), pp. 3229–3241. ISSN: 0022-0957. DOI: [10.1093/jxb/erv135](https://doi.org/10.1093/jxb/erv135). eprint: <https://academic.oup.com/jxb/article-pdf/66/11/3229/17137090/erv135.pdf>. URL: <https://doi.org/10.1093/jxb/erv135>.
- [39] Leah Ginsberg et al. “Structure and Biomechanics during Xylem Vessel Transdifferentiation in *Arabidopsis thaliana*”. en. In: *Plants* 9.12 (Dec. 2020), p. 1715. ISSN: 2223-7747. DOI: [10.3390/plants9121715](https://doi.org/10.3390/plants9121715). URL: <https://www.mdpi.com/2223-7747/9/12/1715>.
- [50] Robert J. Moon et al. “Cellulose nanomaterials review: structure, properties and nanocomposites”. In: *Chem. Soc. Rev.* 40 (7 2011), pp. 3941–3994. DOI: [10.1039/C0CS00108B](https://doi.org/10.1039/C0CS00108B). URL: <http://dx.doi.org/10.1039/C0CS00108B>.
- [53] F Gittes et al. “Flexural rigidity of microtubules and actin filaments measured from thermal fluctuations in shape.” In: *Journal of Cell Biology* 120.4 (Feb. 1993), pp. 923–934. ISSN: 0021-9525. DOI: [10.1083/jcb.120.4.923](https://doi.org/10.1083/jcb.120.4.923). eprint: <https://rupress.org/jcb/article-pdf/120/4/923/384296/923.pdf>. URL: <https://doi.org/10.1083/jcb.120.4.923>.
- [54] Pauline Durand-Smet et al. “A Comparative Mechanical Analysis of Plant and Animal Cells Reveals Convergence across Kingdoms”. In: *Biophysical Journal* 107.10 (2014), pp. 2237–2244. ISSN: 0006-3495. DOI: <https://doi.org/10.1016/j.bpj.2014.10.023>. URL: <http://www.sciencedirect.com/science/article/pii/S0006349514010741>.
- [68] Joseph Boussinesq. “Application des potentials al’etude de l’equilibre et des mouvements des solides elastiques”. In: *Paris, Ganther-Villars* (1885).
- [76] C. X. WANG, L. WANG, and C. R. THOMAS. “Modelling the Mechanical Properties of Single Suspension-Cultured Tomato Cells”. In: *Annals of Botany* 93.4 (Apr. 2004), pp. 443–453. ISSN: 0305-7364. DOI: [10.1093/aob/mch062](https://doi.org/10.1093/aob/mch062). eprint: <https://academic.oup.com/aob/article-pdf/93/4/443/497606/mch062.pdf>. URL: <https://doi.org/10.1093/aob/mch062>.
- [77] Daniel J. Cosgrove. “Water Uptake by Growing Cells: An Assessment of the Controlling Roles of Wall Relaxation, Solute Uptake, and Hydraulic Conductance”. In: *International Journal of Plant Sciences* 154.1 (1993). PMID: 11537965, pp. 10–21. DOI: [10.1086/297087](https://doi.org/10.1086/297087). eprint: <https://doi.org/10.1086/297087>. URL: <https://doi.org/10.1086/297087>.

- [78] Daniel B. Szymanski and Daniel J. Cosgrove. “Dynamic Coordination of Cytoskeletal and Cell Wall Systems during Plant Cell Morphogenesis”. In: *Current Biology* 19.17 (2009), R800–R811. ISSN: 0960-9822. DOI: <https://doi.org/10.1016/j.cub.2009.07.056>. URL: <http://www.sciencedirect.com/science/article/pii/S0960982209014821>.
- [79] DJ Cosgrove. “Catalysts of plant cell wall loosening”. In: *F1000Research* 5.119 (2016). DOI: [10.12688/f1000research.7180.1](https://doi.org/10.12688/f1000research.7180.1).
- [80] Richard Malgat, François Faure, and Arezki Boudaoud. “A Mechanical Model to Interpret Cell-Scale Indentation Experiments on Plant Tissues in Terms of Cell Wall Elasticity and Turgor Pressure”. In: *Frontiers in Plant Science* 7 (Sept. 7, 2016). ISSN: 1664-462X. DOI: [10.3389/fpls.2016.01351](https://doi.org/10.3389/fpls.2016.01351). URL: <http://journal.frontiersin.org/Article/10.3389/fpls.2016.01351/abstract> (visited on 11/06/2019).
- [81] Takashi Hashimoto. “Microtubules in Plants”. In: *The Arabidopsis Book* 13 (Jan. 2015), e0179. ISSN: 1543-8120. DOI: [10.1199/tab.0179](https://doi.org/10.1199/tab.0179). URL: <http://www.bioone.org/doi/10.1199/tab.0179> (visited on 01/04/2021).
- [82] Andrei Smertenko et al. “A new class of microtubule-associated proteins in plants”. In: *Nature Cell Biology* 2.10 (Oct. 2000), pp. 750–753. ISSN: 1465-7392, 1476-4679. DOI: [10.1038/35036390](https://doi.org/10.1038/35036390). URL: [http://www.nature.com/articles/ncb1000\\_750](http://www.nature.com/articles/ncb1000_750) (visited on 01/24/2021).
- [83] Björn J. Sieberer et al. “Cell proliferation, cell shape, and microtubule and cellulose microfibril organization of tobacco BY-2 cells are not altered by exposure to near weightlessness in space”. In: *Planta* 230.6 (Nov. 2009), pp. 1129–1140. ISSN: 0032-0935, 1432-2048. DOI: [10.1007/s00425-009-1010-7](https://doi.org/10.1007/s00425-009-1010-7). URL: <http://link.springer.com/10.1007/s00425-009-1010-7> (visited on 01/13/2021).
- [84] Rhoda J. Hawkins, Simon H. Tindemans, and Bela M. Mulder. “Model for the orientational ordering of the plant microtubule cortical array”. In: *Physical Review E* 82.1 (July 19, 2010), p. 011911. ISSN: 1539-3755, 1550-2376. DOI: [10.1103/PhysRevE.82.011911](https://doi.org/10.1103/PhysRevE.82.011911). URL: <https://link.aps.org/doi/10.1103/PhysRevE.82.011911> (visited on 01/24/2021).
- [85] Pauline Durand-Smet et al. “Cytoskeletal organization in isolated plant cells under geometry control”. In: *Proceedings of the National Academy of Sciences* 117.29 (2020), pp. 17399–17408. ISSN: 0027-8424. DOI: [10.1073/pnas.2003184117](https://doi.org/10.1073/pnas.2003184117). eprint: <https://www.pnas.org/content/117/29/17399.full.pdf>. URL: <https://www.pnas.org/content/117/29/17399>.
- [86] P Rezvani Moghaddam and D Wilman. “Cell wall thickness and cell dimensions in plant parts of eight forage species”. In: *The journal of agricultural science* 131.1 (1998), pp. 59–67.

- [87] Milada Čovanová et al. “Overexpression of the Auxin Binding PROTEIN1 Modulates PIN-Dependent Auxin Transport in Tobacco Cells”. In: *PLoS ONE* 8.7 (July 23, 2013). Ed. by Markus Grebe, e70050. ISSN: 1932-6203. DOI: 10.1371/journal.pone.0070050. URL: <https://dx.plos.org/10.1371/journal.pone.0070050> (visited on 01/13/2021).
- [88] Jan Maisch et al. “Tobacco Arp3 is localized to actin-nucleating sites in vivo”. In: *Journal of Experimental Botany* 60.2 (Feb. 2009), pp. 603–614. ISSN: 1460-2431, 0022-0957. DOI: 10.1093/jxb/ern307. URL: <https://academic.oup.com/jxb/article-lookup/doi/10.1093/jxb/ern307> (visited on 01/19/2021).
- [89] Steffen Durst et al. “Organization of perinuclear actin in live tobacco cells observed by PALM with optical sectioning”. In: *Journal of Plant Physiology* 171.2 (Jan. 2014), pp. 97–108. ISSN: 01761617. DOI: 10.1016/j.jplph.2013.10.007. URL: <https://linkinghub.elsevier.com/retrieve/pii/S0176161713004161> (visited on 01/19/2021).
- [90] Justin Bois. *Introduction to Bayesian Modeling*. Sept. 2018. URL: [http://bebi103.caltech.edu.s3-website-us-east-1.amazonaws.com/2018/lecture\\_notes/l05\\_intro\\_to\\_bayesian\\_modeling.pdf](http://bebi103.caltech.edu.s3-website-us-east-1.amazonaws.com/2018/lecture_notes/l05_intro_to_bayesian_modeling.pdf).
- [91] Michael Betancourt. *Probabilistic Modeling and Statistical Inference*. betanalphabet.github.io. Mar. 2019. URL: [https://betanalphabet.github.io/assets/case\\_studies/modeling\\_and\\_inference.html](https://betanalphabet.github.io/assets/case_studies/modeling_and_inference.html).
- [92] Ovijit Chaudhuri, Sapun H. Parekh, and Daniel A. Fletcher. “Reversible stress softening of actin networks”. In: *Nature* 445.7125 (Jan. 2007), pp. 295–298. ISSN: 0028-0836, 1476-4687. DOI: 10.1038/nature05459. URL: <http://www.nature.com/articles/nature05459> (visited on 11/06/2019).
- [93] Teng Li. “A mechanics model of microtubule buckling in living cells”. In: *Journal of Biomechanics* 41.8 (2008), pp. 1722–1729. ISSN: 00219290. DOI: 10.1016/j.jbiomech.2008.03.003. URL: <https://linkinghub.elsevier.com/retrieve/pii/S0021929008001176> (visited on 02/17/2021).

*Chapter 4*INVERSE ANALYSIS TO DETERMINE THE MECHANICAL  
PROPERTIES OF SINGLE BACTERIAL CELLS**Abstract**

Biological systems have an inherent variability that complicates the interpretation of indentation measurements with respect to subcellular structures. In this work, we simulate atomic force microscopy (AFM) indentations on a gram-negative bacterium, *Escherichia coli*, and perform a sensitivity study and inverse analysis to search for a unique solution to the cell wall (CW) elastic modulus and turgor pressure simultaneously. Sensitivity study results reveal that uncertainty in turgor pressure and CW elastic modulus indeed contribute the most to variability in force spectra from AFM indentations. The two-dimensional parameter space of possible values for CW elastic modulus and turgor pressure is meshed using triangular elements. "Simulated experiments" are tested throughout the parameter space, and correlations between the CW elastic modulus and turgor pressure, which depend on the type of objective function, are investigated. Two unique objective functions are tested in the inverse analysis, and a third objective function, which is a weighted sum of the first two, is found to reduce errors in estimated CW elastic modulus and turgor pressure by 20% and 11%, respectively. The use of this type of inverse analysis has the potential to elucidate the material properties of cell walls using a single indentation measurement and reliably decouple these properties from the high turgor pressures inside walled cells.

**4.1 Introduction**

The interplay between turgor pressure and CW elasticity impacts cell growth, division, and motility [94]. Many experimental methods have been developed to measure turgor pressure, including the direct insertion of a pressure gauge [8, 9], incipient plasmolysis [10], collapse of gas vesicles in the cytoplasm [11], and atomic-force microscopy (AFM) [13]. More commonly, AFM is used to measure CW elasticity [95]. The use of AFM is widespread, so there is a plethora of nanoindentation measurements on isolated cells and CWs in a variety of environments. For a review of the different types of measurements on microbes using AFM, see [96]. However, the interpretation of these measurements with respect to cellular structures is

controversial due to the heterogeneity, anisotropy, and variability inherent to biological systems. There exists an opportunity to advance our understanding of basic cellular physics by developing a mechanical model of the AFM force-indentation experiment with the ability to decouple two or more mechanical properties of a cell simultaneously, such as CW elasticity, turgor pressure, viscoelasticity, adhesion, and plasticity.

Overall cell stiffness measurements remove the need to make any assumptions about the structure of the cell, and can be a reliable indicator of the cell health. When walled cells are healthy and growing, they maintain a constant turgor pressure. When exposed to different chemicals and/or drug treatments, CW damage can cause a cell to lose the ability to maintain turgor, or the cell may actively pump water out of its vacuole in response to the treatment. For example, Volle et al. investigated the use of a certain antimicrobial peptide as an alternative to traditional antibiotics [38]. They found that the overall cell stiffness decreased by about half after treatment with the antimicrobial peptide, indicating that the treatment was detrimental to cell health. However, it is not clear if the treatment reduced overall cell stiffness through weakening of the cell envelope, or through another mechanism that affected the cells' ability to maintain turgor pressure. A mechanical model which could reliably decouple turgor pressure and CW elasticity from their AFM force spectra would advance our understanding of the physical effect that this antimicrobial peptide treatment had on the bacterial cells tested.

Some have found evidence that for shallow indentations, AFM measurements only probe the mechanical response of the cell envelope or CW material. For example, Bailey et al. measured response of the gram-positive *Staphylococcus aureus* under compression using an AFM [97]. They also measured the response of CWs extracted from live cells, and cells with a permanently damaged cell membrane, so as to remove turgor pressure from the cell. All of these measurements were consistent, so they concluded that for indentations less than approximately the thickness of the CW, the AFM measurement only probed the mechanical response of the CW. Tvergaard and Needleman discovered additional numerical evidence that supports this experimental observation [98]. They created a double-layer cell model with a constant pressure and studied the response under compression from a conical indenter. For sufficiently shallow indentations, the mechanical response was dominated by only the CW material, and at deeper indentations the turgor pressure began to play a major role in the response. Still, others have shown that turgor pressure leads to a stress stiffening

of the CW. For example, Deng et al. found that the elastic modulus of the CW in the gram-negative *Escherichia coli* under compression from a conical AFM tip was significantly higher in living cells than in unpressurized sacculi [29]. These seemingly contradictory findings highlight the importance of developing a model of the entire cell as a fluid-filled structure with an internal hydrostatic pressure to investigate the convoluted mechanics of the CW and turgor pressure.

Here, we perform a sensitivity study to determine the contributions of error incurred from variations in geometry and elasticity of the CW material. After determining that CW elastic modulus and turgor pressure are in fact the most significant contribution to the response of a cell under AFM nanoindentation, a minimalistic model of a cell as a pressurized sphere with constant volume is used in an inverse analysis. Similar analyses have been carried out to determine material properties of engineering materials under AFM nanoindentation [99]. We find correlations between CW modulus and turgor pressure that depend on the form of objective function used. A novel objective function, which accounts for two different facets of the force-indentation data, is then used to determine optimal CW modulus and turgor pressure. This objective function reduced errors in estimated CW modulus by 15% and turgor pressure by 10% on average.

## 4.2 Model

To enhance our understanding of AFM measurements on isolated bacterial cells, we explore the deformation of a pressurized and fluid-filled body, subject to a compressive force from a rigid and spherical indenter. We select parameter values representative of *Escherichia coli*, a gram-negative bacteria. Finite-element models (FEMs) of the bacterium under indentation are constructed using Abaqus/CAE and simulations are run using the Abaqus/Standard Solver [100].

At very small indentation depths, and for AFM tips with a radius much smaller than that of the cell under indentation, the CW can be idealized as an infinite half-space, and Hertz contact theory (Equation 1.5) can be used to extract the elastic modulus of the CW [42]. If the CW is very thin, as in gram-negative bacteria, this assumption breaks down. Instead, Reissner's thin shell model can be used to extract the elastic modulus of thin CW, still assuming that the indentation depth is shallow and now idealizing the CW as a thin shell [45]. At large indentation depths, the shell becomes unstable and eventually develops Pogorelov's ridge as a result of the top surface of the shell buckling inwards [46]. More recently, Vella et al.

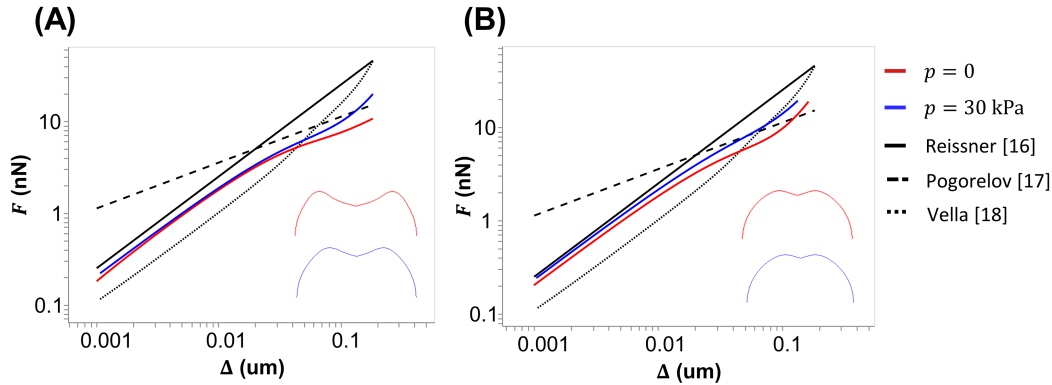


Figure 4.1: Comparison between simulations with no turgor pressure (red line) and 30 kPa of turgor pressure (blue line) to predictions of models from literature. Reissner [45] (solid black line) described the response of a spherical shell with a constant zero internal pressure undergoing small deformations. Pogorelov [46] (dashed black line) described the response of a spherical shell with a constant zero internal pressure undergoing large deformation, and in particular the mirror buckling phenomenon, which is visible in the insets. Vella [14] (dotted black line) described the response of a spherical shell with a constant high internal pressure undergoing large deformation. (A) Simulations are altered to maintain constant internal pressure, as assumed in Reissner [45], Pogorelov [46] and Vella [14]. (B) Simulations are presented with constant internal volume, as used in the subsequent analysis of this chapter. Insets show the final deformed shape of the spherical shell under point load in each simulation.

developed analytical expressions to describe the deformation of highly pressurized spherical shells at asymptotically small and large indentation depths [14]. All of these analytical expressions assume constant pressure inside the sphere, whereas our simulations assume constant volume. We selected a constant volume model because we want to ignore the convoluted effects of viscosity and porosity in the model, and this requires an experiment at short time scales. Because osmosis takes a few seconds in most bacteria, an indentation that lasts less than a second should not involve the opening of any mechanosensitive channels, and therefore the volume of the cytoplasm should stay more or less constant throughout the experiment. A comparison between results from our FEM and analytical expressions presented in literature is shown in Figure 4.1.

A schematic view of the simulations is presented in Figure 4.2. In each simulation, a spherical or elongated cell is filled with an incompressible fluid to represent the cytoplasm. The radius of the cytoplasm is defined as  $R_c = 1 \mu\text{m}$ . The initial thickness of the cell envelope is  $t$ , which is in the range of 25-35 nm [101]. The radius of the spher-

ical AFM tip is specified as  $R_i = 62.5$  nm, which is typical of a commercially available AFM tip size (<https://afmprobes.asylumresearch.com/probes/biospheretm.html>). This tip size is also much smaller than the radius of the cell, and large enough to compress several pores at once. The average size of pores in *E. coli* CW is 5 nm [102]. This selection of tip size should be optimal for probing the elasticity of the homogenized cell envelope at shallow indentation depths.

The CW of a gram-negative bacteria is located within the periplasm, which is a concentrated gel-like substance that is sandwiched between an inner and an outer membrane. This entire assembly is called the cell envelope, and it is represented by a linear thermoelastic solid in the FEM. It is well known that the cell envelope of a bacterial cell has porous and viscoelastic properties, but on short time scales, these nonlinear effects can be minimized [103]. The assigned cell envelope material property relates the stress and strain of the material in a linear fashion. In summation notation, the inverse Hooke's law for a linear thermoelastic material takes the form

$$\varepsilon_{ij} = \frac{1 + \nu}{E} \sigma_{ij} - \frac{\nu}{E} \sigma_{kk} \delta_{ij} + \alpha \Delta T \delta_{ij} \quad (4.1)$$

where  $\sigma$  is the stress,  $\varepsilon$  is the strain,  $E$  is the Young's modulus,  $\nu$  is the Poisson's ratio,  $\alpha = 0.01$  is the thermal expansion coefficient,  $\Delta T$  is the temperature change, and  $\delta$  is the Kronecker delta.

The simulation is executed in two consecutive steps. In the first step, a constant temperature drop is applied through the entire thickness of the cell envelope,  $\Delta T$ . Through thermal contraction, this temperature difference causes the cell envelope to shrink and become stressed in compression. The stress in the cell envelope causes the internal hydrostatic pressure of the fluid cavity,  $p$ , to increase. The cell envelope will shrink a different amount depending on the initial thickness  $t$  of the cell envelope and compressibility of the cell envelope material, which depends on the Poisson's ratio,  $\nu$ . The displacement of the exterior surface of the cell due to the thermal contraction in this step of the simulation can be calculated analytically. Details can be found in the Appendix. The final result for the radial displacement ( $u$ ) of the exterior surface of a fluid-filled thermoelastic sphere is

$$u = (1 + \nu) \alpha \Delta T \left( \frac{4\nu - 2}{(R_c + t)^3} + \frac{-1 - \nu}{R_c^3} \right)^{-1} \left( \frac{-(R_c + t)}{R_c^3} + \frac{1}{(R_c + t)^2} \right). \quad (4.2)$$

The final result for the displacement of the exterior surface of a fluid-filled thermoelastic cylinder is

$$u = (1 + \nu) \alpha \Delta T \left( \frac{2\nu - 1}{(R_c + t)^2} - \frac{1}{R_c^2} \right)^{-1} \left( \frac{-(R_c + t)}{R_c^2} + \frac{1}{(R_c + t)} \right). \quad (4.3)$$

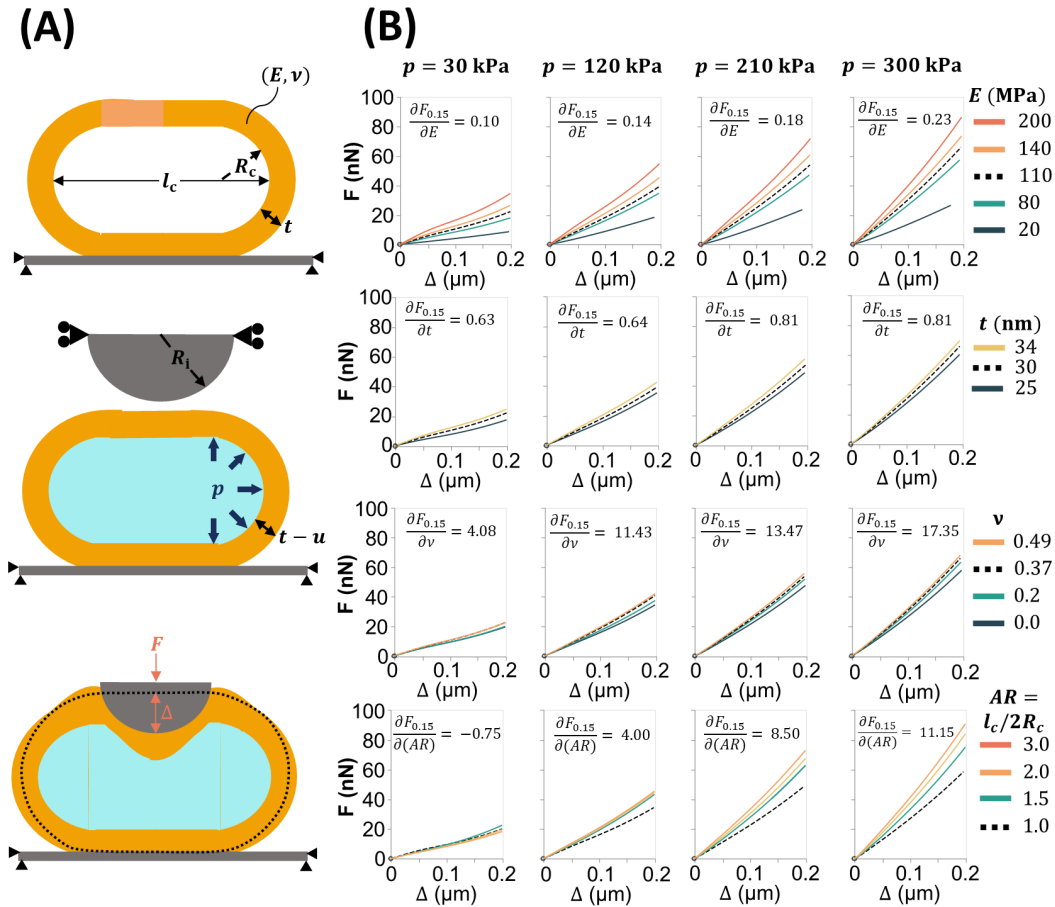


Figure 4.2: (A) Schematic view of the FEM used to simulate an isolated bacterium under indentation from a spherical tip of an AFM cantilever. The AFM tip is modeled using rigid elements with a radius  $R_i = 62.5 \text{ nm}$ . In the simulation, the AFM tip can only move vertically. To represent turgor pressure in the cytoplasm, the interior of the cell is filled with an incompressible fluid which is pressurized to  $p$ . The radius of the of the cytoplasm is  $R_c = 1 \mu\text{m}$ . The initial thickness of the material surrounding the cell is  $t$ . The cell sits atop a flat, rigid plate which is fixed in place. The simulation is controlled through displacement increments,  $\Delta$ , applied to the spherical AFM tip. (B) Results of sensitivity study. Each column contains simulated force-indentation depth curves with a the same turgor pressure,  $p$ . Each simulation within a column will have a different applied temperature difference  $\Delta T$  to achieve a consistent final turgor pressure  $p$ . From top to bottom, the rows contain simulated force-indentation depth curves with varying CW elastic modulus ( $E$ ), initial CW thickness ( $t$ ), CW Poisson ratio ( $\nu$ ), and cell geometric aspect ratio ( $AR = l_c/2R_c$ ). The sensitivity of the overall force measurement at an indentation depth of  $0.15 \mu\text{m}$  to the varying parameter is printed at the top of each plot.

The above equations are solved numerically for the initial cell envelope thickness,  $t$ , required to result in the final desired cell envelope thickness,  $t - u$ .

A balance of forces and Hooke's law (Equation 2.1) can be used to approximate the turgor pressure in a simulation from the applied temperature difference  $\Delta T$ . If the thermal strain is the only mechanical strain on the material, then Hooke's law for a linear thermoelastic material can be reduced to

$$\sigma = -\alpha\Delta T \frac{E}{1 - \nu^2}. \quad (4.4)$$

In a pressurized thin-walled spherical shell, stress can be related to internal pressure through a force balance so that

$$\sigma = \frac{pR_c}{2t} \quad (4.5)$$

Combining the two above equations, we can solve for the pressure  $p$  given a temperature difference  $\Delta T$ ,

$$p = -\frac{2tE\alpha\Delta T}{R_c(1 - \nu^2)}. \quad (4.6)$$

Due to the nonlinear change in the thickness of the shell  $t$  with each increment of the simulation, this equation is an approximation that systematically overestimates the turgor pressure. Therefore, this equation can be thought of as a close approximation and an upper bound to the turgor pressure in a given simulation.

In the second step of the simulation, the AFM tip is lowered to indent the cell. The indentation is controlled through displacement increments,  $\Delta$ , which are applied to the AFM tip. The reaction force,  $F$ , exerted on the AFM tip after contact is recorded. Contact between all surfaces is modeled using a hard contact pressure-overclosure relationship for motions normal to the surfaces, and all relative sliding motion between the two contacting surfaces is prevented. Once the two surfaces have begun contact, no separation is allowed. This formulation avoids instabilities in the simulation from the cell sliding between the AFM tip and the plate. For more details on the FEM, see Figures 4.4 and 4.5 in the Appendix.

A sensitivity study was carried out to determine the influence that each model parameter had on the measured reaction force in the simulated indentation. One at a time, parameters were varied while holding all other parameters at a selected baseline value. The sensitivities are printed in each plot in Figure 4.2, and simulations using selected baseline values are plotted with a black dotted line. No baseline value was selected for turgor pressure because it had the largest effect on the resulting force required to deform the cell. Instead, sensitivity coefficients were calculated

Table 4.1: Ranges of model parameters.

Parameter	Selected Value	Range	Reference	% of total Var[ $F_{0.15}$ ]
$p$	variable	30-300 kPa	[2]	46.6
$E$	110 MPa	20-200 MPa	[102]	43.5
$l_c/2R_c$	1.0	1.0-3.0	[104]	6.8
$t$	30 nm	25-35 nm	[101]	2.2
$\nu$	0.37	0.00-0.49	[102]	<1

for several values of the turgor pressure,  $p$ , and then averaged to determine the final sensitivity coefficient for each parameter. The metric used to determine the performance of a particular set of parameters is the force applied to achieve an indentation depth of 0.15  $\mu\text{m}$ ,  $F_{0.15}$ . If all parameters  $P$  are independent of each other, and second-order terms are ignored, we can write an expression for the variance of  $F_{0.15}$ :

$$\text{Var}[F_{0.15}] = \sum_i \left[ \frac{\partial F_{0.15}}{\partial P_i} \right]^2 \text{Var}[P_i], \quad (4.7)$$

where  $\frac{\partial F_{0.15}}{\partial P_i}$  is the sensitivity coefficient, approximated using a finite difference method

$$\frac{\partial F_{0.15}}{\partial P_i} = \frac{F_{0.15}(P_i = P_{iH}) - F_{0.15}(P_i = P_{iL})}{P_{iH} - P_{iL}}, \quad (4.8)$$

where  $P_{iH}$  is the upper limit, and  $P_{iL}$  is the lower limit of the range for parameter  $P_i$ . If the low and high limits of the ranges from literature reported in Table 4.1 are thought of as approximately a 5-95 percentile range for a normally distributed variable, then we can approximate the variance of each parameter,

$$\text{Var}[P_i] = \left[ \frac{P_{iH} - P_{iL}}{3.3} \right]^2. \quad (4.9)$$

Contributions to the variance of the indentation force from each variable are presented in Table 4.1. Using this formulation, turgor pressure and CW elastic modulus are the source of most of the total parameter error variance (46.6% and 43.5%, respectively).

Hence, reducing uncertainty in the aspect ratio, thickness of the cell envelope, or compressibility of the cell envelope would have a modest or negligible impact on the accuracy of the model. Therefore, in the subsequent inverse analysis we focus solely on the turgor pressure and elastic modulus of the cell envelope. We also use simulations with an aspect ratio of  $l_c/2R_c = 1.0$  even though this is the parameter with the third highest contribution to the total variance. The use of an aspect ratio of 1 allows us to use axisymmetric elements, which saves computation time.

### 4.3 Results and Discussion

Inverse analysis using a FEM is common practice for extracting material properties from indentation experiments. Others have pointed out that implementing this method blindly in cells with porous walls compressed between two parallel plates can result in erroneous approximations due to non-unique solutions [105]. They conducted a parametric study using parameters representative of *Saccharomyces cerevisiae* (commonly known as yeast). Here we perform a parametric study and explore the inverse analysis solution space using parameters representative of *Escherichia coli*, a gram-negative bacteria.

The inverse analysis implemented in this section consists of four steps:

1. Determine the domain or ranges of structural parameters. This requires an extensive review of the literature to include any reported values of the parameters to be quantified in the inverse analysis. The values we used are presented in Table 4.1.
2. Mesh the parameter space of possible structural parameter values using triangular (or tetrahedral, for three parameters) elements and run simulations at each mesh node. Examples of this meshed parameter space for two parameters is presented in Figure 4.3A-C.
3. Select an objective function and evaluate it at each node in the meshed parameter space. This step requires an experimental data set to compare to simulation data. As a first test of our method, we substitute experimental data with a simulation with a known set of parameters. We call this simulation the "simulated experiment."
4. Search for a node (which represents a simulation) that minimizes the objective function. The color contour on the mesh in Figure 4.3A-C represents the magnitude of the objective function evaluated at each node for three different objective functions.

The goal of the inverse analysis process is to take an experimental measurement of a force-indentation curve and perform a fitting to solve for the parameters of interest (in this case, the elastic modulus of the cell envelope and the internal turgor pressure). This fitting operation requires a metric to measure which set of parameters are the "best" fit. That metric is also known as an objective function. Three different objective functions are investigated here.

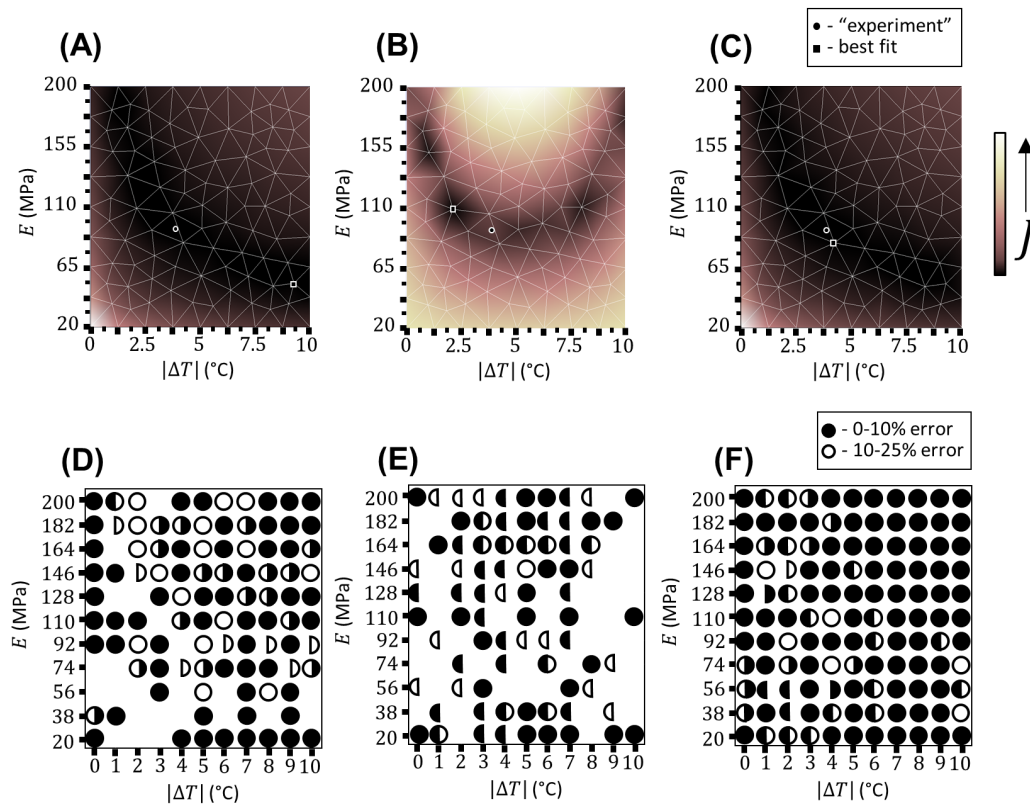


Figure 4.3: (A) Meshed parameter space with color contour representing the magnitude of the RSS objective function. (B) Meshed parameter space with color contour representing the magnitude of the error in cubic coefficients objective function. (C) Meshed parameter space with color contour representing the magnitude of the combined RSS and error in cubic coefficients objective function. Each node in the mesh of (A)-(C) represents a simulation. (D) Convergence of simulations in full possible parameter space using RSS objective function. (E) Convergence of simulations in full possible parameter space using error in cubic coefficients objective function. (F) Convergence of simulations in full possible parameter space using combined RSS and error in cubic coefficients objective function. Each point in the plots (D)-(F) represents a simulated experiment. A filled circle represents an analysis that converged within 0-10% of the true values provided in the simulated experiment. An open circle represents an analysis that converged within 10-25% of the true values provided in the simulated experiment. The left half of the circle represents the elastic modulus of the cell envelope and the right half of the circle represents the turgor pressure (change in temperature applied to the cell envelope).

The first is a residual sum of squares (RSS) objective function, which is the standard minimization function in regression analyses. Mathematically, this objective function can be expressed as

$$J_{\text{RSS}} = \sum_{i=1}^N (F_{i,\text{sim}} - F_{i,\text{exp}})^2, \quad (4.10)$$

where  $J_{\text{RSS}}$  is the objective function that we wish to minimize,  $F_{i,\text{sim}}$  is the simulated force measurement at an incremental indentation depth  $\Delta_i$ ,  $F_{i,\text{exp}}$  is experimental force measurement at the same incremental indentation depth  $\Delta_i$ , and  $N$  is the number of incremental force measurements. The color contour in Figure 4.3A represents the magnitude of this objective function evaluated for a simulated experimental data set with known parameters  $E = 92$  kPa and  $\Delta T = -4.0$ , which translates to a turgor pressure of  $p = 339$  kPa.

The second objective function that we tested is a measure of the change in curvature of fitted polynomials to the force-indentation depth curves. We selected this objective function because we observed that the curvatures of the force-displacement data were different at low turgor pressures than high turgor pressures in the sensitivity study data. To construct this objective function, first each data set (simulation and experiment) must be fit to a third order polynomial through a least squares regression so that

$$F(\Delta) = a + b\Delta + c\Delta^2 + d\Delta^3, \quad (4.11)$$

where the variables  $a$ ,  $b$ ,  $c$ , and  $d$  are the coefficients of the fitted polynomial. The coefficient  $d$  is related to the change in curvature of the fitted polynomial through a series expansion. For example, the third-order Maclaurin series expansion is

$$F(\Delta) = F(0) + F'(0)\Delta + \frac{1}{2!}F''(0)\Delta^2 + \frac{1}{3!}F'''(0)\Delta^3 + O(\Delta^4). \quad (4.12)$$

Hence, coefficient  $d$  is identified as the third derivative of  $F$  computed at  $\Delta = 0$ . The objective function we selected is the percent difference between the third order coefficient  $d$  for fitted polynomials to the simulation and experimental data. Mathematically, this objective function can be expressed as

$$J_{\text{d,error}} = \frac{|d_{\text{sim}} - d_{\text{exp}}|}{d_{\text{exp}}} \quad (4.13)$$

where  $J_{\text{d,error}}$  is the objective function that we wish to minimize,  $d_{\text{sim}}$  is the third-order coefficient fit to simulation data and  $d_{\text{exp}}$  is the third-order coefficient fit to experimental data. The color contour in Figure 4.3B represents the magnitude of

this objective function evaluated for a simulated experimental data set with the same known parameters as in Figure 4.3A.

The final objective function that we tested is a weighted average of the other two objective functions, with the error in third-order fitted coefficients weighted highest,

$$J_{ave} = 0.75 * J_{d,error} + 0.25 * J_{SOLS}. \quad (4.14)$$

These weights were selected through trial and error. Because the scales of the two objective functions  $J_{d,error}$  and  $J_{SOLS}$  are not the same, the weights multiplied to each of the separate objective functions do not represent the contributions of each one to the combined function  $J_{ave}$ . The color contour in Figure 4.3C represents the magnitude of this objective function evaluated for a simulated experimental data set with the same known parameters as in Figures 4.3A and B.

To further investigate the accuracy of each objective function across a range of true values, we selected 121 simulations evenly spaced through the parameters space to act as simulated experiments and repeated the inverse analysis on each one. Each point in the plots of Figures 4.3C-F represents one such simulation that converged to within 25% of the true parameter values. Simulations that did not converge to within 25% of the true parameter values are represented by blank spaces. One interesting observation is that the correlations visible between  $E$  and  $\Delta T$  in Figures 4.3A-C are again represented, although less clearly, in Figures 4.3D-F. It is also interesting to note that the RSS objective function resulted in better approximations for  $\Delta T$  (turgor pressure), while the error in third order polynomial coefficients resulted in better approximations for the Young's modulus,  $E$ . The combined objective function produced the most accurate results, resulting in no blank spaces in Figure 4.3F.

If we take a closer look at the correlations for each of the objective functions, we can see that in the case of the RSS objective, there is a semi-linear correlation between the elastic modulus of the cell envelope,  $E$ , and the turgor pressure (represented by  $\Delta T$ ). This correlation makes sense, as cells with a high internal turgor pressure and low elastic cell envelope modulus will respond similarly to indentation as a cell with low internal turgor pressure and high elastic cell envelope modulus. This phenomenon is similar to the way an inflated party balloon may feel almost as stiff as an uninflated bicycle tire when poked with a finger. Even though the bending rigidity of the thin latex of a party balloon is much less than that of a thick rubber bicycle tire, the internal pressure can provide an apparent overall stiffness to the balloon that makes its indentation modulus similar to that of the uninflated tire.

There is no apparent physical explanation for the shape of the correlation between  $E$  and  $\Delta T$  using the error in fitted cubic polynomial coefficients. For an unknown reason, the change in curvature of the force-indentation depth curves is similar for cells with high elastic modulus of the cell envelope and either low or high turgor pressures. Combining information from both of these objective functions led to the third objective function with a minimized objective function very close to the true parameter values in almost all cases. The combined objective function, when compared to the RSS objective function alone, resulted in a reduction in error from an average of 21% to 4.9% for CW elastic modulus and a reduction in error from an average of 18% to 7.5% for turgor pressure. When compared to the error in cubic coefficients objective function alone, the combined objective function reduced errors from an average of 25% to 4.9% for CW elastic modulus and from an average of 100% to 7.5% for turgor pressure.

#### 4.4 Conclusions

The observed correlations between turgor pressure and CW elastic modulus demonstrate the non-unique set of solutions that are possible from fitting AFM force spectra on microbes to a FEM. The two parameters can be separated from a single AFM force spectra by using metrics that account for changing magnitudes and changing curvatures of the force spectra with changing turgor pressure and CW elasticity. Here we present one such possibility and demonstrate a reduction in error by 20% for CW elastic modulus and 11% for turgor pressure when compared to the standard least squares regression function.

There are many opportunities to refine and improve the method presented here. For example, after a node which minimizes the objective function is located, the mesh can be refined in the area of the minimal node, and more simulations can be run at each refined mesh node to increase the precision of the estimated parameters. Incorporating the true aspect ratio of the cell would also decrease variability in the resulting parameter estimations by about 6% according to the sensitivity study conducted here.

Additional information in the form of indentation using different size or shaped indenters or exerting different types of load on the cells could allow for estimation of even more parameters with unique solutions. One such parameter is the contribution to stiffness of the cytoskeletal filaments. There is recent and growing evidence that the filaments of the cytoskeleton contribute to the mechanical response of a cell in

compression [54, 92]. Including experiments from a spherical and a conical AFM tip, for example, may provide enough information for a similar inverse analysis as presented here to extract the bulk modulus of the cytoplasmic fluid in addition to CW elastic modulus and turgor pressure.

## Appendix

### FEM Definition

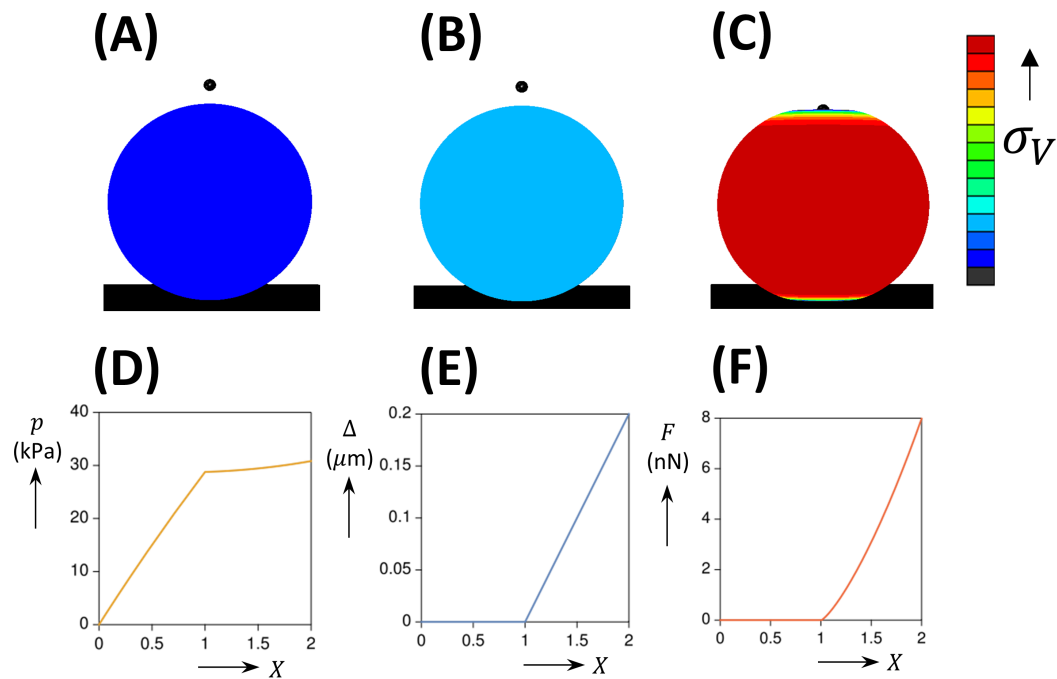


Figure 4.4: (A) Undeformed configuration of a spherically-shaped cell under indentation from a rigid spherical indenter.  $X = 0$  in simulation time. (B) Spherical cell under uniform tension from building turgor pressure.  $X = 1$  in simulation time. (C) Final deformed configuration of spherical cell after indentation from rigid spherical indenter.  $X = 2$  in simulation time. Colors represent von Mises stress. (D) Evolution of pressure over simulation time. Turgor pressure is built to the nominal value (in this example, 30 kPa) during the thermal contraction step between  $X = 0$  and  $X = 1$ . Pressure continues to build during indentation due to the constant volume constraint. (E) Indentation depth over simulation time. The simulation is displacement-controlled, so this is a linear function of time during the indentation step. (F) Evolution of contact force over simulation time.

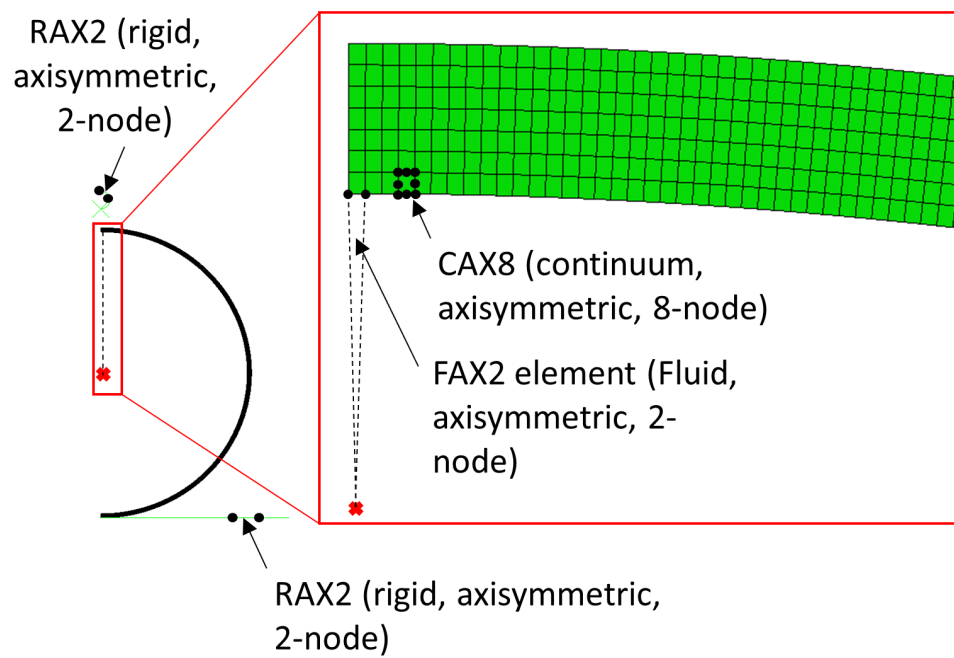


Figure 4.5: Element types used in construction of Abaqus FEM.

### Displacement of Spherical Cell Envelope Due to Thermal Contraction

Consider a sphere made of a linear thermoelastic material with known mechanical properties  $E$ , the Young's modulus,  $\nu$ , Poisson's ratio, and  $\alpha$ , the coefficient of thermal expansion. The sphere has a hole in the center of radius  $R_c$  which is filled with an incompressible fluid that cannot escape the sphere. The thickness of the material surrounding the hole is  $t$ , so the radius of the full sphere is  $R_c + t$ . A temperature difference  $\Delta T$  is applied uniformly to the material surrounding the incompressible fluid.

Due to the symmetries in this problem, we know that shear stresses will all be equal to zero, and the two tangential stress components will be equal ( $\sigma_\theta = \sigma_\phi$ ). Stress will only vary in the radial direction. Relabeling  $\sigma_t = \sigma_\theta = \sigma_\phi$ , equilibrium in the radial direction of an element reduces to

$$\frac{\partial \sigma_r}{\partial r} + \frac{2}{r}(\sigma_r - \sigma_t) = 0. \quad (4.15)$$

Equilibrium in other directions is trivial. As in the case of the stresses, there will only be three nonzero components of strain, and the two tangential components ( $\varepsilon_\theta$  and  $\varepsilon_\phi$ ) are equal. Also note that the material can only displace in the radial direction,  $u = u_r$ . Relabelling  $\varepsilon_t = \varepsilon_\theta = \varepsilon_\phi$ , the kinematic equations reduce to

$$\varepsilon_r = \frac{du}{dr}, \quad \varepsilon_t = \frac{u}{r}. \quad (4.16)$$

Finally, the constitutive equations for the homogeneous and isotropic body reduce to

$$\varepsilon_r = \frac{1}{E}(\sigma_r - 2\nu\sigma_t) + \alpha\Delta T, \quad \varepsilon_t = \frac{1}{E}[\sigma_t - \nu(\sigma_t + \sigma_r)] + \alpha\Delta T. \quad (4.17)$$

We can solve the above constitutive equations for the two stress components in terms of the strains

$$\sigma_r = \frac{E}{(1+\nu)(1-2\nu)} [(1-\nu)\varepsilon_r + 2\nu\varepsilon_t - (1+\nu)\alpha\Delta T] \quad (4.18)$$

$$\sigma_t = \frac{E}{(1+\nu)(1-2\nu)} [\varepsilon_t + \nu\varepsilon_r - (1+\nu)\alpha\Delta T]. \quad (4.19)$$

Substituting Equations 4.18 and 4.19 in Equation 4.15, then replacing  $\varepsilon_r$  and  $\varepsilon_t$  by the kinematic Equation 4.16, we find an ordinary differential equation for  $u$

$$\frac{d^2u}{dr^2} + \frac{2}{r} \frac{du}{dr} - \frac{2u}{r^2} = \frac{1+\nu}{1-\nu} \alpha \frac{dT}{dr}, \quad (4.20)$$

which can be rewritten in a more convenient form to integrate

$$\frac{d}{dr} \left[ \frac{1}{r^2} \frac{d}{dr} (r^2 u) \right] = \frac{1+\nu}{1-\nu} \alpha \frac{dT}{dr}. \quad (4.21)$$

Finally, because the applied temperature difference is constant through the thickness of the material, the right-hand side of the above equation is zero.

$$\frac{d}{dr} \left[ \frac{1}{r^2} \frac{d}{dr} (r^2 u) \right] = 0 \quad (4.22)$$

The solution of this ordinary differential equation is

$$u(r) = C_1 r + \frac{C_2}{r^2}. \quad (4.23)$$

Because the fluid-filled cavity is incompressible, the interior surface of the surrounding material cannot move in the radial direction, so  $u(r = R_c) = 0$ . Applying this boundary condition to the above equation, we can solve for one of the constants of integration

$$u(r = R_c) = C_1 R_c + \frac{C_2}{R_c^2} = 0 \quad (4.24)$$

$$u(r) = \frac{C_2}{r^2} - \frac{C_2}{R_c^3} r \quad (4.25)$$

At the exterior surface, we have a traction-free boundary condition because there are no external forces on the material. In our case, this means that the radial stress at the exterior surface is equal to zero,  $\sigma_r(r = R_c + t) = 0$ . To apply the exterior boundary condition, we must first find  $\sigma_r$  in terms of the displacement  $u$

$$\begin{aligned} \sigma_r &= \frac{E}{(1+\nu)(1-2\nu)} [(1-\nu)\varepsilon_r + 2\nu\varepsilon_t - (1+\nu)\alpha\Delta T] \\ &= \frac{E}{(1+\nu)(1-2\nu)} \left[ (1-\nu) \frac{du}{dr} + 2\nu \frac{u}{r} - (1+\nu)\alpha\Delta T \right] \\ &= \frac{E}{(1+\nu)(1-2\nu)} \left[ (1-\nu) \left( \frac{-2C_2}{r^3} - \frac{C_2}{R_c^3} \right) + 2\nu \left( \frac{C_2}{r^3} - \frac{C_2}{R_c^3} \right) - (1+\nu)\alpha\Delta T \right]. \end{aligned}$$

Applying the boundary condition and solving for  $C_2$ ,

$$\begin{aligned} \sigma_r(r = R_c + t) = 0 &= \frac{E}{(1+\nu)(1-2\nu)} \left[ (1-\nu) \left( \frac{-2C_2}{(R_c+t)^3} - \frac{C_2}{R_c^3} \right) + 2\nu \left( \frac{C_2}{(R_c+t)^3} - \frac{C_2}{R_c^3} \right) - (1+\nu)\alpha\Delta T \right] \\ &= C_2 \left( \frac{4\nu-2}{(R_c+t)^3} + \frac{-1-\nu}{R_c^3} \right) - (1+\nu)\alpha\Delta T \\ C_2 &= (1+\nu)\alpha\Delta T \left( \frac{4\nu-2}{(R_c+t)^3} + \frac{-1-\nu}{R_c^3} \right)^{-1}. \end{aligned}$$

Finally, we can write the expression for the radial displacement of the sphere at the exterior surface

$$u(r = R_c + t) = (1 + \nu)\alpha\Delta T \left( \frac{4\nu - 2}{(R_c + t)^3} + \frac{-1 - \nu}{R_c^3} \right)^{-1} \left( \frac{-(R_c + t)}{R_c^3} + \frac{1}{(R_c + t)^2} \right).$$

### Displacement of Cylindrical Cell Envelope Due to Thermal Contraction

Consider a cylinder made of a linear thermoelastic material with known mechanical properties  $E$ , the Young's modulus,  $\nu$ , Poisson's ratio, and  $\alpha$ , the coefficient of thermal expansion. The cylinder has a concentric hole of radius  $R_c$  which is filled with an incompressible fluid that cannot escape the sphere. The thickness of the material surrounding the hole is  $t$ , so the radius of the full sphere is  $R_c + t$ . A temperature difference  $\Delta T$  is applied uniformly to the material surrounding the incompressible fluid.

Again, due to the symmetries in this problem, we know that the shear stresses will all be zero. Therefore, equilibrium in the radial direction of an element reduces to

$$\frac{d\sigma_r}{dr} + \frac{\sigma_r - \sigma_t}{r} = 0. \quad (4.26)$$

Equilibrium in the other directions is trivial. There will only be three nonzero components of strain. Also note that the material can only displace in the radial direction. Therefore, the kinematic equations reduce to

$$\varepsilon_r = \frac{du_r}{dr} \quad (4.27)$$

$$\varepsilon_t = \frac{u_r}{r} \quad (4.28)$$

$$\varepsilon_z = \frac{\partial u_z}{\partial z}. \quad (4.29)$$

Finally, the stress-strain relationships reduce to

$$\varepsilon_r = \frac{1}{E} [\sigma_r - \nu(\sigma_t + \sigma_z)] + \alpha T, \quad \varepsilon_t = \frac{1}{E} [\sigma_t - \nu(\sigma_z + \sigma_r)] + \alpha T, \quad \varepsilon_z = \frac{1}{E} [\sigma_z - \nu(\sigma_r + \sigma_t)] + \alpha T. \quad (4.30)$$

Assuming that the cylinder is in a plane strain condition,  $\varepsilon_z = 0$ , and the third of Equations 4.30 gives

$$\sigma_z = \nu(\sigma_r + \sigma_t) - \alpha ET. \quad (4.31)$$

Substituting this into the other two Eqs (2.30) gives

$$\epsilon_r - (1 + \nu)\alpha T = \frac{1 - \nu^2}{E} \left( \sigma_r - \frac{\nu}{1 - \nu} \sigma_t \right) \quad (4.32)$$

$$\epsilon_t - (1 + \nu)\alpha T = \frac{1 - \nu^2}{E} \left( \sigma_t - \frac{\nu}{1 - \nu} \sigma_r \right). \quad (4.33)$$

Solving Equations 4.32 and 4.33 for the stresses

$$\sigma_r = \frac{E}{(1 + \nu)(1 - 2\nu)} [\nu\epsilon_t + (1 - \nu)\epsilon_r - (1 + \nu)\alpha T] \quad (4.34)$$

$$\sigma_t = \frac{E}{(1 + \nu)(1 - 2\nu)} [\nu\epsilon_r + (1 - \nu)\epsilon_t - (1 + \nu)\alpha T]. \quad (4.35)$$

Substituting Equations 4.34 and 4.35 in 4.26, then replacing  $\epsilon_r, \epsilon_t$  by the values given in Equation 4.30, we find the differential equation for  $u$

$$\frac{d^2 u_r}{dr^2} + \frac{1}{r} \frac{du_r}{dr} - \frac{1}{r^2} u_r = \frac{1 + \nu}{1 - \nu} \alpha \frac{dT}{dr}, \quad (4.36)$$

which can be written

$$\frac{d}{dr} \left[ \frac{1}{r} \frac{d}{dr} (r u_r) \right] = \frac{1 + \nu}{1 - \nu} \alpha \frac{dT}{dr}. \quad (4.37)$$

Since the temperature is constant, we can set the right-hand side of Equation (2.37) to zero. Then, the solution of the differential equation is

$$u_r(r) = C_1 r + \frac{C_2}{r}. \quad (4.38)$$

The boundary condition at the interior surface implies that the  $u_r(r = R) = 0$ . Applying this to the above equation,

$$u_r(R) = C_1 R + \frac{C_2}{R} = 0 \quad (4.39)$$

$$u_r(r) = \frac{C_2}{r} - \frac{C_2}{R^2} r. \quad (4.40)$$

The traction-free boundary condition at the exterior surface implies that  $\sigma_r(r = R + t) = 0$ . First, let's find  $\sigma_r$  in terms of the displacement  $u(r)$

$$\begin{aligned}\sigma_r &= \frac{E}{(1 + \nu)(1 - 2\nu)} [\nu\epsilon_t + (1 - \nu)\epsilon_r - (1 + \nu)\alpha T] \\ &= \frac{E}{(1 + \nu)(1 - 2\nu)} \left[ \nu \frac{u_r}{r} + (1 - \nu) \frac{\partial u_r}{\partial r} - (1 + \nu)\alpha T \right] \\ &= \frac{E}{(1 + \nu)(1 - 2\nu)} \left[ \nu \left( \frac{C_2}{r^2} - \frac{C_2}{R^2} \right) + (1 - \nu) \left( \frac{-C_2}{r^2} - \frac{C_2}{R^2} \right) - (1 + \nu)\alpha T \right].\end{aligned}$$

Now apply the boundary condition and solve for  $C_2$

$$\begin{aligned}\sigma_r(r = R + t) = 0 &= \frac{E}{(1 + \nu)(1 - 2\nu)} \left[ \nu \left( \frac{C_2}{(R + t)^2} - \frac{C_2}{R^2} \right) + (1 - \nu) \left( \frac{-C_2}{(R + t)^2} - \frac{C_2}{R^2} \right) - (1 + \nu)\alpha T \right] \\ &= C_2 \left( \frac{2\nu - 1}{(R + t)^2} - \frac{1}{R^2} \right) - (1 + \nu)\alpha T \\ C_2 &= (1 + \nu)\alpha T \left( \frac{2\nu - 1}{(R + t)^2} - \frac{1}{R^2} \right)^{-1}.\end{aligned}$$

Finally, we can plug the constant into Equation 4.40 and solve for the radial displacement of the sphere at the exterior surface

$$u(r = R + t) = (1 + \nu)\alpha T \left( \frac{2\nu - 1}{(R + t)^2} - \frac{1}{R^2} \right)^{-1} \left( \frac{-(R + t)}{R^2} + \frac{1}{(R + t)} \right). \quad (4.41)$$

## References

- [2] D. S. Cayley, H. J. Guttman, and M. T. Record. “Biophysical characterization of changes in amounts and activity of *Escherichia coli* cell and compartment water and turgor pressure in response to osmotic stress”. In: *Biophysical Journal* 78.4 (Apr. 2000), pp. 1748–1764. ISSN: 0006-3495. DOI: 10.1016/S0006-3495(00)76726-9.
- [8] E. Steudle. “Pressure probe techniques: basic principles and application to studies of water and solute relations at the cell, tissue and organ level”. In: *Water deficits* (1993), pp. 5–36. URL: <https://docuserve.library.caltech.edu/illiad/illiad.dll?Action=10&Form=75&Value=531985> (visited on 02/05/2021).
- [9] A. Deri Tomos and Roger A. Leigh. “THE PRESSURE PROBE: A Versatile Tool in Plant Cell Physiology”. In: *Annual Review of Plant Physiology and Plant Molecular Biology* 50.1 (1999), pp. 447–472. DOI: 10.1146/annurev.arplant.50.1.447. URL: <https://doi.org/10.1146/annurev.arplant.50.1.447> (visited on 02/04/2021).
- [10] Roger R. Lew. “How does a hypha grow? The biophysics of pressurized growth in fungi”. In: *Nature Reviews Microbiology* 9.7 (July 2011). Number: 7 Publisher: Nature Publishing Group, pp. 509–518. ISSN: 1740-1534. DOI: 10.1038/nrmicro2591. URL: <https://www.nature.com/articles/nrmicro2591> (visited on 02/04/2021).
- [11] Anthony Edward Walsby. “The pressure relationships of gas vacuoles”. In: *Proceedings of the Royal Society of London. Series B. Biological Sciences* 178.1052 (Aug. 3, 1971), pp. 301–326. ISSN: 0080-4649, 2053-9193. DOI: 10.1098/rspb.1971.0067. URL: <https://royalsocietypublishing.org/doi/10.1098/rspb.1971.0067> (visited on 02/04/2021).
- [13] M. Arnoldi et al. “Bacterial turgor pressure can be measured by atomic force microscopy”. In: *Physical Review. E, Statistical Physics, Plasmas, Fluids, and Related Interdisciplinary Topics* 62.1 (July 2000), pp. 1034–1044. ISSN: 1063-651X. DOI: 10.1103/physreve.62.1034.
- [14] Dominic Vella et al. “The indentation of pressurized elastic shells: from polymeric capsules to yeast cells”. In: *Journal of The Royal Society Interface* 9.68 (Mar. 7, 2012), pp. 448–455. ISSN: 1742-5689, 1742-5662. DOI: 10.1098/rsif.2011.0352. URL: <https://royalsocietypublishing.org/doi/10.1098/rsif.2011.0352> (visited on 11/11/2019).
- [29] Yi Deng, Mingzhai Sun, and Joshua W. Shaevitz. “Direct Measurement of Cell Wall Stress Stiffening and Turgor Pressure in Live Bacterial Cells”. In: *Physical Review Letters* 107.15 (Oct. 6, 2011). Publisher: American Physical Society, p. 158101. DOI: 10.1103/PhysRevLett.107.158101. URL: <https://link.aps.org/doi/10.1103/PhysRevLett.107.158101> (visited on 02/07/2021).

- [38] Catherine Volle et al. “Measuring the Effect of Antimicrobial Peptides on the Biophysical Properties of Bacteria using Atomic Force Microscopy”. In: *Biophysical Journal* 114.3 (Feb. 2018), 354a. ISSN: 00063495. DOI: 10.1016/j.bpj.2017.11.1969. URL: <https://linkinghub.elsevier.com/retrieve/pii/S0006349517332010> (visited on 02/16/2021).
- [42] H. Hertz. “Über die Berührung fester elastischer Körper (On the contact of elastic solids)”. In: *Journal für die reine und angewandte Mathematik* 82 (1882), pp. 156–171.
- [45] Eric Reissner. “Stresses and Small Displacements of Shallow Spherical Shells. I”. In: *Journal of Mathematics and Physics* 25.1 (Apr. 1946), pp. 80–85. ISSN: 00971421. DOI: 10.1002/sapm194625180. URL: <http://doi.wiley.com/10.1002/sapm194625180> (visited on 11/06/2019).
- [46] A Pogorelov. *Bendings of Surfaces and Stability of Shells*. Vol. 72. Translations of Mathematical Monographs. Providence, Rhode Island: American Mathematical Society, 1988. ISBN: 978-0-8218-4525-7 978-1-4704-4486-0. DOI: 10.1090/mmono/072. URL: <http://www.ams.org/mmono/072> (visited on 02/03/2021).
- [54] Pauline Durand-Smet et al. “A Comparative Mechanical Analysis of Plant and Animal Cells Reveals Convergence across Kingdoms”. In: *Biophysical Journal* 107.10 (2014), pp. 2237–2244. ISSN: 0006-3495. DOI: <https://doi.org/10.1016/j.bpj.2014.10.023>. URL: <http://www.sciencedirect.com/science/article/pii/S0006349514010741>.
- [92] Ovijit Chaudhuri, Sapun H. Parekh, and Daniel A. Fletcher. “Reversible stress softening of actin networks”. In: *Nature* 445.7125 (Jan. 2007), pp. 295–298. ISSN: 0028-0836, 1476-4687. DOI: 10.1038/nature05459. URL: <http://www.nature.com/articles/nature05459> (visited on 11/06/2019).
- [94] Enrique R Rojas and Kerwyn Casey Huang. “Regulation of microbial growth by turgor pressure”. In: *Current Opinion in Microbiology*. Cell Regulation 42 (Apr. 1, 2018), pp. 62–70. ISSN: 1369-5274. DOI: 10.1016/j.mib.2017.10.015. URL: <https://www.sciencedirect.com/science/article/pii/S1369527417300395> (visited on 02/04/2021).
- [95] David Alsteens et al. “Structure, cell wall elasticity and polysaccharide properties of living yeast cells, as probed by AFM”. In: *Nanotechnology* 19.38 (Sept. 24, 2008), p. 384005. ISSN: 0957-4484, 1361-6528. DOI: 10.1088/0957-4484/19/38/384005. URL: <https://iopscience.iop.org/article/10.1088/0957-4484/19/38/384005> (visited on 02/16/2021).
- [96] John W. Goss and Catherine B. Volle. “Using Atomic Force Microscopy To Illuminate the Biophysical Properties of Microbes”. In: *ACS Applied Bio Materials* 3.1 (Jan. 21, 2020), pp. 143–155. ISSN: 2576-6422, 2576-6422.

- DOI: 10.1021/acsabm.9b00973. URL: <https://pubs.acs.org/doi/10.1021/acsabm.9b00973> (visited on 02/16/2021).
- [97] Richard G. Bailey et al. “The Interplay between Cell Wall Mechanical Properties and the Cell Cycle in *Staphylococcus aureus*”. In: *Biophysical Journal* 107.11 (Dec. 2, 2014), pp. 2538–2545. ISSN: 0006-3495. DOI: 10.1016/j.bpj.2014.10.036. URL: <https://www.ncbi.nlm.nih.gov/pmc/articles/PMC4255174/> (visited on 02/05/2021).
- [98] Viggo Tvergaard and Alan Needleman. “Effect of Properties and Turgor Pressure on the Indentation Response of Plant Cells”. In: *Journal of Applied Mechanics* 85.6 (June 1, 2018). ISSN: 0021-8936. DOI: 10.1115/1.4039574. URL: <https://asmedigitalcollection.asme.org/appliedmechanics/article/85/6/061007/421999/Effect-of-Properties-and-Turgor-Pressure-on-the> (visited on 11/06/2019).
- [99] T. Nakamura, T. Wang, and S. Sampath. “Determination of properties of graded materials by inverse analysis and instrumented indentation”. In: *Acta Materialia* 48.17 (Nov. 2000), pp. 4293–4306. ISSN: 13596454. DOI: 10.1016/S1359-6454(00)00217-2. URL: <https://linkinghub.elsevier.com/retrieve/pii/S1359645400002172> (visited on 11/06/2019).
- [100] Michael Smith. *ABAQUS/Standard User’s Manual, Version 6.9*. English. United States: Dassault Systèmes Simulia Corp, 2018.
- [101] J. A. Hobot et al. “Periplasmic gel: new concept resulting from the reinvestigation of bacterial cell envelope ultrastructure by new methods.” In: *Journal of Bacteriology* 160.1 (Oct. 1, 1984), pp. 143–152. ISSN: 0021-9193, 1098-5530. URL: <https://jlb.asm.org/content/160/1/143> (visited on 02/08/2021).
- [102] James C. Gumbart et al. “*Escherichia coli* Peptidoglycan Structure and Mechanics as Predicted by Atomic-Scale Simulations”. In: *PLOS Computational Biology* 10.2 (Feb. 20, 2014). Publisher: Public Library of Science, e1003475. ISSN: 1553-7358. DOI: 10.1371/journal.pcbi.1003475. URL: <https://journals.plos.org/ploscompbiol/article?id=10.1371/journal.pcbi.1003475> (visited on 02/03/2021).
- [103] Virginia Vadillo-Rodríguez and John R. Dutcher. “Viscoelasticity of the bacterial cell envelope”. In: *Soft Matter* 7.9 (Apr. 18, 2011). Publisher: The Royal Society of Chemistry, pp. 4101–4110. ISSN: 1744-6848. DOI: 10.1039/C0SM01054E. URL: <https://pubs.rsc.org/en/content/articlelanding/2011/sm/c0sm01054e> (visited on 02/06/2021).
- [104] Nili Grossman, Eliora Z Ron, and Conrad L Woldringh. “Changes in Cell Dimensions During Amino Acid Starvation of *Escherichia coli*”. In: *J. BACTERIOL.* 152 (1982), p. 7.

- [105] A. E. Smith, K. E. Moxham, and A. P. J. Middelberg. “On uniquely determining cell–wall material properties with the compression experiment”. In: *Chemical Engineering Science* 53.23 (Dec. 1, 1998), pp. 3913–3922. ISSN: 0009-2509. DOI: 10.1016/S0009-2509(98)00198-5. URL: <http://www.sciencedirect.com/science/article/pii/S0009250998001985> (visited on 11/06/2019).

*Chapter 5*

## CONCLUSIONS AND OUTLOOK

This dissertation explored a variety of experimental and modeling approaches to decoupling the contributions of subcellular structures to the mechanical response of a walled cell. There is an increasing amount of indentation data on single cells available in the literature. Typically, the indentation data is interpreted using either one stiffness value or using a full continuum model. The former is easy to implement, but results in only one extracted mechanical stiffness from each indentation. The latter requires an expertise in solid mechanics or materials science to develop, but results in material properties that do not rely on the structure of the particular experiment. To bridge the gap between highly complex models and ease of analysis implementation, a new two-spring model was introduced in Chapter 2. Adding some complexity to the analysis, the same two-spring model was used in Chapter 3 with the addition of a Bayesian optimization to determine the magnitude of stiffness for each subcellular component. In Chapter 4, a finite-element model (FEM) of a cell under atomic-force microscopy (AFM) nano-indentation is examined in detail to determine if unique mechanical properties and the turgor pressure of a cell can be extracted from a single indentation measurement.

In Chapters 2 and 3, the relative stiffness contributions from the cell wall (CW) and cytoplasm in two types of cultured plant cell were decoupled through the use of a newly developed discrete two-spring model in conjunction with a newly designed multi-scale biomechanical assay. The magnitude of stiffness contributions was evaluated for two types of plant cells after exposing the cells to solutions of different osmolarities, drug treatments to affect the cytoskeleton, and during different stages of differentiation. These studies confirmed some ubiquitous hypotheses and results of many other plant cell mechanobiology researchers: turgor pressure dominates the response of a turgid cell in compression, turgor pressure stiffens the CW through stress, and the cytoskeleton plays a non-negligible role in resisting external mechanical loads.

More specifically, in transgenic xylem vessel elements of *Arabidopsis thaliana*, the mechanical contributions from the cytoplasm and CW were isolated at three stages of the differentiation process. The results provide experimental evidence that the

secondary cell wall (SCW) is stiffer than the relaxed primary cell wall (PCW), in a living cell system. This conclusion is reached by comparing measured cell stiffnesses across the stages of differentiation in hypertonic conditions, where the cell wall is effectively decoupled from the cytoplasm. In isotonic and hypotonic conditions, turgor pressure gives rise to an increased stress in the PCW, causing it to stiffen beyond the SCW. We also measure a quantifiable softening of the PCW in stage 1 in hypotonic conditions, as the cell prepares for deposition of the SCW. This is the first time a mechanical weakening is measured on the PCW before the SCW deposition in living cells. From measurements in isotonic and hypotonic conditions, evidence was also found of a quantifiable difference in cytoplasmic stiffness as a consequence of active bundling of the filaments in the cytoplasm, guided by differentiation. These findings provide insight into the mechanisms of xylem vessel element differentiation. They suggest that inter- and/or intra-cellular mechanical signals regulate cell differentiation and SCW deposition.

Experiments conducted on suspension-cultured *Nicotiana tabacum* cells in the multi-scale biomechanical assay showed evidence that the cytoskeleton contributes significantly to the stiffness and dissipated energy of cells in compression. Using a generative statistical model applied to the discrete two-spring model allows the decoupling of the relative stiffness contributions of the microtubules (MTs) and actin filaments (AFs) from the CW and the rest of the cytoplasm. The stiffness of the MTs and AFs was similar to those of all other isolated components in plasmolyzing solution. The highest stiffness contribution is from the cytoplasm, excluding contributions from MTs and AFs, in hypotonic conditions. This contribution is reduced by approximately four times in hypertonic conditions, which indicates that turgor pressure is the dominant resisting component to compression. Higher internal pressure stresses the CW and stiffens it. The stiffness of the CW in hypotonic conditions is estimated to be approximately twice as high as the stiffness of the CW in hypertonic conditions. This increase in stiffness in our experiment is confirmed by AFM nano-indentation measurements. These results are all in agreement with observations from current literature, but are derived from a different experimental technique and new model. In addition, the energy dissipation analysis indicated that the anisotropic orientation of the MTs causes the distribution of dissipated energies to be larger, and this effect is magnified when the more isotropically distributed AFs are removed. The MTs and AFs of the cytoskeleton have long been known to play a pivotal role in cell morphogenesis, but recently have been studied for their possible additional role in mechano-sensing and mechano-transduction within a cell. The

results presented in this dissertation support the possibility that MTs and AFs play a significant role in mechano-transduction within a cell, and in particular can carry a significant mechanical load for the cell in compression.

Decoupling stiffness contributions from subcellular components is a significant step towards a deeper fundamental understanding of the morphology and structural mechanics of walled cells. To separate material properties from structure, a continuum model is needed. In Chapter 4, a FEM is used to investigate the possibility of decoupling turgor pressure and CW material properties from a single AFM indentation measurement. Turgor pressure and CW elasticity are found to be intricately linked and standard fitting methods could not separate the two properties from a single indentation measurement. The observed correlations between turgor pressure and CW elastic modulus demonstrate the non-unique set of solutions that are possible from fitting AFM force spectra obtained on microbes to a FEM. The two parameters can be separated from a single AFM force spectra by using metrics that account for multiple facets of the transformation of the force spectra with changing turgor pressure and CW elasticity. Here we present one such possibility and demonstrate a reduction in error by 20% for estimating CW elastic modulus and 11% for turgor pressure when compared to the standard least squares regression function.

The knowledge gained through these studies has implications for human health, agriculture, molecular biology and biotechnology, and environmental sustainability. In the field of human health, for instance, human bodies are colonized by many bacteria, which can either exist with us in harmony, or be a detriment to our health. Deepening our understanding of the biomechanics of bacteria can help researchers determine the best practices for developing new drugs and treatments. For example, a method is needed to determine both turgor pressure and CW elasticity with confidence for medical researchers to understand if a new antibiotic treatment works to destroy bacteria through weakening the CW or through forcing the cell to expel solutes and lose equilibrium with the surrounding osmotic solution. Then, if a new antibiotic-resistant strain of bacteria emerges, researchers may be able to use this knowledge of turgor pressure and CW elasticity to determine the underlying resistance mechanism the new strain has developed.

## **5.1 Future Work in Models of Walled Cells**

The discrete two-spring model presented in this dissertation can be used as a general starting point for a more complex spring model. More springs can be added in series

or parallel to represent various subcellular components. To be able to decouple the contributions from each of the subcellular components in the model, the only experimental requirement is that the component can be removed from the cell in the micro- and nano-indentation experiments. For example, a spring could be added in series in the cytoplasmic layer of the two-spring model to represent the nucleus of a cell. Assuming that the nucleus of the cell can be removed, and the cell can be tested afterwards in indentation experiments, the contribution of the nucleus to the overall stiffness of the cell in compression could be determined. This is a particularly interesting subject to investigate in the presented multi-scale biomechanical assay, as there is new emerging evidence that the nucleus stiffens in response to plasmolyzing environmental conditions [106].

The discrete model of a cell also has a general utility in uncovering nonlinear phenomena and unexpected interactions. In Chapter 2, the two-spring model was unable to account for the extreme increase of stiffness in plasmolyzed transgenic *Arabidopsis thaliana* VND7 cells in stage 2 of differentiation as compared to stages 1 and 3. If the cell in stage 2 does have both a primary cell wall (PCW) and a secondary cell wall (SCW), which are acting as a combined cell wall, then the stiffness of the combined cell wall should be close to the addition of the stiffness measured from the isolated PCW and SCW. This is not observed. Instead, the combined PCW and SCW of stage 2 of transdifferentiation is more than double the addition of the isolated PCW and SCW stiffnesses. Therefore, a nonlinear interaction between the two cell walls in plasmolyzing conditions must be occurring, and several hypotheses for what that interaction could be are proposed in Chapter 2. The same logic could be applied to any composite material under indentation using the discrete spring model. If the spring model is unable to explain the measured stiffnesses, this may suggest a nonlinear interaction between the constituent properties.

A combination of the finite-element modeling methodology presented in Chapter 4 with the experimental techniques presented in Chapters 2 and 3 would help calculate the material properties of subcellular components of a plant cell, separate from the cell structure. While it was difficult to decouple the mechanics of the CW and the cytoplasm from a single AFM measurement on a microbe, there is a strong possibility that the structure and material properties of the cell wall and cytoplasm can be separated for plant cells because we can probe their mechanics at two scales, using both the micro-indentation and the nano-indentation experiment. The mechanics of cytoskeletal filaments would be particularly relevant while trying to capture behavior

using a finite-element model. The modeling of individual filaments could be too time-intensive, but a surrogate property is still possible to model. For example, introducing compressibility to the cytoplasm could be used to represent the buckling behavior of cytoskeletal filaments in compression. Another aspect that may be of interest is the time-dependent behavior of walled cells, namely their viscoelastic or poroviscoelastic behavior. In principle, such effects can be incorporated in the mechanical models by including damping in the form of dashpots. The change in mechanics across drug treatments, osmotic conditions, or stages of differentiation could then be studied to determine how the discrete subcellular components react to each of these conditions.

## **5.2 Future Work in Parameter Fitting for Walled Cell Models**

There are many opportunities to refine and improve the parameter fitting methods presented here. The development of a statistical framework for determining the relative stiffness magnitudes of subcellular components was used in this dissertation to further our fundamental biomechanical understanding of the way each component responds to changes in the environment. Here we investigated a handful of parameters, which made the brute-force computation of the posterior possible. To extend this approach to calculate the stiffness contributions from any number of subcellular components of the cell, a method such as Markov chain Monte Carlo would be necessary to sample from the posterior rather than attempting to do the full calculation. With this change, however, the framework set up here could be extended to determine the stiffness contribution from any number of the thousands of proteins that could exist inside a plant cell.

The inverse analysis presented in Chapter 4 could also be refined to locate the best fit material parameters more quickly and more precisely. To speed up the computation, more efficient optimization algorithms could be used to sample from the parameter space, rather than necessitating running simulations spaced throughout the range of possible parameters. Alternatively, if using the same parameter mesh framework, a remeshing of the parameter space can be used to refine the precise location of the minimum of the objective function. After a node which minimizes the objective function is located in the coarse mesh, the mesh can be refined in the area of the minimal node, and more simulations can be run at each refined mesh node to increase the precision of the estimated parameters.

### 5.3 Extensions to Biocomposites and Living Materials

The detrimental effects of petroleum-based plastics manufacturing and consumption have led scientists and engineers to investigate natural materials as sustainable and efficient alternatives to plastics [107]. Natural wood is amongst the most important and widely used sustainable structural materials [48]. Further, plant fibers, recycled wood, and other plant products have long been used to create biocomposite materials [108, 109]. Bacterial cellulose has also been used in biocomposites to enhance paper strength, in acoustic diaphragms for audio speakers, and as artificial skin material [110]. So, an advanced understanding of the physical properties and structure of individual plant and bacterial cells and their subcellular components through the work presented in this dissertation, and others like it, will inevitably lead to an improved knowledge of the bulk properties of biocomposite materials. Additionally, the ability to measure and control the development of these physical properties, like the cell wall structure, would allow for fine control of biocomposite properties to meet the requirements of various applications.

Living materials have also received much recent research attention. Advances in synthetic biology have revealed the plethora of engineering applications that living cells can be designed to accomplish. For example, the field of bioremediation has elucidated many microorganisms that can be used to consume and break down many environmental pollutants, including polyaromatic hydrocarbons created by the oil production industry and pesticides from the agriculture industry [111]. Living materials also possess the desirable material property of self-healing. Through the mineralization process, bacteria can be used in engineering practice to heal incredibly strong, yet brittle materials, like concrete and limestone [112]. Living materials can respond to many external stimuli, not just damage. For example, Piraner et al. created thermal bioswitches which have tunable temperature thresholds [113]. Before scientists and engineers can apply fully-fledged structural biofilms in practice, one needs to understand how these living materials respond to mechanical forces.

One type of living material which has received much recent attention is the biofilm. AFM nano-indentation is a commonly used technique for measuring the elastic properties of thin films, and can be used in conjunction with a soft cantilever to measure the elastic properties of soft materials, like biofilms [114]. Kesel et al. used AFM nano-indentation, rheology and a profilometric analysis to characterize two types of *Bacillus subtilis* biofilms [115]. The AFM indentation data was used

to obtain an estimate of the Young's modulus of the biofilms, which they used to demonstrate that the surface elasticity of the biofilm is significantly affected by the presence of specific proteins in the EPS. Asally et al. demonstrated that the mechanical stiffness of the extracellular matrix and the location of cell death are both important for wrinkle formation in a biofilm [116]. They found that cell death occurs before wrinkle formation, and by inducing cell death in a synthetic pattern, they were able to create a synthetically patterned wrinkle formation on the biofilm. Cell death induces the lateral mechanical forces required for biofilm wrinkle formation. The stiffness of the extracellular matrix also matters for wrinkle formation. Indentation methods have been successfully used to measure the mechanics of the constituent cells, matrix materials, and the composite living material or biocomposite. In the future, a multi-scale model that uses information from indentation experiments at these vastly different length scales could be used to further our knowledge of the mechanical behavior of living materials and biocomposites, and begin using them in practice at a large scale.

## References

- [48] Lorna J Gibson. “The hierarchical structure and mechanics of plant materials”. In: *Journal of the royal society interface* 9.76 (2012), pp. 2749–2766.
- [106] Rituparna Goswami et al. “Is the plant nucleus a mechanical rheostat?” In: *Current Opinion in Plant Biology*. Cell signalling and gene regulation 57 (Oct. 1, 2020), pp. 155–163. ISSN: 1369-5266. DOI: 10.1016/j.pbi.2020.09.001. URL: <https://www.sciencedirect.com/science/article/pii/S1369526620301072> (visited on 02/26/2021).
- [107] Amar K. Mohanty et al. “Composites from renewable and sustainable resources: Challenges and innovations”. In: *Science* 362.6414 (2018), pp. 536–542. ISSN: 0036-8075. DOI: 10.1126/science.aat9072. eprint: <https://science.sciencemag.org/content/362/6414/536.full.pdf>. URL: <https://science.sciencemag.org/content/362/6414/536>.
- [108] A. K. Mohanty, M. Misra, and G. Hinrichsen. “Biofibres, biodegradable polymers and biocomposites: An overview”. In: *Macromolecular Materials and Engineering* 276-277.1 (2000), pp. 1–24. DOI: 10.1002/(SICI)1439-2054(20000301)276:1<1::AID-MAME1>3.0.CO;2-W. eprint: <https://onlinelibrary.wiley.com/doi/pdf/10.1002/%28SICI%291439-2054%2820000301%29276%3A1%3C1%3A%3AAID-MAME1%3E3.0.CO%3B2-W>. URL: <https://onlinelibrary.wiley.com/doi/abs/10.1002/%28SICI%291439-2054%2820000301%29276%3A1%3C1%3A%3AAID-MAME1%3E3.0.CO%3B2-W>.
- [109] Murali M. Reddy et al. “Biobased plastics and bionanocomposites: Current status and future opportunities”. In: *Progress in Polymer Science* 38.10 (2013). Progress in Bionanocomposites: from green plastics to biomedical applications, pp. 1653–1689. ISSN: 0079-6700. DOI: <https://doi.org/10.1016/j.progpolymsci.2013.05.006>. URL: <http://www.sciencedirect.com/science/article/pii/S0079670013000476>.
- [110] Kuan-Chen Cheng, Jeff M Catchmark, and Ali Demirci. “Enhanced production of bacterial cellulose by using a biofilm reactor and its material property analysis”. In: *Journal of biological engineering* 3.1 (2009), pp. 1–10.
- [111] M. Vidali. “Bioremediation. An overview”. In: *Pure and Applied Chemistry* 73.7 (July 1, 2001), pp. 1163–1172. ISSN: 1365-3075, 0033-4545. DOI: 10.1351/pac200173071163. URL: <https://www.degruyter.com/view/journals/pac/73/7/article-p1163.xml> (visited on 01/08/2021).
- [112] Alan W. Decho. “Overview of biopolymer-induced mineralization: What goes on in biofilms?” In: *Ecological Engineering* 36.2 (Feb. 2010), pp. 137–144. ISSN: 09258574. DOI: 10.1016/j.ecoleng.2009.01.003. URL: <https://linkinghub.elsevier.com/retrieve/pii/S0925857409001128> (visited on 01/08/2021).

- [113] Dan I Piraner et al. “Tunable thermal bioswitches for in vivo control of microbial therapeutics”. In: *Nature Chemical Biology* 13.1 (Jan. 2017), pp. 75–80. ISSN: 1552-4450, 1552-4469. DOI: 10.1038/nchembio.2233. URL: <http://www.nature.com/articles/nchembio.2233> (visited on 01/11/2021).
- [114] Peter C.Y. Lau et al. “Absolute Quantitation of Bacterial Biofilm Adhesion and Viscoelasticity by Microbead Force Spectroscopy”. In: *Biophysical Journal* 96.7 (Apr. 2009), pp. 2935–2948. ISSN: 00063495. DOI: 10.1016/j.bpj.2008.12.3943. URL: <https://linkinghub.elsevier.com/retrieve/pii/S0006349509004226> (visited on 01/26/2021).
- [115] Sara Kesel et al. “Direct Comparison of Physical Properties of *Bacillus subtilis* NCIB 3610 and B-1 Biofilms”. In: *Applied and Environmental Microbiology* 82.8 (Apr. 15, 2016). Ed. by J. L. Schottel, pp. 2424–2432. ISSN: 0099-2240, 1098-5336. DOI: 10.1128/AEM.03957-15. URL: <http://aem.asm.org/lookup/doi/10.1128/AEM.03957-15> (visited on 01/08/2021).
- [116] M. Asally et al. “Localized cell death focuses mechanical forces during 3D patterning in a biofilm”. In: *Proceedings of the National Academy of Sciences* 109.46 (Nov. 13, 2012), pp. 18891–18896. ISSN: 0027-8424, 1091-6490. DOI: 10.1073/pnas.1212429109. URL: <http://www.pnas.org/cgi/doi/10.1073/pnas.1212429109> (visited on 01/12/2021).

## Appendix A

### PARAMETER FITTING METHODS

This appendix describes the parameter fitting methods used in this thesis.

#### Ordinary Least Squares (OLS)

The most commonly used parameter fitting method is simple linear regression [117]. The simple linear regression model for the spring constant of a force-indentation data set is

$$F_i = a + k\Delta_i + e_i \quad (\text{A.1})$$

where  $a$  and  $k$  are the regression coefficients,  $F_i$  is the variable which represents the incremental contact force,  $\Delta_i$  is the variable which represents the incremental indentation depth, and  $e_i$  is a random statistical error. To solve for the regression coefficients using an ordinary least squares (OLS) method, we must assume that the errors  $e_i$  are independent (we are not, for example, accumulating errors in the measurement with each indentation depth increment), the expected value of the errors at any given incremental indentation depth  $\Delta_i$  is zero ( $\mathbb{E}[e_i | \Delta_i] = 0$ ), and the variance of the errors is homoscedastic ( $\mathbb{V}[e_i | \Delta_i] = \sigma^2$ ). OLS is the standard regression method, and the resulting regression coefficients are those that minimize the residual sum of squares (RSS)

$$RSS = \sum_{i=1}^n \hat{e}_i^2 = \sum_{i=1}^n (F_i - a - k\Delta_i)^2 \rightarrow \text{minimize}, \quad (\text{A.2})$$

where  $\hat{e}_i$  is the residual, and  $F_i$  and  $\Delta_i$  now represent incremental measurements from experimental indentations. The residual  $\hat{e}_i$  can be viewed as a realization of  $e_i$ , and it can be used to check the model assumptions.

#### Maximum Likelihood Estimate (MLE)

A small modification of OLS assumptions leads to another common parameter fitting method: the maximum likelihood estimate (MLE) [117]. The general assumptions of independent errors ( $e_i$ ),  $\mathbb{E}[e_i | \Delta_i] = 0$ , and  $\mathbb{V}[e_i | \Delta_i] = \sigma^2$  can be combined into a more specific assumption that the errors are normally distributed

$$e_i | \Delta_i \sim \mathcal{N}(0, \sigma^2). \quad (\text{A.3})$$

Then, the distribution of the measured indentation force is also normally distributed,

$$F_i | \Delta_i \sim \mathcal{N}(a + k\Delta_i, \sigma^2). \quad (\text{A.4})$$

The likelihood function is the joint probability of observing our collected force-indentation depth data given regression parameters  $a$  and  $b$  and the variance  $\sigma^2$ ,

$$\mathcal{L}((F_i, \Delta_i) | a, k, \sigma^2) = \prod_{i=1}^n \frac{1}{\sqrt{2\pi}\sigma} \exp \left[ -\frac{(F_i - a - k\Delta_i)^2}{2\sigma^2} \right]. \quad (\text{A.5})$$

The product can be translated to a summation in the exponential

$$\mathcal{L}((F_i, \Delta_i) | a, k, \sigma^2) = \left( \frac{1}{\sqrt{2\pi}\sigma} \right)^{-n} \exp \left[ -\frac{\sum_{i=1}^n (F_i - a - k\Delta_i)^2}{2\sigma^2} \right]. \quad (\text{A.6})$$

The summation in the exponential is exactly the residual sum of squares (RSS) presented in Equation A.2. To maximize the likelihood  $\mathcal{L}((F_i, \Delta_i) | a, k, \sigma^2)$  with respect to the regression parameters, we must again minimize the residual sum of squares. Therefore, the most likely estimates of  $a$  and  $k$  are also the regression parameters that minimize the residual sum of squares. For comparison with the maximum a posteriori (MAP) estimate in the next section, we can write this optimization as

$$\theta_{\text{MLE}} = \arg \max_{\theta} \mathcal{L}((F_i, \Delta_i) | a, k, \sigma^2), \quad (\text{A.7})$$

where  $\theta$  represents the regression parameters and the subscript MLE is used to denote the maximum likelihood estimate for the regression parameters.

### Maximum a Posteriori (MAP) Estimate

The only difference between the MLE and the MAP is the inclusion of the prior distribution in the MAP [90, 91]. Recall Bayes' theorem

$$\mathcal{F}(\theta|y) = \frac{\mathcal{L}(y | \theta)P(\theta)}{f(y)} \quad (\text{A.8})$$

which we can rewrite for the problem of fitting force-indentation data to a line, as we have been discussing so far,

$$\mathcal{F}(a, k, \sigma^2 | (F_i, \Delta_i)) = \frac{\mathcal{L}((F_i, \Delta_i) | a, k, \sigma^2)P(a, k, \sigma^2)}{f(F_i, \Delta_i)}, \quad (\text{A.9})$$

where  $f(F_i, \Delta_i)$  is a normalization constant called the evidence. This term can be ignored strictly for the purposes of parameter optimization. So the posterior is proportional to the likelihood multiplied by the prior,

$$\mathcal{F}(a, k, \sigma^2 | (F_i, \Delta_i)) \propto \mathcal{L}((F_i, \Delta_i) | a, k, \sigma^2)P(a, k, \sigma^2). \quad (\text{A.10})$$

If we replace the likelihood from the MLE optimization in Equation A.7 with the posterior, we get

$$\theta_{\text{MAP}} = \arg \max_{\theta} \mathcal{L}((F_i, \Delta_i) | a, b, \sigma^2) P(a, b, \sigma^2). \quad (\text{A.11})$$

Maximizing the posterior is equivalent to maximizing the logarithm of the posterior, so we can rewrite the above equation as

$$\begin{aligned} \theta_{\text{MAP}} &= \arg \max_{\theta} \mathcal{L}((F_i, \Delta_i) | a, b, \sigma^2) P(a, b, \sigma^2) \\ &= \arg \max_{\theta} \log \mathcal{L}((F_i, \Delta_i) | a, b, \sigma^2) + \log P(a, b, \sigma^2). \end{aligned}$$

So, the only difference between the MLE and MAP optimizations is the inclusion of the prior information. In other words, the optimization function for the MAP is the likelihood weighted by the prior.

**References**

- [90] Justin Bois. *Introduction to Bayesian Modeling*. Sept. 2018. URL: [http://bebi103.caltech.edu.s3-website-us-east-1.amazonaws.com/2018/lecture\\_notes/105\\_intro\\_to\\_bayesian\\_modeling.pdf](http://bebi103.caltech.edu.s3-website-us-east-1.amazonaws.com/2018/lecture_notes/105_intro_to_bayesian_modeling.pdf).
- [91] Michael Betancourt. *Probabilistic Modeling and Statistical Inference*. betanalpha.github.io. Mar. 2019. URL: [https://betanalpha.github.io/assets/case\\_studies/modeling\\_and\\_inference.html](https://betanalpha.github.io/assets/case_studies/modeling_and_inference.html).
- [117] Konstantin Zuev. “Statistical Inference”. In: *arXiv:1603.04929 [math, stat]* (Mar. 15, 2016). arXiv: 1603.04929. URL: <http://arxiv.org/abs/1603.04929> (visited on 02/24/2021).

## BIBLIOGRAPHY

- [1] Elisabeth Fischer-Friedrich et al. “Quantification of surface tension and internal pressure generated by single mitotic cells”. In: *Scientific Reports* 4.1 (Aug. 29, 2014). Number: 1 Publisher: Nature Publishing Group, p. 6213. ISSN: 2045-2322. DOI: 10.1038/srep06213. URL: <https://www.nature.com/articles/srep06213> (visited on 02/22/2021).
- [2] D. S. Cayley, H. J. Guttman, and M. T. Record. “Biophysical characterization of changes in amounts and activity of Escherichia coli cell and compartment water and turgor pressure in response to osmotic stress”. In: *Biophysical Journal* 78.4 (Apr. 2000), pp. 1748–1764. ISSN: 0006-3495. DOI: 10.1016/s0006-3495(00)76726-9.
- [3] Daniel J. Cosgrove. “Assembly and enlargement of the primary cell wall in plants”. In: *Annual Review of Cell and Developmental Biology* 13.1 (1997). PMID: 9442872, pp. 171–201. DOI: 10.1146/annurev.cellbio.13.1.171. eprint: <https://doi.org/10.1146/annurev.cellbio.13.1.171>. URL: <https://doi.org/10.1146/annurev.cellbio.13.1.171>.
- [4] Kenneth W. Foster. “Chapter 47 - Flagella, Cilia, Actin- and Centrin-based Movement”. In: *Cell Physiology Source Book (Fourth Edition)*. Ed. by Nicholas Sperelakis. San Diego: Academic Press, Jan. 1, 2012, pp. 823–853. ISBN: 978-0-12-387738-3. DOI: 10.1016/B978-0-12-387738-3.00047-0. URL: <https://www.sciencedirect.com/science/article/pii/B9780123877383000470> (visited on 02/22/2021).
- [5] Wieland Fricke. “Turgor Pressure”. In: *eLS*. Ed. by John Wiley & Sons Ltd. Chichester, UK: John Wiley & Sons, Ltd, Jan. 16, 2017, pp. 1–6. ISBN: 978-0-470-01590-2 978-0-470-01617-6. DOI: 10.1002/9780470015902.a0001687.pub2. URL: <http://doi.wiley.com/10.1002/9780470015902.a0001687.pub2> (visited on 02/04/2021).
- [6] Daniel J. Cosgrove, Elizabeth Van Volkenburgh, and Robert E. Cleland. “Stress relaxation of cell walls and the yield threshold for growth”. In: *Planta* 162.1 (Sept. 1, 1984), pp. 46–54. ISSN: 1432-2048. DOI: 10.1007/BF00397420. URL: <https://doi.org/10.1007/BF00397420> (visited on 02/22/2021).
- [7] Fred Chang and Kerwyn Casey Huang. “How and why cells grow as rods”. In: *BMC Biology* 12.1 (Aug. 2, 2014), p. 54. ISSN: 1741-7007. DOI: 10.1186/s12915-014-0054-8. URL: <https://doi.org/10.1186/s12915-014-0054-8> (visited on 02/22/2021).
- [8] E. Steudle. “Pressure probe techniques: basic principles and application to studies of water and solute relations at the cell, tissue and organ level”. In: *Water deficits* (1993), pp. 5–36. URL: <https://docuserve.library>.

caltech.edu/illiad/illiad.dll?Action=10&Form=75&Value=531985 (visited on 02/05/2021).

- [9] A. Deri Tomos and Roger A. Leigh. “THE PRESSURE PROBE: A Versatile Tool in Plant Cell Physiology”. In: *Annual Review of Plant Physiology and Plant Molecular Biology* 50.1 (1999), pp. 447–472. DOI: 10.1146/annurev.arplant.50.1.447. URL: <https://doi.org/10.1146/annurev.arplant.50.1.447> (visited on 02/04/2021).
- [10] Roger R. Lew. “How does a hypha grow? The biophysics of pressurized growth in fungi”. In: *Nature Reviews Microbiology* 9.7 (July 2011). Number: 7 Publisher: Nature Publishing Group, pp. 509–518. ISSN: 1740-1534. DOI: 10.1038/nrmicro2591. URL: <https://www.nature.com/articles/nrmicro2591> (visited on 02/04/2021).
- [11] Anthony Edward Walsby. “The pressure relationships of gas vacuoles”. In: *Proceedings of the Royal Society of London. Series B. Biological Sciences* 178.1052 (Aug. 3, 1971), pp. 301–326. ISSN: 0080-4649, 2053-9193. DOI: 10.1098/rspb.1971.0067. URL: <https://royalsocietypublishing.org/doi/10.1098/rspb.1971.0067> (visited on 02/04/2021).
- [12] Raymond W. Bourdeau et al. “Acoustic reporter genes for noninvasive imaging of microorganisms in mammalian hosts”. In: *Nature* 553.7686 (Jan. 3, 2018), pp. 86–90. ISSN: 1476-4687. DOI: 10.1038/nature25021.
- [13] M. Arnoldi et al. “Bacterial turgor pressure can be measured by atomic force microscopy”. In: *Physical Review. E, Statistical Physics, Plasmas, Fluids, and Related Interdisciplinary Topics* 62.1 (July 2000), pp. 1034–1044. ISSN: 1063-651X. DOI: 10.1103/physreve.62.1034.
- [14] Dominic Vella et al. “The indentation of pressurized elastic shells: from polymeric capsules to yeast cells”. In: *Journal of The Royal Society Interface* 9.68 (Mar. 7, 2012), pp. 448–455. ISSN: 1742-5689, 1742-5662. DOI: 10.1098/rsif.2011.0352. URL: <https://royalsocietypublishing.org/doi/10.1098/rsif.2011.0352> (visited on 11/11/2019).
- [15] Anne-Lise Routier-Kierzkowska et al. “Cellular Force Microscopy for in Vivo Measurements of Plant Tissue Mechanics”. In: *Plant Physiology* 158.4 (2012), pp. 1514–1522. ISSN: 0032-0889. DOI: 10.1104/pp.111.191460. eprint: <http://www.plantphysiol.org/content/158/4/1514.full.pdf>. URL: <http://www.plantphysiol.org/content/158/4/1514>.
- [16] Gang Bao and Subra Suresh. “Cell and molecular mechanics of biological materials”. In: *Nature materials* 2.11 (2003), pp. 715–725.
- [17] Amir J Bidhendi and Anja Geitmann. “Methods to quantify primary plant cell wall mechanics”. In: *Journal of Experimental Botany* 70.14 (July 2019), pp. 3615–3648. ISSN: 0022-0957. DOI: 10.1093/jxb/erz281. eprint: <https://academic.oup.com/jxb/article-pdf/70/14/3615/>

- 28985115/erz281.pdf. URL: <https://doi.org/10.1093/jxb/erz281>.
- [18] S Aguayo et al. “Single-bacterium nanomechanics in biomedicine: unravelling the dynamics of bacterial cells”. In: *Nanotechnology* 26.6 (2015), p. 062001.
- [19] Alexis Peaucelle, Raymond Wightman, and Herman Höfte. “The control of growth symmetry breaking in the Arabidopsis hypocotyl”. In: *Current Biology* 25.13 (2015), pp. 1746–1752.
- [20] Siobhan A. Braybrook and Alexis Peaucelle. “Mechano-Chemical Aspects of Organ Formation in Arabidopsis thaliana: The Relationship between Auxin and Pectin”. In: *PLOS ONE* 8.3 (Mar. 2013), pp. 1–10. DOI: 10.1371/journal.pone.0057813. URL: <https://doi.org/10.1371/journal.pone.0057813>.
- [21] Chung-Souk Han, Seyed HR Sanei, and Farid Alisafaei. “On the origin of indentation size effects and depth dependent mechanical properties of elastic polymers”. In: *Journal of Polymer Engineering* 36.1 (2016), pp. 103–111.
- [22] Ksenija Radotić et al. “Atomic force microscopy stiffness tomography on living Arabidopsis thaliana cells reveals the mechanical properties of surface and deep cell-wall layers during growth”. eng. In: *Biophysical Journal* 103.3 (Aug. 2012), pp. 386–394. ISSN: 1542-0086. DOI: 10.1016/j.bpj.2012.06.046.
- [23] Pascale Milani, Siobhan A. Braybrook, and Arezki Boudaoud. “Shrinking the hammer: micromechanical approaches to morphogenesis”. In: *Journal of Experimental Botany* 64.15 (July 2013), pp. 4651–4662. ISSN: 0022-0957. DOI: 10.1093/jxb/ert169. eprint: <https://academic.oup.com/jxb/article-pdf/64/15/4651/18043081/ert169.pdf>. URL: <https://doi.org/10.1093/jxb/ert169>.
- [24] Arun Sampathkumar et al. “Subcellular and supracellular mechanical stress prescribes cytoskeleton behavior in Arabidopsis cotyledon pavement cells”. In: *eLife* 3 (Apr. 2014). Ed. by Dominique Bergmann, e01967. ISSN: 2050-084X. DOI: 10.7554/eLife.01967. URL: <https://doi.org/10.7554/eLife.01967>.
- [25] Siobhan A. Braybrook. “Chapter 13 - Measuring the elasticity of plant cells with atomic force microscopy”. In: *Biophysical Methods in Cell Biology*. Ed. by Ewa K. Paluch. Vol. 125. Methods in Cell Biology. Academic Press, 2015, pp. 237–254. DOI: <https://doi.org/10.1016/bs.mcb.2014.10.006>. URL: <http://www.sciencedirect.com/science/article/pii/S0091679X14000077>.
- [26] Elham Forouzesh et al. “In vivo extraction of Arabidopsis cell turgor pressure using nanoindentation in conjunction with finite element modeling”. In: *The Plant Journal* 73.3 (2013), pp. 509–520.

- [27] Léna Beauzamy, Julien Derr, and Arezki Boudaoud. “Quantifying hydrostatic pressure in plant cells by using indentation with an atomic force microscope”. In: *Biophysical journal* 108.10 (2015), pp. 2448–2456.
- [28] Alain Weber et al. “Measuring the mechanical properties of plant cells by combining micro-indentation with osmotic treatments”. In: *Journal of Experimental Botany* 66.11 (Apr. 2015), pp. 3229–3241. ISSN: 0022-0957. DOI: [10.1093/jxb/erv135](https://doi.org/10.1093/jxb/erv135). eprint: <https://academic.oup.com/jxb/article-pdf/66/11/3229/17137090/erv135.pdf>. URL: <https://doi.org/10.1093/jxb/erv135>.
- [29] Yi Deng, Mingzhai Sun, and Joshua W. Shaevitz. “Direct Measurement of Cell Wall Stress Stiffening and Turgor Pressure in Live Bacterial Cells”. In: *Physical Review Letters* 107.15 (Oct. 6, 2011). Publisher: American Physical Society, p. 158101. DOI: [10.1103/PhysRevLett.107.158101](https://doi.org/10.1103/PhysRevLett.107.158101). URL: <https://link.aps.org/doi/10.1103/PhysRevLett.107.158101> (visited on 02/07/2021).
- [30] Alexis Peaucelle et al. “Pectin-induced changes in cell wall mechanics underlie organ initiation in Arabidopsis”. In: *Current biology* 21.20 (2011), pp. 1720–1726.
- [31] D. B. MacManus et al. “Dynamic mechanical properties of murine brain tissue using micro-indentation”. In: *Journal of Biomechanics* 48.12 (Sept. 18, 2015), pp. 3213–3218. ISSN: 0021-9290. DOI: [10.1016/j.jbiomech.2015.06.028](https://doi.org/10.1016/j.jbiomech.2015.06.028). URL: <https://www.sciencedirect.com/science/article/pii/S002192901500370X> (visited on 02/24/2021).
- [32] Camilo Velez, Robin E. Carroll, and David P. Arnold. “Direct measurement and microscale mapping of nanoNewton to milliNewton magnetic forces”. In: *AIP Advances* 7.5 (Mar. 7, 2017). Publisher: American Institute of Physics, p. 056809. DOI: [10.1063/1.4978316](https://doi.org/10.1063/1.4978316). URL: <https://aip.scitation.org/doi/full/10.1063/1.4978316> (visited on 02/24/2021).
- [33] Dimitris Felekis et al. “Quantifying growth mechanics of living, growing plant cells in situ using microrobotics”. In: *Micro & Nano Letters* 6.5 (2011), pp. 311–316.
- [34] Hannes Vogler et al. “The pollen tube: a soft shell with a hard core”. In: *The Plant Journal* 73.4 (2013), pp. 617–627.
- [35] J.-E. Bolduc et al. “Finite-element analysis of geometrical factors in micro-indentation of pollen tubes”. In: *Biomechanics and Modeling in Mechanobiology* 5.4 (Nov. 2006), pp. 227–236. ISSN: 1617-7959. DOI: [10.1007/s10237-005-0010-1](https://doi.org/10.1007/s10237-005-0010-1).
- [36] Evan A. Zamir and Larry A. Taber. “On the effects of residual stress in microindentation tests of soft tissue structures”. In: *Journal of Biomechan-*

- ical Engineering* 126.2 (Apr. 2004), pp. 276–283. ISSN: 0148-0731. DOI: 10.1115/1.1695573.
- [37] A Flamant et al. “Sur la répartition des pressions dans un solide rectangulaire chargé transversalement”. In: *CR Acad. Sci. Paris* 114 (1892), pp. 1465–1468.
- [38] Catherine Volle et al. “Measuring the Effect of Antimicrobial Peptides on the Biophysical Properties of Bacteria using Atomic Force Microscopy”. In: *Biophysical Journal* 114.3 (Feb. 2018), 354a. ISSN: 00063495. DOI: 10.1016/j.bpj.2017.11.1969. URL: <https://linkinghub.elsevier.com/retrieve/pii/S0006349517332010> (visited on 02/16/2021).
- [39] Leah Ginsberg et al. “Structure and Biomechanics during Xylem Vessel Transdifferentiation in *Arabidopsis thaliana*”. en. In: *Plants* 9.12 (Dec. 2020), p. 1715. ISSN: 2223-7747. DOI: 10.3390/plants9121715. URL: <https://www.mdpi.com/2223-7747/9/12/1715>.
- [40] Leah Ginsberg et al. “Cell wall and cytoskeletal contributions in single cell biomechanics of *Nicotiana tabacum*”. In: *Plant and Cell Physiology* (In review).
- [41] C Ferguson et al. “Location of cellulose and callose in pollen tubes and grains of *Nicotiana tabacum*”. In: *Planta* 206.3 (1998), pp. 452–460.
- [42] H. Hertz. “Über die Berührung fester elastischer Körper (On the contact of elastic solids)”. In: *Journal für die reine und angewandte Mathematik* 82 (1882), pp. 156–171.
- [43] Ian N. Sneddon. “The relation between load and penetration in the axisymmetric boussinesq problem for a punch of arbitrary profile”. In: *International Journal of Engineering Science* 3.1 (May 1, 1965), pp. 47–57. ISSN: 0020-7225. DOI: 10.1016/0020-7225(65)90019-4. URL: <https://www.sciencedirect.com/science/article/pii/0020722565900194> (visited on 02/23/2021).
- [44] Kenneth Langstreth Johnson et al. “Surface energy and the contact of elastic solids”. In: *Proceedings of the Royal Society of London. A. Mathematical and Physical Sciences* 324.1558 (Sept. 8, 1971). Publisher: Royal Society, pp. 301–313. DOI: 10.1098/rspa.1971.0141. URL: <https://royalsocietypublishing.org/doi/10.1098/rspa.1971.0141> (visited on 02/23/2021).
- [45] Eric Reissner. “Stresses and Small Displacements of Shallow Spherical Shells. I”. In: *Journal of Mathematics and Physics* 25.1 (Apr. 1946), pp. 80–85. ISSN: 00971421. DOI: 10.1002/sapm194625180. URL: <http://doi.wiley.com/10.1002/sapm194625180> (visited on 11/06/2019).

- [46] A Pogorelov. *Bendings of Surfaces and Stability of Shells*. Vol. 72. Translations of Mathematical Monographs. Providence, Rhode Island: American Mathematical Society, 1988. ISBN: 978-0-8218-4525-7 978-1-4704-4486-0. DOI: 10.1090/mmono/072. URL: <http://www.ams.org/mmono/072> (visited on 02/03/2021).
- [47] L. A. Taber. “Large Deflection of a Fluid-Filled Spherical Shell Under a Point Load”. In: *Journal of Applied Mechanics* 49.1 (Mar. 1, 1982), pp. 121–128. ISSN: 0021-8936, 1528-9036. DOI: 10.1115/1.3161953. URL: <https://asmedigitalcollection.asme.org/appliedmechanics/article/49/1/121/388706/Large-Deflection-of-a-FluidFilled-Spherical-Shell> (visited on 11/06/2019).
- [48] Lorna J Gibson. “The hierarchical structure and mechanics of plant materials”. In: *Journal of the royal society interface* 9.76 (2012), pp. 2749–2766.
- [49] Ruiqin Zhong, Dongtao Cui, and Zheng-Hua Ye. “Secondary cell wall biosynthesis”. In: *New Phytologist* 221.4 (2019), pp. 1703–1723. DOI: 10.1111/nph.15537. eprint: <https://nph.onlinelibrary.wiley.com/doi/pdf/10.1111/nph.15537>. URL: <https://nph.onlinelibrary.wiley.com/doi/abs/10.1111/nph.15537>.
- [50] Robert J. Moon et al. “Cellulose nanomaterials review: structure, properties and nanocomposites”. In: *Chem. Soc. Rev.* 40 (7 2011), pp. 3941–3994. DOI: 10.1039/C0CS00108B. URL: <http://dx.doi.org/10.1039/C0CS00108B>.
- [51] Daniel J. Cosgrove. “Plant cell wall extensibility: connecting plant cell growth with cell wall structure, mechanics, and the action of wall-modifying enzymes”. In: *Journal of Experimental Botany* 67.2 (Nov. 2015), pp. 463–476. ISSN: 0022-0957. DOI: 10.1093/jxb/erv511. eprint: <https://academic.oup.com/jxb/article-pdf/67/2/463/9366332/erv511.pdf>. URL: <https://doi.org/10.1093/jxb/erv511>.
- [52] Ovijit Chaudhuri, Sapun H. Parekh, and Daniel A. Fletcher. “Reversible stress softening of actin networks”. In: *Nature* 445.7125 (2007), pp. 295–298. ISSN: 1476-4687. DOI: 10.1038/nature05459. URL: <https://doi.org/10.1038/nature05459>.
- [53] F Gittes et al. “Flexural rigidity of microtubules and actin filaments measured from thermal fluctuations in shape.” In: *Journal of Cell Biology* 120.4 (Feb. 1993), pp. 923–934. ISSN: 0021-9525. DOI: 10.1083/jcb.120.4.923. eprint: <https://rupress.org/jcb/article-pdf/120/4/923/384296/923.pdf>. URL: <https://doi.org/10.1083/jcb.120.4.923>.
- [54] Pauline Durand-Smet et al. “A Comparative Mechanical Analysis of Plant and Animal Cells Reveals Convergence across Kingdoms”. In: *Biophysical Journal* 107.10 (2014), pp. 2237–2244. ISSN: 0006-3495. DOI: <https://doi.org/10.1016/j.bpj.2014.08.011>.

doi.org/10.1016/j.bpj.2014.10.023. URL: <http://www.sciencedirect.com/science/article/pii/S0006349514010741>.

- [55] Masatoshi Yamaguchi et al. “VASCULAR-RELATED NAC-DOMAIN6 and VASCULAR-RELATED NAC-DOMAIN7 Effectively Induce Transdifferentiation into Xylem Vessel Elements under Control of an Induction System”. en. In: *Plant Physiology* 153.3 (July 2010). Publisher: American Society of Plant Biologists Section: BREAKTHROUGH TECHNOLOGIES, pp. 906–914. ISSN: 0032-0889, 1532-2548. DOI: 10.1104/pp.110.154013. URL: <http://www.plantphysiol.org/content/153/3/906> (visited on 07/31/2020).
- [56] Minoru Kubo et al. “Transcription switches for protoxylem and metaxylem vessel formation”. In: *Genes & Development* 19.16 (2005), pp. 1855–1860. DOI: 10.1101/gad.1331305. eprint: <http://genesdev.cshlp.org/content/19/16/1855.full.pdf+html>.
- [57] Sacha Escamez and Hannele Tuominen. “Programmes of cell death and autolysis in tracheary elements: when a suicidal cell arranges its own corpse removal”. en. In: *Journal of Experimental Botany* 65.5 (Mar. 2014). Publisher: Oxford Academic, pp. 1313–1321. ISSN: 0022-0957. DOI: 10.1093/jxb/eru057. URL: <https://academic.oup.com/jxb/article/65/5/1313/452788> (visited on 07/31/2020).
- [58] Hiroo Fukuda. “Tracheary Element Differentiation.” In: *The Plant Cell* 9.7 (July 1997), pp. 1147–1156. ISSN: 1040-4651. URL: <https://www.ncbi.nlm.nih.gov/pmc/articles/PMC156987/> (visited on 08/01/2020).
- [59] Elena T Iakimova and Ernst J Woltering. “Xylogenesis in zinnia (*Zinnia elegans*) cell cultures: unravelling the regulatory steps in a complex developmental programmed cell death event”. In: *Planta* 245.4 (2017), pp. 681–705.
- [60] Anna Kákošová et al. “Galactoglucomannan oligosaccharides are assumed to affect tracheary element formation via interaction with auxin in *Zinnia* xylogenic cell culture”. In: *Plant cell reports* 32.4 (2013), pp. 479–487.
- [61] Hannes Vogler et al. “Measuring the Mechanical Properties of Plant Cell Walls”. In: *Plants* 4.2 (2015), pp. 167–182. ISSN: 2223-7747. DOI: 10.3390/plants4020167. URL: <https://www.mdpi.com/2223-7747/4/2/167>.
- [62] Zengfang Yin and Ruwen Fan. “Ultrastructural analysis of the differentiation process of secondary xylem vessel element in *Populus deltoides*”. en. In: *Frontiers of Forestry in China* 4.484 (July 2009). Publisher: Springer. ISSN: 1673-3630. DOI: 10.1007/s11461-009-0067-6. URL: <https://link.springer.com/article/10.1007%5C%2Fs11461-009-0067-6> (visited on 08/30/2020).

- [63] Miranda J Meents, Yoichiro Watanabe, and A Lacey Samuels. “The cell biology of secondary cell wall biosynthesis”. In: *Annals of Botany* 121.6 (Feb. 2018), pp. 1107–1125. ISSN: 0305-7364. DOI: 10.1093/aob/mcy005. eprint: <https://academic.oup.com/aob/article-pdf/121/6/1107/24805712/mcy005.pdf>. URL: <https://doi.org/10.1093/aob/mcy005>.
- [64] Benjamin Bollhöner, Jakob Prestele, and Hannele Tuominen. “Xylem cell death: emerging understanding of regulation and function”. en. In: *Journal of Experimental Botany* 63.3 (Feb. 2012). Publisher: Oxford Academic, pp. 1081–1094. ISSN: 0022-0957. DOI: 10.1093/jxb/err438. URL: <https://academic.oup.com/jxb/article/63/3/1081/475758> (visited on 08/01/2020).
- [65] Yoshihisa Oda and Seiichiro Hasezawa. “Cytoskeletal organization during xylem cell differentiation”. en. In: *Journal of Plant Research* 119.3 (May 2006), pp. 167–177. ISSN: 1618-0860. DOI: 10.1007/s10265-006-0260-8. URL: <https://doi.org/10.1007/s10265-006-0260-8> (visited on 08/03/2020).
- [66] Takema Sasaki, Hiroo Fukuda, and Yoshihisa Oda. “CORTICAL MICROTUBULE DISORDERING1 Is Required for Secondary Cell Wall Patterning in Xylem Vessels”. In: *The Plant Cell* 29.12 (2017), pp. 3123–3139. ISSN: 1040-4651. DOI: 10.1105/tpc.17.00663. eprint: <http://www.plantcell.org/content/29/12/3123.full.pdf>. URL: <http://www.plantcell.org/content/29/12/3123>.
- [67] Rene Schneider et al. “Two Complementary Mechanisms Underpin Cell Wall Patterning during Xylem Vessel Development”. In: *The Plant Cell* 29.10 (2017), pp. 2433–2449. ISSN: 1040-4651. DOI: 10.1105/tpc.17.00309. eprint: <http://www.plantcell.org/content/29/10/2433.full.pdf>. URL: <http://www.plantcell.org/content/29/10/2433>.
- [68] Joseph Boussinesq. “Application des potentials al’etude de l’equilibre et des mouvements des solides elastiques”. In: *Paris, Ganther-Villars* (1885).
- [69] Léna Beauzamy, Naomi Nakayama, and Arezki Boudaoud. “Flowers under pressure: ins and outs of turgor regulation in development”. In: *Annals of botany* 114.7 (2014), pp. 1517–1533.
- [70] Amir J Bidhendi and Anja Geitmann. “Methods to quantify primary plant cell wall mechanics”. In: *Journal of Experimental Botany* 70.14 (July 2019), pp. 3615–3648. ISSN: 0022-0957. DOI: 10.1093/jxb/erz281. eprint: <https://academic.oup.com/jxb/article-pdf/70/14/3615/28985115/erz281.pdf>. URL: <https://doi.org/10.1093/jxb/erz281>.

- [71] Y. Watanabe et al. “Visualization of cellulose synthases in Arabidopsis secondary cell walls”. en. In: *Science* 350.6257 (Oct. 2015). Publisher: American Association for the Advancement of Science Section: Report, pp. 198–203. ISSN: 0036-8075, 1095-9203. DOI: [10.1126/science.aac7446](https://doi.org/10.1126/science.aac7446). URL: <https://science.sciencemag.org/content/350/6257/198> (visited on 08/03/2020).
- [72] Pascale Milani et al. “In vivo analysis of local wall stiffness at the shoot apical meristem in Arabidopsis using atomic force microscopy”. In: *The Plant Journal* 67.6 (2011), pp. 1116–1123. DOI: <https://doi.org/10.1111/j.1365-313X.2011.04649.x>. eprint: <https://onlinelibrary.wiley.com/doi/pdf/10.1111/j.1365-313X.2011.04649.x>. URL: <https://onlinelibrary.wiley.com/doi/abs/10.1111/j.1365-313X.2011.04649.x>.
- [73] Olivier Hamant and Elizabeth S. Haswell. “Life behind the wall: sensing mechanical cues in plants”. en. In: *BMC Biology* 15.1 (Dec. 2017), p. 59. ISSN: 1741-7007. DOI: [10.1186/s12915-017-0403-5](https://doi.org/10.1186/s12915-017-0403-5). URL: <http://bmcbiol.biomedcentral.com/articles/10.1186/s12915-017-0403-5> (visited on 09/19/2020).
- [74] P Durand-Smet et al. “Estimation of turgor pressure through comparison between single plant cell and pressurized shell mechanics”. In: *Physical Biology* 14.5 (2017), p. 055002.
- [75] Jacob VanderPlas et al. “Altair: Interactive Statistical Visualizations for Python”. In: *Journal of Open Source Software* (Dec. 2018). DOI: [10.21105/joss.01057](https://doi.org/10.21105/joss.01057). URL: <https://doi.org/10.21105/joss.01057>.
- [76] C. X. WANG, L. WANG, and C. R. THOMAS. “Modelling the Mechanical Properties of Single Suspension-Cultured Tomato Cells”. In: *Annals of Botany* 93.4 (Apr. 2004), pp. 443–453. ISSN: 0305-7364. DOI: [10.1093/aob/mch062](https://doi.org/10.1093/aob/mch062). eprint: <https://academic.oup.com/aob/article-pdf/93/4/443/497606/mch062.pdf>. URL: <https://doi.org/10.1093/aob/mch062>.
- [77] Daniel J. Cosgrove. “Water Uptake by Growing Cells: An Assessment of the Controlling Roles of Wall Relaxation, Solute Uptake, and Hydraulic Conductance”. In: *International Journal of Plant Sciences* 154.1 (1993). PMID: 11537965, pp. 10–21. DOI: [10.1086/297087](https://doi.org/10.1086/297087). eprint: <https://doi.org/10.1086/297087>. URL: <https://doi.org/10.1086/297087>.
- [78] Daniel B. Szymanski and Daniel J. Cosgrove. “Dynamic Coordination of Cytoskeletal and Cell Wall Systems during Plant Cell Morphogenesis”. In: *Current Biology* 19.17 (2009), R800–R811. ISSN: 0960-9822. DOI: <https://doi.org/10.1016/j.cub.2009.07.056>. URL: <http://www.sciencedirect.com/science/article/pii/S0960982209014821>.

- [79] DJ Cosgrove. “Catalysts of plant cell wall loosening”. In: *F1000Research* 5.119 (2016). DOI: 10.12688/f1000research.7180.1.
- [80] Richard Malgat, François Faure, and Arezki Boudaoud. “A Mechanical Model to Interpret Cell-Scale Indentation Experiments on Plant Tissues in Terms of Cell Wall Elasticity and Turgor Pressure”. In: *Frontiers in Plant Science* 7 (Sept. 7, 2016). ISSN: 1664-462X. DOI: 10.3389/fpls.2016.01351. URL: <http://journal.frontiersin.org/Article/10.3389/fpls.2016.01351/abstract> (visited on 11/06/2019).
- [81] Takashi Hashimoto. “Microtubules in Plants”. In: *The Arabidopsis Book* 13 (Jan. 2015), e0179. ISSN: 1543-8120. DOI: 10.1199/tab.0179. URL: <http://www.bioone.org/doi/10.1199/tab.0179> (visited on 01/04/2021).
- [82] Andrei Smertenko et al. “A new class of microtubule-associated proteins in plants”. In: *Nature Cell Biology* 2.10 (Oct. 2000), pp. 750–753. ISSN: 1465-7392, 1476-4679. DOI: 10.1038/35036390. URL: [http://www.nature.com/articles/ncb1000\\_750](http://www.nature.com/articles/ncb1000_750) (visited on 01/24/2021).
- [83] Björn J. Sieberer et al. “Cell proliferation, cell shape, and microtubule and cellulose microfibril organization of tobacco BY-2 cells are not altered by exposure to near weightlessness in space”. In: *Planta* 230.6 (Nov. 2009), pp. 1129–1140. ISSN: 0032-0935, 1432-2048. DOI: 10.1007/s00425-009-1010-7. URL: <http://link.springer.com/10.1007/s00425-009-1010-7> (visited on 01/13/2021).
- [84] Rhoda J. Hawkins, Simon H. Tindemans, and Bela M. Mulder. “Model for the orientational ordering of the plant microtubule cortical array”. In: *Physical Review E* 82.1 (July 19, 2010), p. 011911. ISSN: 1539-3755, 1550-2376. DOI: 10.1103/PhysRevE.82.011911. URL: <https://link.aps.org/doi/10.1103/PhysRevE.82.011911> (visited on 01/24/2021).
- [85] Pauline Durand-Smet et al. “Cytoskeletal organization in isolated plant cells under geometry control”. In: *Proceedings of the National Academy of Sciences* 117.29 (2020), pp. 17399–17408. ISSN: 0027-8424. DOI: 10.1073/pnas.2003184117. eprint: <https://www.pnas.org/content/117/29/17399.full.pdf>. URL: <https://www.pnas.org/content/117/29/17399>.
- [86] P Rezvani Moghaddam and D Wilman. “Cell wall thickness and cell dimensions in plant parts of eight forage species”. In: *The journal of agricultural science* 131.1 (1998), pp. 59–67.
- [87] Milada Čovanová et al. “Overexpression of the Auxin Binding PROTEIN1 Modulates PIN-Dependent Auxin Transport in Tobacco Cells”. In: *PLoS ONE* 8.7 (July 23, 2013). Ed. by Markus Grebe, e70050. ISSN: 1932-6203. DOI: 10.1371/journal.pone.0070050. URL: <https://dx.plos.org/10.1371/journal.pone.0070050> (visited on 01/13/2021).

- [88] Jan Maisch et al. “Tobacco Arp3 is localized to actin-nucleating sites in vivo”. In: *Journal of Experimental Botany* 60.2 (Feb. 2009), pp. 603–614. ISSN: 1460-2431, 0022-0957. DOI: 10.1093/jxb/ern307. URL: <https://academic.oup.com/jxb/article-lookup/doi/10.1093/jxb/ern307> (visited on 01/19/2021).
- [89] Steffen Durst et al. “Organization of perinuclear actin in live tobacco cells observed by PALM with optical sectioning”. In: *Journal of Plant Physiology* 171.2 (Jan. 2014), pp. 97–108. ISSN: 01761617. DOI: 10.1016/j.jplph.2013.10.007. URL: <https://linkinghub.elsevier.com/retrieve/pii/S0176161713004161> (visited on 01/19/2021).
- [90] Justin Bois. *Introduction to Bayesian Modeling*. Sept. 2018. URL: [http://bebi103.caltech.edu.s3-website-us-east-1.amazonaws.com/2018/lecture\\_notes/105\\_intro\\_to\\_bayesian\\_modeling.pdf](http://bebi103.caltech.edu.s3-website-us-east-1.amazonaws.com/2018/lecture_notes/105_intro_to_bayesian_modeling.pdf).
- [91] Michael Betancourt. *Probabilistic Modeling and Statistical Inference*. betanalphabet.github.io. Mar. 2019. URL: [https://betanalphabet.github.io/assets/case\\_studies/modeling\\_and\\_inference.html](https://betanalphabet.github.io/assets/case_studies/modeling_and_inference.html).
- [92] Ovijit Chaudhuri, Sapun H. Parekh, and Daniel A. Fletcher. “Reversible stress softening of actin networks”. In: *Nature* 445.7125 (Jan. 2007), pp. 295–298. ISSN: 0028-0836, 1476-4687. DOI: 10.1038/nature05459. URL: <http://www.nature.com/articles/nature05459> (visited on 11/06/2019).
- [93] Teng Li. “A mechanics model of microtubule buckling in living cells”. In: *Journal of Biomechanics* 41.8 (2008), pp. 1722–1729. ISSN: 00219290. DOI: 10.1016/j.jbiomech.2008.03.003. URL: <https://linkinghub.elsevier.com/retrieve/pii/S0021929008001176> (visited on 02/17/2021).
- [94] Enrique R Rojas and Kerwyn Casey Huang. “Regulation of microbial growth by turgor pressure”. In: *Current Opinion in Microbiology*. Cell Regulation 42 (Apr. 1, 2018), pp. 62–70. ISSN: 1369-5274. DOI: 10.1016/j.mib.2017.10.015. URL: <https://www.sciencedirect.com/science/article/pii/S1369527417300395> (visited on 02/04/2021).
- [95] David Alsteens et al. “Structure, cell wall elasticity and polysaccharide properties of living yeast cells, as probed by AFM”. In: *Nanotechnology* 19.38 (Sept. 24, 2008), p. 384005. ISSN: 0957-4484, 1361-6528. DOI: 10.1088/0957-4484/19/38/384005. URL: <https://iopscience.iop.org/article/10.1088/0957-4484/19/38/384005> (visited on 02/16/2021).
- [96] John W. Goss and Catherine B. Volle. “Using Atomic Force Microscopy To Illuminate the Biophysical Properties of Microbes”. In: *ACS Applied Bio Materials* 3.1 (Jan. 21, 2020), pp. 143–155. ISSN: 2576-6422, 2576-6422. DOI: 10.1021/acsabm.9b00973. URL: <https://pubs.acs.org/doi/10.1021/acsabm.9b00973> (visited on 02/16/2021).

- [97] Richard G. Bailey et al. “The Interplay between Cell Wall Mechanical Properties and the Cell Cycle in *Staphylococcus aureus*”. In: *Biophysical Journal* 107.11 (Dec. 2, 2014), pp. 2538–2545. ISSN: 0006-3495. DOI: 10.1016/j.bpj.2014.10.036. URL: <https://www.ncbi.nlm.nih.gov/pmc/articles/PMC4255174/> (visited on 02/05/2021).
- [98] Viggo Tvergaard and Alan Needleman. “Effect of Properties and Turgor Pressure on the Indentation Response of Plant Cells”. In: *Journal of Applied Mechanics* 85.6 (June 1, 2018). ISSN: 0021-8936. DOI: 10.1115/1.4039574. URL: <https://asmedigitalcollection.asme.org/appliedmechanics/article/85/6/061007/421999/Effect-of-Properties-and-Turgor-Pressure-on-the> (visited on 11/06/2019).
- [99] T. Nakamura, T. Wang, and S. Sampath. “Determination of properties of graded materials by inverse analysis and instrumented indentation”. In: *Acta Materialia* 48.17 (Nov. 2000), pp. 4293–4306. ISSN: 13596454. DOI: 10.1016/S1359-6454(00)00217-2. URL: <https://linkinghub.elsevier.com/retrieve/pii/S1359645400002172> (visited on 11/06/2019).
- [100] Michael Smith. *ABAQUS/Standard User’s Manual, Version 6.9*. English. United States: Dassault Systèmes Simulia Corp, 2018.
- [101] J. A. Hobot et al. “Periplasmic gel: new concept resulting from the reinvestigation of bacterial cell envelope ultrastructure by new methods.” In: *Journal of Bacteriology* 160.1 (Oct. 1, 1984), pp. 143–152. ISSN: 0021-9193, 1098-5530. URL: <https://jlb.asm.org/content/160/1/143> (visited on 02/08/2021).
- [102] James C. Gumbart et al. “Escherichia coli Peptidoglycan Structure and Mechanics as Predicted by Atomic-Scale Simulations”. In: *PLOS Computational Biology* 10.2 (Feb. 20, 2014). Publisher: Public Library of Science, e1003475. ISSN: 1553-7358. DOI: 10.1371/journal.pcbi.1003475. URL: <https://journals.plos.org/ploscompbiol/article?id=10.1371/journal.pcbi.1003475> (visited on 02/03/2021).
- [103] Virginia Vadillo-Rodríguez and John R. Dutcher. “Viscoelasticity of the bacterial cell envelope”. In: *Soft Matter* 7.9 (Apr. 18, 2011). Publisher: The Royal Society of Chemistry, pp. 4101–4110. ISSN: 1744-6848. DOI: 10.1039/C0SM01054E. URL: <https://pubs.rsc.org/en/content/articlelanding/2011/sm/c0sm01054e> (visited on 02/06/2021).
- [104] Nili Grossman, Eliora Z Ron, and Conrad L Woldringh. “Changes in Cell Dimensions During Amino Acid Starvation of *Escherichia coli*”. In: *J. BACTERIOL.* 152 (1982), p. 7.
- [105] A. E. Smith, K. E. Moxham, and A. P. J. Middelberg. “On uniquely determining cell-wall material properties with the compression experiment”. In: *Chemical Engineering Science* 53.23 (Dec. 1, 1998), pp. 3913–3922. ISSN: 0009-2509. DOI: 10.1016/S0009-2509(98)00198-5. URL: <http://www>

- w.sciencedirect.com/science/article/pii/S0009250998001985 (visited on 11/06/2019).
- [106] Rituparna Goswami et al. “Is the plant nucleus a mechanical rheostat?” In: *Current Opinion in Plant Biology*. Cell signalling and gene regulation 57 (Oct. 1, 2020), pp. 155–163. ISSN: 1369-5266. DOI: 10.1016/j.pbi.2020.09.001. URL: <https://www.sciencedirect.com/science/article/pii/S1369526620301072> (visited on 02/26/2021).
- [107] Amar K. Mohanty et al. “Composites from renewable and sustainable resources: Challenges and innovations”. In: *Science* 362.6414 (2018), pp. 536–542. ISSN: 0036-8075. DOI: 10.1126/science.aat9072. eprint: <https://science.sciencemag.org/content/362/6414/536.full.pdf>. URL: <https://science.sciencemag.org/content/362/6414/536>.
- [108] A. K. Mohanty, M. Misra, and G. Hinrichsen. “Biofibres, biodegradable polymers and biocomposites: An overview”. In: *Macromolecular Materials and Engineering* 276-277.1 (2000), pp. 1–24. DOI: 10.1002/(SICI)1439-2054(20000301)276:1<1::AID-MAME1>3.0.CO;2-W. eprint: <https://onlinelibrary.wiley.com/doi/pdf/10.1002/%28SICI%291439-2054%2820000301%29276%3A1%3C1%3A%3AAID-MAME1%3E3.0.CO%3B2-W>. URL: <https://onlinelibrary.wiley.com/doi/abs/10.1002/%28SICI%291439-2054%2820000301%29276%3A1%3C1%3A%3AAID-MAME1%3E3.0.CO%3B2-W>.
- [109] Murali M. Reddy et al. “Biobased plastics and bionanocomposites: Current status and future opportunities”. In: *Progress in Polymer Science* 38.10 (2013). Progress in Bionanocomposites: from green plastics to biomedical applications, pp. 1653–1689. ISSN: 0079-6700. DOI: <https://doi.org/10.1016/j.progpolymsci.2013.05.006>. URL: <http://www.sciencedirect.com/science/article/pii/S0079670013000476>.
- [110] Kuan-Chen Cheng, Jeff M Catchmark, and Ali Demirci. “Enhanced production of bacterial cellulose by using a biofilm reactor and its material property analysis”. In: *Journal of biological engineering* 3.1 (2009), pp. 1–10.
- [111] M. Vidali. “Bioremediation. An overview”. In: *Pure and Applied Chemistry* 73.7 (July 1, 2001), pp. 1163–1172. ISSN: 1365-3075, 0033-4545. DOI: 10.1351/pac200173071163. URL: <https://www.degruyter.com/view/journals/pac/73/7/article-p1163.xml> (visited on 01/08/2021).
- [112] Alan W. Decho. “Overview of biopolymer-induced mineralization: What goes on in biofilms?” In: *Ecological Engineering* 36.2 (Feb. 2010), pp. 137–144. ISSN: 09258574. DOI: 10.1016/j.ecoleng.2009.01.003. URL: <https://linkinghub.elsevier.com/retrieve/pii/S0925857409001128> (visited on 01/08/2021).

- [113] Dan I Piraner et al. “Tunable thermal bioswitches for in vivo control of microbial therapeutics”. In: *Nature Chemical Biology* 13.1 (Jan. 2017), pp. 75–80. ISSN: 1552-4450, 1552-4469. DOI: 10.1038/nchembio.2233. URL: <http://www.nature.com/articles/nchembio.2233> (visited on 01/11/2021).
- [114] Peter C.Y. Lau et al. “Absolute Quantitation of Bacterial Biofilm Adhesion and Viscoelasticity by Microbead Force Spectroscopy”. In: *Biophysical Journal* 96.7 (Apr. 2009), pp. 2935–2948. ISSN: 00063495. DOI: 10.1016/j.bpj.2008.12.3943. URL: <https://linkinghub.elsevier.com/retrieve/pii/S0006349509004226> (visited on 01/26/2021).
- [115] Sara Kesel et al. “Direct Comparison of Physical Properties of *Bacillus subtilis* NCIB 3610 and B-1 Biofilms”. In: *Applied and Environmental Microbiology* 82.8 (Apr. 15, 2016). Ed. by J. L. Schottel, pp. 2424–2432. ISSN: 0099-2240, 1098-5336. DOI: 10.1128/AEM.03957-15. URL: <http://aem.asm.org/lookup/doi/10.1128/AEM.03957-15> (visited on 01/08/2021).
- [116] M. Asally et al. “Localized cell death focuses mechanical forces during 3D patterning in a biofilm”. In: *Proceedings of the National Academy of Sciences* 109.46 (Nov. 13, 2012), pp. 18891–18896. ISSN: 0027-8424, 1091-6490. DOI: 10.1073/pnas.1212429109. URL: <http://www.pnas.org/cgi/doi/10.1073/pnas.1212429109> (visited on 01/12/2021).
- [117] Konstantin Zuev. “Statistical Inference”. In: *arXiv:1603.04929 [math, stat]* (Mar. 15, 2016). arXiv: 1603.04929. URL: <http://arxiv.org/abs/1603.04929> (visited on 02/24/2021).